Investigation of γ-TiAl Alloys by means of Diffraction Methods

Doctoral Thesis

Dipl.-Ing. Thomas Schmölzer

Department of Physical Metallurgy and Materials Testing
Montanuniversität Leoben

Leoben, April 2012

Affidavit

I declare in lieu of oath that I wrote this thesis and performed the associated research myself, using only literature cited in this volume.

Leoben, 10 April 2012 Dipl.-Ing. Thomas Schmoelzer

Acknowledgements

It would have been impossible to write this thesis without the support and guidance of many different persons. I want to express my gratitude to everybody who contributed to this work in the following.

I am grateful to Prof. Helmut Clemens, who offered me the opportunity to perform this thesis and offered guidance as well as a large number of interesting ideas.

The readiness of Prof. Gerhard Dehm to act as a reviewer for this thesis is highly acknowledged.

Dr. Klaus-Dieter Liss, Dr. Peter Staron and Dr. Andreas Stark contributed greatly to this thesis by providing me with expert advice and introducing me to in-situ diffraction techniques. I want to thank them also for many fruitful discussions that inspired me and helped me to see things from a different angle.

Thanks go also to my colleagues in the high temperature materials group. Thanks go to Dr. Svea Mayer for providing support, Emanuel Schwaighofer for contributing to the advancement of X-ray diffraction at our department, Andrea Gaitzenauer and Robert Werner for interesting conversations and Martin Schloffer for generating vast piles of data. The production of numerous specimens by Albert Themessl and Christian Sailer is highly acknowledged.

Without the help of the non-scientific employees at the Department, I would have spent considerably less time pursuing my research. I want to thank all of them for their valuable contributions.

Many thanks go to the beamline scientists and to the administrative staff at DESY and ESRF. Without their support we would not have been able to perform experiments at synchrotron sources. Financial support by the Helmholtz Zentrum Geesthacht and the European Community's Sevent Framework Programme (FP7/2007–2013) under grant agreement numbers 226507 and 226716 is highly acknowledged.

I furthermore want to thank my friends and colleagues Sophie Primig, Christoph Lerchbacher, Matthias Nöhrer, Rainer Hochfellner, Dr. David Holec, Dr. Michael Zuber, Dr. Harald Wurmbauer, Dr. Erich Stergar, Dr. Michael Schober and Eva Eidenberger for creating a positive and inspiring working atmosphere. Dr. Elisabeth Eidenberger significantly contributed to this thesis by actively promoting my scientific skills which is highly acknowledged. Dr. Christoph Kirchlechner has always been a critical and inspiring discussion partner who is always asking the right questions which is highly appreciated.

Many thanks go to my parents and also to my grand-mother who managed to direct my insatiable thirst for knowledge into the right direction instead of quenching it by telling me not to ask too many questions. I am grateful for their continuous support in my academic as well as in my personal aims.

I am deeply indebted to my beloved wife Kerstin and my wonderful son Florian. They have endured long hours at home while I was in the office and instead of complaining supported me in my pursuit of this thesis. It would not have been possible to finish this thesis without their understanding for which I am incredibly grateful.

Table of Contents

Abbreviations

Al	Aluminum
AT(-plot)	Azimuthal angle – time (plot)
B	Boron
bcc	Body centered cubic
BSE	Back-scattered electron (contrast)
CALPHAD	Calculation of phase diagrams
Cu	Copper
DESY	Deutsches Elektronen Synchrotron
DRV	Dynamic recovery
DRX	Dynamic recrystallization
DSC	Dynamic scanning calorimetry
EBSD	Electron back scatter diffraction
ETMT	Electro thermo-mechanical tester
fcc	Face centered cubic
FEG	Field emission gun
f_q	Atomic X-ray form factor
F_{HKL}	Structure factor
HAGB	High-angle grain boundary
hcp	Hexagonal close packed
HEXRD	High energy X-ray diffraction
LAGB	Low-angle grain boundary
Nb	Niobium
Mo	Molybdenum
ppm	Parts per million
Pt	Platinum
q	Scattering vector $q=(4\pi/\lambda)\cdot\sin(\theta)$
r_e	Classical electron radius
RV	Recovery
RX	Recrystallization
SEM	Scanning electron microscope
Ta	Tantalum
TEM	Transmission electron microscope
Ti	Titanium
XRD	X-ray diffraction
γ	Azimuthal angle
Θ	Bragg angle
3D-XRD	Three-dimensional X-ray diffraction

1 Introduction

In 2010, it was the first time that engines equipped with TiAl blades propelled a commercially operated airplane. This fact is just one indication of the advent of γ-TiAl based alloys in applications where light-weight materials with high strength and creep resistance are required [1–7]. In the temperature range from 600 °C to 800 °C intermetallic γ-TiAl alloys can substitute Ni-based alloys bringing about a significant reduction in component weight [8–13]. The main applications driving the development of TiAl alloys are low-pressure turbine blades of jet-engines and turbocharger wheels for reciprocating engines.

The establishment of a reliable and cost-effective processing route is a crucial step for the widespread use of TiAl components. Exploiting the high deformability of the disordered β-phase at high temperatures [2,14–16] allows deformation of TiAl alloys in near-conventional hot-die forging processes [2,6,17–19]. Subsequent heat-treatments can be used to reduce the amount of the ordered β_o-phase which has poor creep resistance and low room-temperature ductility [6,20–22]. Additionally the microstructure can be adjusted in such a way as to attain the desired mechanical properties. To be able to design such a process, the dependence of phase fractions on temperature and alloy composition has to be well understood. Dislocation motion is frequently significantly different in ordered phases as compared to their disordered configurations [23] which is also reported to be true for the β/β_o-phase [19]. Consequently, the ordering temperatures of phases are also of interest.

Since thermodynamic calculations were shown to yield inconsistent results [24,25], the phase transformation temperatures and the course of phase fractions were determined experimentally. Due to a multitude of occurring phase transformations and the different length scales of the microstructural constituents, microscopic methods suffer from severe limitations. Powder diffraction offers the benefit of illuminating a large number of grains and therefore provides results of high statistical relevance [26]. Furthermore, in-situ experiments are possible at synchrotron sources, enabling the direct observation of the materials behavior [27]. For TiAl alloys, superstructure peaks, indicating the presence of order in a phase, are of rather low intensity in diffraction patterns obtained at X-ray sources. Due to this reason, ordering phenomena are ideally investigated by means of neutron diffraction, which produces superstructure peaks of high intensity [28,29].

TiAl alloys are materials with challenging hot-working properties [13,30]. Investigating the processes which accommodate the plastic deformation during hot-working is a difficult task. Again, with microscopic methods, only a post-mortem analysis of the microstructure can be performed. Some microstructural features might be obscured by rapidly occurring static annealing phenomena or phase transitions occurring during cooling of the specimen. Fast state-of-the-art flat-panel detectors enable the acquisition of

diffraction patterns at high frame rates [31]. This made it possible to apply a diffraction technique proposed by Liss et al. to the investigation of the hot-deformation behavior of γ-TiAl alloys [32–35].

To obtain additional information and to verify the results of in-situ experiments, complementary methods were employed. Especially scanning electron microscopy (SEM) and electron back-scatter diffraction (EBSD) were used for microstructural investigations [29,36]. To check the validity of the temperature control during the in-situ experiments thermal analysis tools such as dilatometry and dynamic scanning calorimetry (DSC) were utilized [21,37].

In the following, information on the phases occurring in TiAl alloys are provided. The diffraction methods employed in the course of this thesis are elaborated in Chapter 3. In Chapter 4, a technique for investigating the materials behavior during deformation is introduced. A short overview of the complementary methods employed and references to the relevant literature are given in Chapter 5. An outline of each of the appended publications is provided before the thesis is summarized and concluded.

2 The System Ti-Al

For developing new alloys and designing reliable processing routes, a profound understanding of the relevant phase diagrams is a prerequisite. In the case of TiAl alloys, the investigation of phase diagrams is complicated by the large number of different phases occurring [38]. It is frequently difficult to discern between ordered and disordered variants of phases and the existence of a number of orientation relationships promotes the formation of intricate microstructures (e.g. [39]). In the following, a short introduction to the most important phases and the phase diagrams is given.

2.1 Primary Phases Occurring in Advanced γ-TiAl Alloys

As already hinted by the name of this alloy class, the tetragonal body centered γ-phase is the most prominent phase in γ-TiAl alloys at room temperature. It possesses a $L1_0$ crystal structure and is ordered up to its dissolution temperature. To highlight its similarity to the face centered cubic (fcc) crystal structure, two unit cells of γ-phase are usually drawn which resembles an fcc unit cell with a slightly elongated c-axis (Figure 1a) [40]. The ideal stoichiometric ratio of Al and Ti atoms in the γ-phase is 1. If Nb is alloyed to a binary alloy, it is reported that Nb atoms only occupy Ti positions in the γ-phase [41–43]. Mo is uniformly distributed among Ti and Al lattice sites [44].

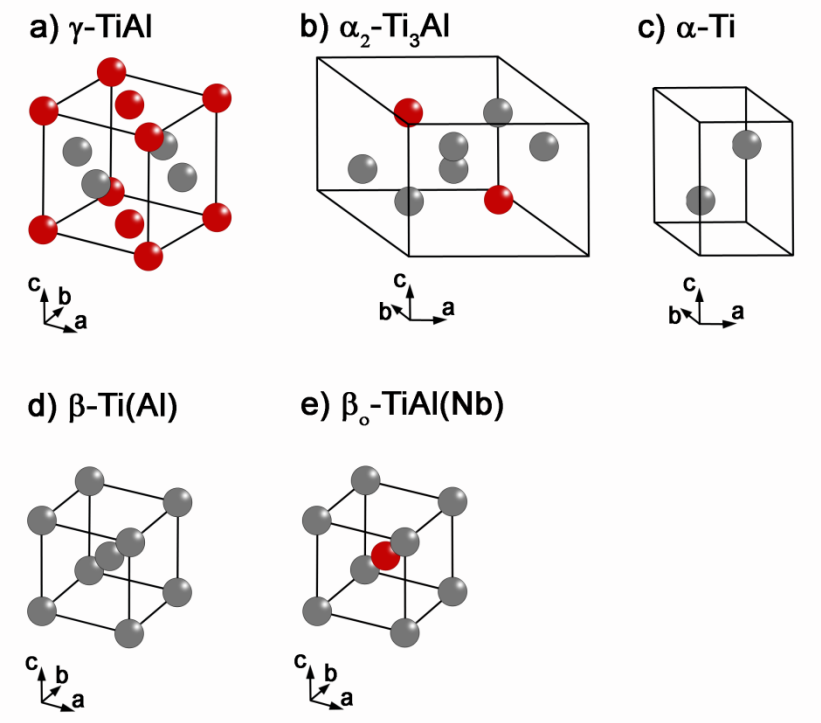

Figure 1: Crystal structures of the main phases observed in γ-TiAl alloys. Ti atoms are colored grey, Al atoms red. Note that for the γ-phase two unit cells are drawn to highlight the resemblance to the fcc structure. [40]

A range of existence calculated for the γ-phase in a Ti-X Al-4 Nb-1 Mo-0.1 B alloy is presented in Figure 2. Note that in this thesis all compositions are given in atomic percent unless stated otherwise. It should be noted that the γ-phase has a rather wide range of existence and, hence, the chemical composition does not necessarily correspond to the exact stoichiometric ratio. Concerning mechanical properties and additional information on the effect of alloying elements, the reader is referred to the corresponding literature e.g. [22,37,45,46]. The phase diagram shown in Figure 2 describes the appearing phases in the TNM™ alloy. This alloy exhibits a nominal composition of Ti-43.5 Al-4 Nb-1 Mo-0.1 B and was developed at the Department of Physical Metallurgy and Materials Testing at the Montanuniversität Leoben. It possesses excellent hot-working behavior and exhibits balanced mechanical properties as reported in the corresponding literature [2,6,39,47–49].

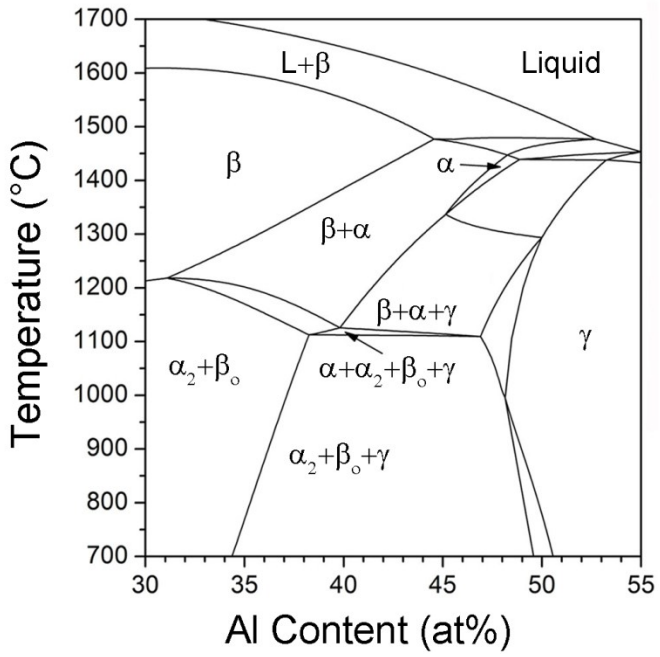

Figure 2: Calculated section of the phase diagram for Ti-(30-55) Al-4 Nb-1 Mo-0.1 B including 450 mass-ppm oxygen. This quasi-binary phase diagram was obtained by using the CALPHAD method. After [50].

The α_2-phase is an ordered structure of the $D0_{19}$ type which plays an important role in γ-TiAl alloys. At the eutectoid temperature (see Figure 2) the α_2-phase (Figure 1b) disorders to the α-phase which exhibits an A3 hexagonal close packed (hcp) structure (Figure 1c). Crystal structures of α_2 and α are given in Figure 1. Ordering upon cooling occurs at such high rates that α cannot be stabilized to room-temperature [40]. While the total formula of α_2 is Ti_3Al, the disordered α-phase is frequently designated α-Ti(Al) due to its similarity to the α-phase in Ti alloys. It should, however, be noted that also the α-phase contains a significant amount of Al and, in the case of advanced γ-TiAl alloys,

other alloying elements. It was found that Nb and Mo occupy Ti sites in Ti_3Al alloys [51] and it is therefore reasonable to assume that the same is true for the α_2-phase in γ-TiAl alloys. Further details on the nature of the α_2/α-phase are given in [42,51–54].

Possessing a body centered cubic (bcc) (A2) structure (Figure 1d) and a correspondingly high number of independent slip systems, the β-phase decisively determines the deformation behavior of TNM™ alloys at high temperatures [2,14,18,49,55]. Upon cooling, β-Ti(Al) transforms to the cubic primitive, ordered B2 structure (Figure 1e) and is designated β_o in the following [40,56]. This ordering reaction occurs at extraordinarily high rates which prevents observing the β-phase at room-temperature [57]. In TNM™ alloys, the β/β_o-phase is commonly enriched in heavy alloying elements such as Nb and Mo. Nb was reported to preferentially occupy Al lattice sites in the β/β_o-phase [40].

2.2 Low-Symmetry Phases in Ti-Al-X Systems

In addition to the primary phases, there are a number of phases with lower symmetry that can be observed in γ-TiAl alloys. Since these are metastable phases, they are not indicated in the corresponding phase diagrams. They are, however, of some technological relevance. This is, on one hand, due to the fact that these phases could occur during service conditions which might lead to a change in properties of the alloys [58,59]. On the other hand, all of these phases exhibit strong structural relations to the primary phases in γ-TiAl alloys and might therefore occur as transient phases facilitating phase transformations [58,60,61].

The ω-phase (C32) forms in Ti alloys from the β-phase by a small distortion of the lattice parameters (about 1%) and the displacement of atomic layers by 1/12 [111] β or, correspondingly, 1/6 [0001] ω [58,60]. This leads to a so-called layer collapse which is presumed to occur by the formation of a trigonal transition phase [62]. In Figure 3a, the unit cell of the ω-phase is shown.

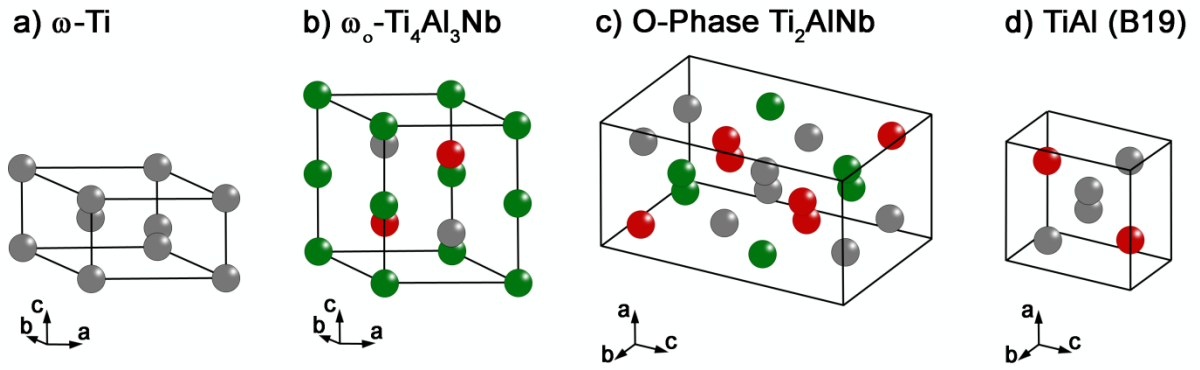

Figure 3: Crystal structures of low-symmetry phases occurring in γ-TiAl alloys. Ti sites are indicated by grey spheres; Al is represented by red spheres and Nb is shown in green. After [40].

Similarly to the formation of ω from β occurs the formation of ω_o from β_o. In addition to the distortion of the unit cell and the layer collapse, atoms have to change their lattice positions in order to form the $B8_2$ structure of the ω_o-phase (Figure 3b) [40].

At high Ti and Nb contents, the so-called O-phase can form which has a total formula of Ti_2AlNb. In terms of crystal structure, this phase is related to both, the α/α_2-phase and the β/β_o-phase (Figure 3c). For details concerning the structural relation, the reader is referred to the thesis of A. Stark [40]. A phase that was proposed as a transitional phase for the phase transformation $\beta_o \rightarrow$O-phase is of the B19 structure (Figure 3d) [63]. Experimentally, however, the B19-phase was observed to form upon quenching from the α single phase field [57] or during an ensuing heat-treatment [64], where it facilitates the precipitation of γ-phase. In Figure 4, the structural relations between the main phases in γ-TiAl alloys and B19 are illustrated. The closest packed planes of B19 and γ are identical, only the stacking sequence is different (…ABABAB… in B19 instead of …ABCABC… in γ). If the closest packed planes of α/α_2 and B19 are compared, the different site occupation is obvious. With β_o, B19 shares also a common close packed plane. It is evident that B19 is structurally closely related to α_2, β_o, and γ as well as to the metastable O-phase.

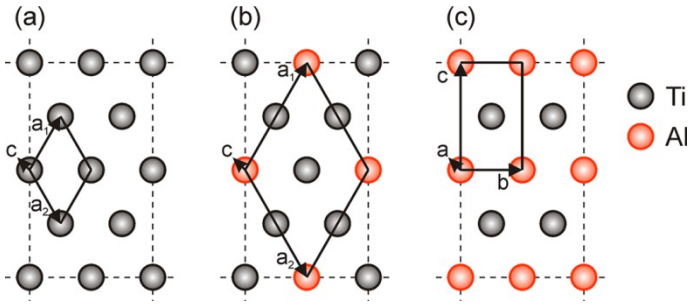

Figure 4: Structural relations of different phases in the TiAl system illustrated by the comparison of their closest packed planes. (a) {0001} α-Ti, (b) {0001} α_2-Ti_3Al, (c) {100} B19-TiAl. The unit cells are indicated by the solid lines. It is important to recognize that (a) also corresponds to {100} β-Ti(Al) and (c) is identical to {111} γ-TiAl as well as {110} β_o-TiAl. After [40,57]. (Appendix F)

2.3 Orientation Relationships

Due to the fact that many phases in the TiAl alloy systems share common closest packed planes with little differences in lattice parameters, it is not surprising that a number of orientation relationships are reported. The most important one is the Blackburn relationship which describes the relative orientations between α_2 and γ which is the basis for the formation of lamellar colonies. A small lattice misfit (~ 1 %) between the two phases is caused by the fact that the c axis of the γ unit cell is slightly elongated compared to an fcc lattice that would enable a perfect fit between the two phases. Blackburn [65] formulated the following relation:

{111}γ ‖ (0001)α_2 and <1-10>γ ‖ <11-20>α_2

Between α_2 and β_o phase the Burgers orientation relation is frequently observed:

{110}bcc ‖ (0001)hcp and <111>bcc ‖ <11-20)hcp

For the Burgers relation, a rather large misfit in the range of ~10 % exists [40]. In addition to these well-established relations, a number of similar relations are feasible between stable and metastable phases (see [66]). In principle, all of these relations can be derived from either the Burgers or the Blackburn orientation relation. Details can be found in [40].

2.4 Non Stoichiometric Phases

In this chapter, up to now, it was assumed that the chemical composition of the phases corresponds to their stoichiometric composition. All phases discussed, however, exist over a certain range of chemical composition at different temperatures. In some cases, especially at high temperatures, these ranges can be very large. For TNM™ alloys, for instance, it is possible to enter a single β-phase field at a sufficiently high temperature which extends from the alloy composition to pure Ti. Upon rapid quenching, a large part of β transforms to α_2, the remaining fraction of β orders to β_o [67]. Due to the high cooling rate, it can be assumed that no long-range diffusional processes were possible during quenching. This entails that the chemical compositions of the resulting α_2 and β_o phases are close to the overall chemical composition of the alloy and far from their stoichiometric compositions. Correspondingly, the occupation of the lattice sites deviates from that of the ideal ordered phases and the lattice parameters are different from the tabulated values. In the case of the α_2-phase the c/a ratio was reported to be dependent on its Ti/Al ratio [68]. The same effect can be suspected for the γ-phase from the results presented in [69]. Due to this reason, the lattice mismatch for the different orientation relations might deviate from the values indicated in literature. Another consequence from this behavior is that the chemical composition of a grain is a poor indicator of what phase is present. Back-scattered electron (BSE) contrast in the SEM can be exceptionally low in TiAl microstructures far from equilibrium conditions due to the fact that all occurring phases exhibit similar chemical compositions. Since the above described phases are all structurally closely related it is in some cases difficult to determine the type of a phase observed in a non-equilibrium microstructure.

In some cases, the question should be raised if the exact classification of a phase that does not exhibit a stoichiometric composition serves the purpose of understanding the materials behavior. Determining whether the phase in the TNM™ specimen quenched from the β single phase field corresponds rather to α or α_2 is difficult since the chemical composition of 52 Ti-43 Al-4 Nb-1 Mo does not allow to attain perfect order. In this thesis a phase is designated as ordered phase if superstructure peaks are visible in the diffraction pattern. Although this is not a rigorous criterion, it is sufficient for our purpose.

3 Determination of Phase Fractions and Ordering Temperatures with Diffraction Methods

In Chapter 2, the phases encountered in advanced γ-TiAl alloys were introduced. These phases have different mechanical and thermal properties which enables adjusting the characteristics of an alloy by controlling the phase fractions and their morphology [2,10,70]. Calculation of phase fractions by means of the CALPHAD method is difficult in the case of TiAl alloys since no adequate thermodynamical databases are available. Due to this reason, the simulations conducted yield phase diagrams that are inaccurate especially in terms of the phase transition temperatures [21,25,50]. Phase fractions can be determined by heat-treating and quenching a specimen prior to metallographic examination in the SEM. For high temperatures, this is not possible in the case of TiAl alloys because rapid phase transformations occur upon cooling which leads to erroneous results [67,71]. Additionally, the fine microstructural features present at ambient temperature make it difficult to determine phase fractions by microscopic methods. With in-situ diffraction methods, phase fractions can be analyzed accurately as a function of temperature. Additionally, ordering temperatures can be evaluated through the appearance of superstructure peaks in the diffraction pattern. The special issue of Advanced Engineering Materials on the "Application of Photons and Neutrons for the Innovation of Engineering Materials" [72] and the textbook "Neutrons and Synchrotron Radiation in Engineering Materials Science" [73] provide further information on modern diffraction methods and their application to TiAl alloys.

3.1 Properties and Contrast Formation for X-Rays and Neutrons

For the analysis of crystal structures by means of diffraction methods either neutrons or X-rays are used in materials science. Electrons can also be employed for performing diffraction experiments on thin specimens. This is commonly used in the transmission electron microscope (TEM) where in-situ experiments suffer from some restrictions in terms of temperature and investigated volume which is why this technique shall be discussed here no further [74]. The principles that govern contrast formation for X-rays and neutrons are quite different; whereas photons interact with the electrons in the shell of atoms, neutrons are only interacting with atomic nuclei. In the case of X-rays, a strong correlation between the scattering length densities of atoms and their atomic number exists, while no such relationship can be established for neutrons [75].

Due to the relatively weak interaction of neutrons with the common isotopes of many heavy elements such as Fe, Cr, Ni, etc. their penetration depth of many materials used in engineering materials science is high. The penetration power of X-rays depends strongly on the photon energy and is generally lower than that of thermal neutrons. Laboratory X-ray sources usually generate radiation with energies in the range of 10 keV (a typical source would be a Cu K_α tube with E=8.06 keV) which translates to attenuation

lengths in the order of 10 µm for common metals. Synchrotron sources offer much higher brilliance and the possibility to use radiation of higher energy at dedicated beamlines [27]. At an energy of 100 keV, the attenuation length increases to the order of 1 cm which allows performing experiments in which the bulk behavior of specimens is investigated [26]. Another advantage of using high energy X-rays lies in the small diffraction angles which allow the use of bulky specimen environments.

In the case of neutrons, the scattering behavior of individual atoms is characterized by their bound coherent scattering length. For X-rays, the scattering length of an atom is determined by $r_e \cdot f(q)$, where r_e is the classical electron radius, whereas $f(q)$ is the atomic X-ray form factor [76]. The intensity of a peak in the diffractogram is determined not only by the scattering lengths of the atoms, but also by the spatial arrangement of the atoms within the crystal. This is accounted for by the phase factor which is dependent on the positions of individual atoms within the unit cell. Summing up all the atomic scattering lengths weighted by the respective phase factors for all atoms in the unit cell yields the structure factor F_{hkl}, which ultimately determines the intensity of a reflection [77]. If the main reflections of a phase are considered, the phase factor is close to one and the scattering lengths of the individual atoms add up directly. For a superstructure reflection, the scattering lengths of the atomic sites in the unit cell are equal but of opposite sign.

For an atomic species disordered crystal, an average atomic scattering length is calculated from the scattering lengths of the constituting atoms weighted by their atomic fraction and all lattice sites are assumed to exhibit this mean atomic scattering length. Consequently, the intensity of ordinary reflections is determined by the average scattering length density and the superstructure reflections exhibit zero intensity. If an ordered crystal is considered, the calculation of an average scattering density would lead to erroneous results. Instead, the structure factor is calculated by summing up the scattering lengths of the atoms sitting on individual lattice sites multiplied by the corresponding phase factors over all lattice positions. Since different atomic species exhibit different scattering lengths, the superstructure reflections of ordered phases attain non-zero values.

In the case of TiAl, the scattering lengths for Ti and Al are -3.370 fm and 3.449 fm for neutrons, respectively [75]. The scattering lengths for X-rays at 100 keV are b_{Ti}=6.207 fm and b_{Al}=3.664 fm. It is important to notice that the scattering lengths of Ti and Al for neutrons are almost identical but of opposite sign. This leads to the peculiar situation that the average scattering length is a small number resulting in very small diffraction peaks for a disordered phase in which the ratio of Ti:Al is close to 1. For the superstructure reflections, however, high intensities are observed (see Figure 5 a). In X-ray diffraction, high intensities are observed for the main reflections of ordered and disordered crystals (Figure 5 b). The superstructure peaks exhibit rather low intensities. Consequently, neutron diffraction is well

suited to investigate order/disorder transition, whereas X-ray diffraction is preferably used for phase fraction determination.

In addition to the physical differences between neutrons and X-rays, a few words regarding the corresponding sources are due. Laboratory X-ray sources are easily available and cost-effective, but provide only low brilliance at moderate energies. Synchrotron sources offer much higher brilliance and a broad range of possible energies [78]. In exchange for this, beam-time is limited and access to synchrotrons is usually only granted after a written application. Neutron sources used in material science are usually nuclear reactors or spallation sources. These facilities are also only accessible after an application for beam-time has been approved. In contrast to synchrotrons, however, neutron sources exhibit comparatively low brilliance [79].

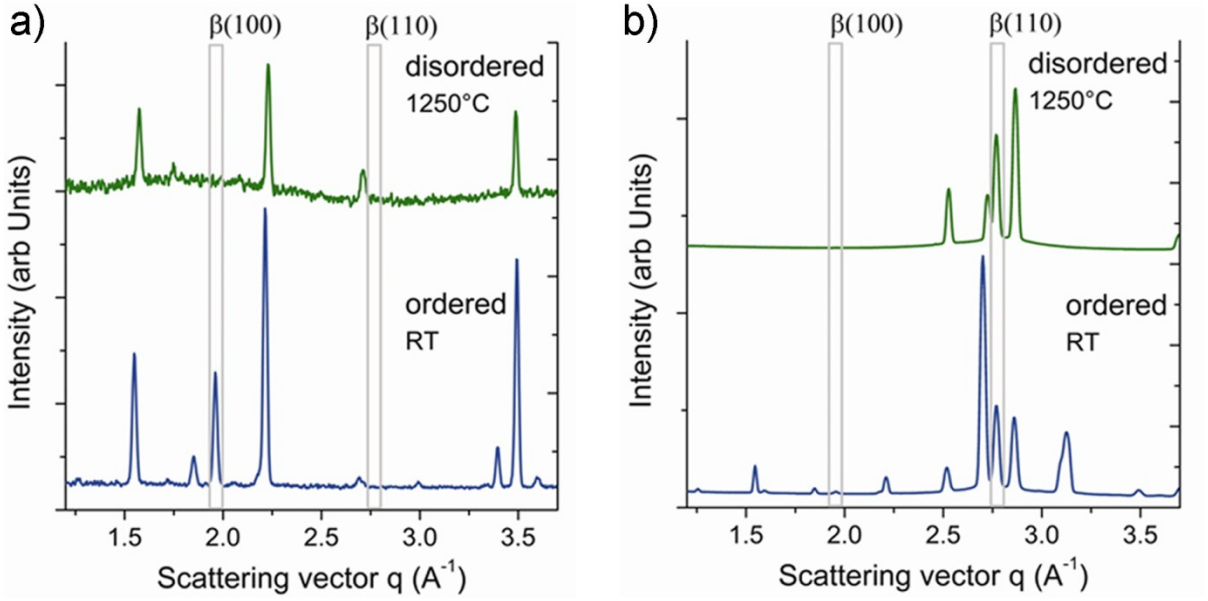

Figure 5: Integrated diffraction patterns of a TNM™ alloy obtained by (a) neutron and (b) X-ray diffraction. For each case one diffraction pattern obtained at room-temperature (bottom) and one recorded at 1250 °C (top) is shown. It can be seen that the superstructure peak (β (100)) has a high intensity and the "ordinary" peak (β(110)) has a low intensity for neutron scattering (a). In the case of X-rays (b), the ordinary peak exhibits a high intensity, whereas the superstructure peak has low intensity.

3.2 The Powder Diffraction Experiment

Debye and Scherrer published a paper in 1916 which laid the foundation for today's powder diffraction methods [80]. The use of sources with high brilliance, smaller beams, and modern detectors has brought about a plethora of different applications, but in principle the experimental technique has not changed much since its development. One of the key requirements in powder diffraction is that of small grained specimens to obtain a

statistically valid result [26]. Using 2-dimensional detectors reduces the demands in terms of maximum grain size since the complete Debye-Scherrer rings can be recorded and subsequently integrated over the azimuthal angle. If the powder diffraction experiment is performed at a synchrotron source, the statistics can be further improved by the high penetration power of high-energy X-rays [27]. In Figure 6, a typical experimental layout for a powder diffraction experiment at a synchrotron source in transmission mode is presented.

High-energy X-ray diffraction experiments offer unique advantages for performing in-situ diffraction experiments. As mentioned before, the enhanced statistics through the larger illuminated volume and modern detectors are prerequisites for investigating specimens at temperatures where grain coarsening is important. At energies in the range of 100 keV, a sufficiently large **q** range can be covered even at relatively small diffraction angles. In the case of γ-TiAl alloys, all major Deby-Scherrer rings are observed at Bragg-angles $2\Theta<10°$ at a mean energy of 100 keV. One important advantage of the small diffraction angles is the simple implementation of bulky specimen environments. Determination of the phase fractions as a function of temperature necessitates the use of devices for heating the specimen to the desired temperature.

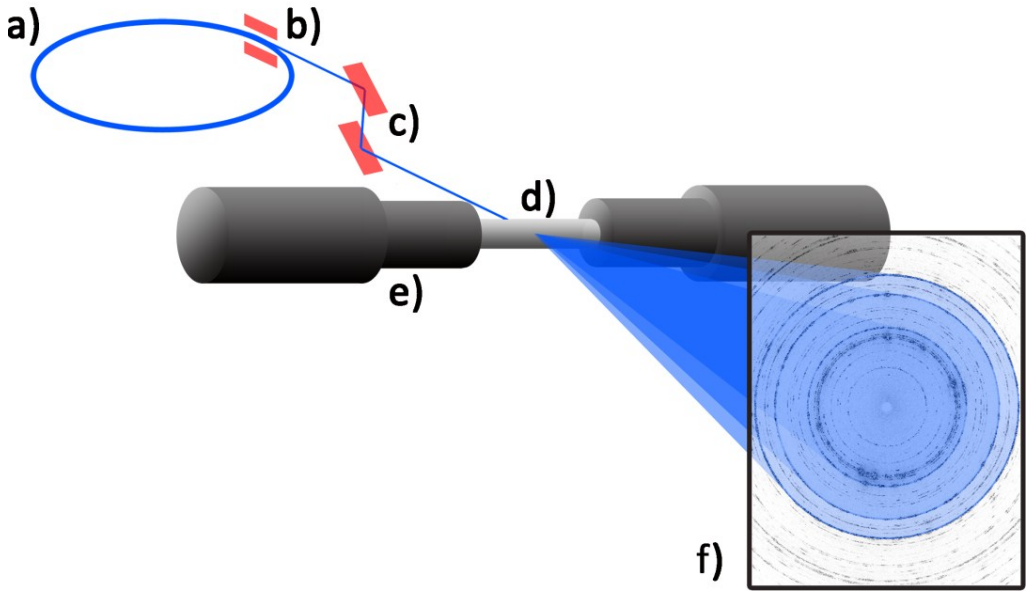

Figure 6: Layout of a typical experimental setup for a powder diffraction experiment at a synchrotron source. Charged particles circulate in the storage ring (a) and emit radiation when deflected by a bending magnet, wiggler, or undulator (b). Radiation within a small energy range is selected by the monochromator (c). The monochromatic beam illuminates the specimen (d) for which various environments, such as a compression device (e) can be provided. A flat-panel detector (f) is employed for recording the diffraction patterns [29] (see also Appendix A).

Additionally, a controlled atmosphere is beneficial in the case of TiAl alloys if temperatures well above 1000 °C are to be investigated. Otherwise an oxidation layer may rapidly form which could affect the experiment [81]. In addition to forming surface oxide layers, TiAl alloys suffer from the selective evaporation of Al close to the specimen surface. Consequently, regions close to the surface are enriched in Ti which increases the fractions of α/α_2 and β/β_o at the expense of γ [50]. A surface layer depleted in Al is visible in the micrograph presented in Figure 7. The influence of this effect can be minimized by using large specimens which decreases the fraction of the volume close to the surface depleted in Al in relation to the total investigated volume.

Another crucial requirement for conducting in-situ diffraction experiments is that of rapid data acquisition. It was already mentioned that synchrotron sources provide a beam with extremely high brilliance. This makes it possible to acquire diffraction images after short exposure times. Together with fast detectors that require little time for the readout, a high frame rate can be achieved enabling the in-situ investigation of phase transformation at high heating or cooling rates.

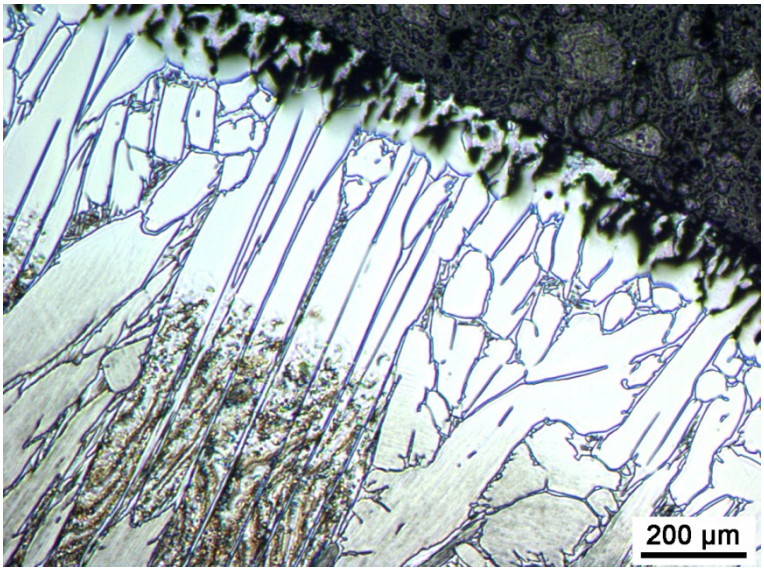

Figure 7: Light optical micrograph showing the Al depletion layer close to the specimen surface. This specimen was heated to a temperature of 1450 °C and held for 60 min.

3.3 Data Analysis

The first step in phase analysis is usually to integrate the two-dimensional detector images over the azimuthal angle γ. This results in plots of intensity over the scattering vector **q** or the Bragg angle 2Θ. When performing this integration, special care should be taken to account for a number of corrections that can be incorporated in this step. Recording a diffraction pattern of a standard specimen (such as, i.e., LaB_6 powder) enables to calculate the exact specimen to detector distance for a given mean energy of the beam, the tilt angles of the detector with respect to the beam axis, and the center of the Debye-Scherrer rings. Additionally, a background image can be subtracted from the recorded image, the small-angle scattering signal around the beam-stop can be masked and pixels that exceed a threshold value can be disregarded. A commonly used software tool to perform these corrections is named fit2D and was developed by Hammersley et al. [82].

Once the diffraction data are plotted as intensity over 2Θ, phase fraction analysis can be performed by different methods. Rietveld analysis is based on a whole-pattern fitting approach. It is not the purpose of this thesis to delve deep into the principles of Rietveld fitting and structure refinement, consequently the reader is referred to the corresponding literature, i.e. [83–85]. In the course of this thesis, the software package TOPAS of Bruker AXS was used for Rietveld analysis [86]. If a large number of diffraction patterns are recorded, the integrated patterns can be batch-analyzed with TOPAS. However, during in-situ heating (or cooling) experiments, changes in lattice parameter due to thermal expansion and possibly rapid changes in phase fractions make it difficult to obtain consistent fits of good quality throughout the experiment. Due to this reason, a different approach was used for phase analysis. Here, the area of all discernible peaks of one phase was calculated by fitting a Gaussian to each peak. This was performed for all phases present in the specimen. To obtain the phase fractions, the cumulative peak areas of all phases are multiplied by a weighting factor. The weighting factor is calculated from reference measurements where the phase fractions were determined by a complementary method. To find accurate weighting factors, selected patterns were subjected to a Rietveld analysis [25]. Once these values were known, fitting of the peaks was performed with a Python routine that was specifically designed by the author to serve this purpose.

It should be noted here that Rietveld analysis of patterns acquired during in-situ heating experiments suffers from an additional limitation. To be able to fit the pattern, the crystal structures and the site occupancies of the phases present must be provided. If all phases in TiAl alloys would maintain their stoichiometric composition at all times this would be an easy task. As already elaborated in Chapter 2.4, this is not the case. The chemical composition of all phases varies with changes in temperature, and thermodynamics dictate that the degree of disorder in ordered phases increases as temperature rises [87]. To obtain exact results from the Rietveld analysis, these factors must be taken into account. It is,

however, impractical to provide the exact chemical compositions of all phases for every temperature at which a diffraction pattern was acquired. Therefore, it is suggested to determine chemical compositions only for a few data-points and use them for interpolation. Since the effect of small changes in site occupancy and chemical composition has limited influence on the phase fractions determined by means of Rietveld analysis, using an approximate value for these parameters was found to be sufficient.

One factor that significantly complicates the quantitative evaluation of phase fractions are the close structural similarities between the important phases in γ-TiAl alloys. These similarities (discussed in some detail in Chapter 2) are responsible for the severe peak overlaps observed in the diffraction patterns (see Figure 8). Additionally, especially at high temperatures, an increased background noise is observed around the peaks of highest intensity which is believed to stem from fluorescence and thermal diffuse scattering [28]. In combination, these effects are detrimental to the exact determination of lattice parameters and can lead to difficulties if phases with similar structures are to be distinguished (e.g. α_2 and B19, see Figure 8). Grain coarsening during an in-situ experiment might decrease the pattern quality dramatically. For the case that phase fractions under equilibrium conditions are desired, a compromise must be made between allowing enough time to approach equilibrium and maintaining sufficient grain statistics. To gain information on the rate-dependence of phase transformations, experiments can be performed at different heating/cooling rates and the effect on the phase transition temperatures can be evaluated (e.g. [37]).

Data analysis of experiments targeted to investigating the precipitation behavior of γ-phase from supersaturated α_2 upon heating might be biased by an additional phenomenon. As γ lamellae precipitate, the occurrence of severe streaking is observed. This was already reported by Liss et al. [88] and attributed to the finite thickness of the lamellae, lattice parameter gradients and diffuse scattering. Intensive streaking might lead to broader peaks in the integrated pattern and thereby decrease the ability to separate individual peaks.

One pitfall that is not directly related to data analysis but can lead to erroneous results nonetheless is the establishment of a correct temperature measurement. Although this might seem to be a trivial problem it was found to be quite persistent in the course of this thesis. In early experiments, a pyrometer was used for controlling the specimen temperature. Despite the fact that this seemed to work, it was found that the phase transition temperatures determined in the in-situ experiment did not correspond to the ones found by means of DSC (Appendix C).

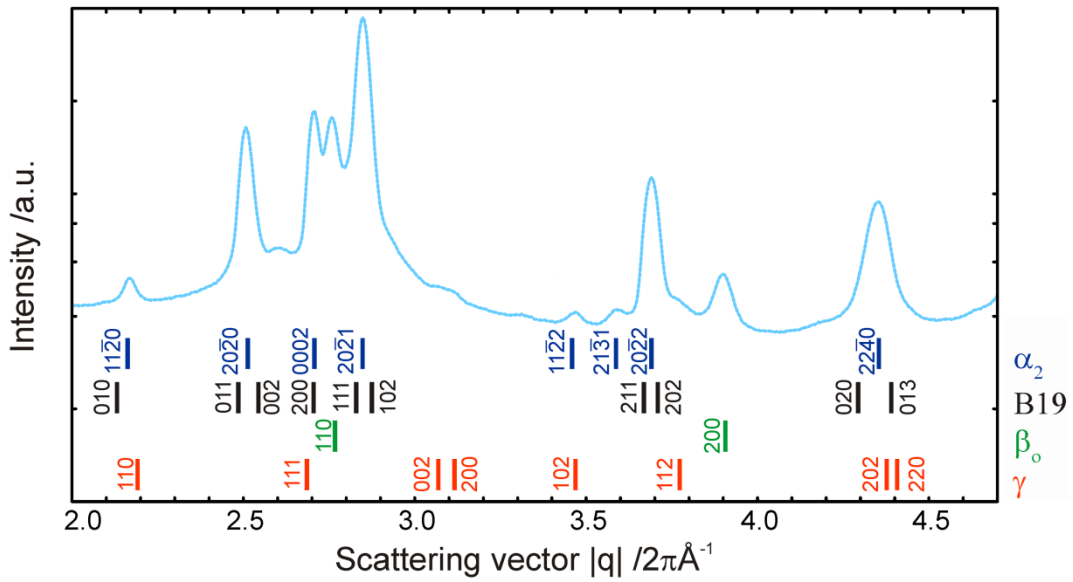

Figure 8: Diffraction pattern of a Ti-45 Al-3 Mo-0.1 B alloy heat-treated in the β single phase field region and subsequently quenched. The peak positions of the individual phases are indicated below the pattern. It is obvious that especially the main peaks between q=2.5 and q=3 A^{-1} show severe overlapping (see also Appendix F).

When a pyrometer was used while the specimen rotated in the beam, it was discovered that the temperature readings followed a sine wave. This behavior can be attributed to a variation in emission coefficients on the specimen surface, presumably due to the formation of an oxide layer on the surface. Although a differential pyrometer was used which is supposed to take the emission coefficient into account, it was confirmed that the temperature measured did not consistently reflect the actual specimen temperature by means of a thermocouple. Thermocouples are an accurate and user-friendly method for measuring temperatures up to 1300 °C on TiAl specimens. If long-term experiments are performed, the thermocouple might degrade due to a change in chemical composition induced by diffusion between the thermocouple and the specimen. This, however, can be disregarded for in-situ diffraction experiments since the limited amounts of beam-time do not allow for such experiments. Of greater concern is the fact that Pt, which is the main constituent of types S and B thermocouples used at high temperatures, forms a eutectic alloy in the binary Ti-Pt diagram at 1310 °C [89–91].

Consequently, the thermocouple separates from the specimen surface and the experiment must be terminated. A solution to this problem was found in spot-welding a small piece of Mo or Ta to the specimen to which, in turn, the thermocouple is welded. Although this is somewhat tricky and a fair percentage of the refractory-metal plates detach during the experiment it gives a valid temperature reading and allows performing experiments up to about 1450 °C.

4 The Investigation of Dynamic Processes during Hot-Deformation by means of High-Energy X-Ray Diffraction

At elevated temperatures, metals and many ceramics experience changes in their microstructure. Especially if grains exhibit high defect densities, a multitude of different mechanisms can take place all of which decrease the energy stored within the material. Generally, these mechanisms are classified into two groups, depending if the movement of high-angle grain boundaries (HAGBs) is involved or not [92,93]. During recovery, the density of point defects decreases and dislocations arrange themselves into low-energy configurations [92,94]. Recrystallization involves the movement of HAGBs which sweep through the material and form new grains with low defect densities [92]. Another distinction is made based on whether the recovery and recrystallization mechanisms occur during deformation or not. Static recovery (RV) and recrystallization (RX) are frequently observed after the material has been deformed at low temperatures and the driving force is therefore the stored energy of cold work. Dynamic recovery (DRV) and dynamic recrystallization (DRX), however, occur while the material is being deformed at high temperatures (e.g [93–95]).

Recovery and recrystallization have long been (and are still) subject of intensive research efforts and a vast number of publications concerned with these effects are available. One of the many difficulties associated with this research is that it is difficult to gain information on these processes in-situ. A common way of performing experiments is to make a series of deformation or annealing experiments and stop them for different specimens at different times. By performing post-mortem analysis, information on the microstructural development can be gained. Especially if recrystallization or discontinuous grain growth is regarded, very few, sometimes tiny nuclei are responsible for the future microstructural development [93]. Not being able to follow the evolution of one nucleus during recrystallization or discontinuous grain growth hampers research progress in this area. One method that has a promising prospect is the three-dimensional X-ray diffraction (3D-XRD) method by which it is possible to obtain a dataset in which the grain shapes and the grain orientations within the investigated volume are contained. Currently the spatial resolution of this method is in the range of µm and the maximum number of grains is in the range of 10^3 [96]. For details on the 3D-XRD method, the reader is referred to the corresponding literature [97–99]. Today, however, this method is not fast enough to obtain the data really in-situ. Instead, the experiment is performed in a stepwise fashion. While such experiments are well suited for investigating static annealing phenomena, it is impossible to gain information about dynamic processes.

In an attempt to close this gap, Liss et al. [35] have developed an in-situ method that is based on a simple powder diffraction setup used at a synchrotron source. This method does not allow observing the behavior of all grains in the illuminated volume, but it enables

to draw conclusions from the behavior of individual reflection spots on the Debye-Scherrer rings. Under the assumption that the behavior of the grains observed is representative for the entire specimen, new, previously inaccessible information can be gained on the behavior of materials during thermo-mechanical processing.

4.1 Experimental Method

A prerequisite for monitoring individual grains in a powder diffraction experiment is that single diffraction spots are discernible in the diffraction pattern, i.e. that a sufficiently low number of crystallites is illuminated. Another requirement is that of a fast detector. The minimum frame rate depends on the strain rate applied to the specimen. For the experiment published by Liss et al. a strain rate of $2.6\times10^{-3}\ s^{-1}$ was adjusted and approximately two images were recorded per second [34] (Appendix E). For the experiments performed in the course of this thesis, an Instron ETMT (electro thermo-mechanical tester) compression rig was installed in the synchrotron beam. Specimens were heated resistively while temperature control was obtained by a type-S thermocouple spot welded to the specimen surface. Since the ETMT has only one moving anvil the specimen moves laterally with respect to the beam while being deformed. The motorized table on which the ETMT was mounted was controlled in such a way as to counteract the lateral displacement of the specimen. To reduce friction, a graphite foil was placed between the specimen and the anvils while a Ta foil prevented diffusion between the graphite foil and the specimen. For specifics concerning the experimental the reader is referred to the appended publication (Appendix C).

4.2 Data Analysis and Interpretation

During one in-situ compression experiment, several hundred diffraction images should be obtained to enable data analysis and interpretation. This large amount of data necessitates the use of automated algorithms for compiling the acquired data into a format that allows interpreting them. In the following, the procedure that produces the diagrams that were first introduced by Liss et al. [34,35] shall be elaborated. First, the Debye-Scherrer ring for which the AT-plot shall be constructed is chosen and its 2Θ position determined. Next, the intensity is integrated over a small angular range around the line position of the ring (Figure 9). This range is adjusted in such a way as to include all spots of one ring, and should be as small as possible to improve the signal-to-noise ratio of the analysis. Resulting from this the integrated intensity is attained as a function of azimuthal angle for one diffraction pattern. The process of constructing an AT-plot from a series of detector images is shown schematically in Figure 10. This routine is applied to all detector images acquired and the azimuthal-angle time plot (AT-plot) is assembled in a diagram where the pattern number (which is equivalent to the time) is plotted on the horizontal axis, the azimuthal angle is indicated on the vertical axis, and the intensity is shown in grey-scale (Figure 11).

Once AT-plots have been established for several reflections of all phases, the question arises how these plots are to be interpreted. A line that indicates the angular position of a single grains reflection over time is henceforth called a timeline [34]. Parallel timelines, as visible in Figure 11 at t<180 s, are caused by the reflections of grains which remain static. If grains rotate about an axis parallel to the incident beam, the timeline is tilted. For the case that the grain rotates about an axis that is not parallel to the beam, the Bragg condition is lost and the reflection is no longer visible on the Debye-Scherrer ring. In addition to this, the width of the reflection gives information about the defect density of the corresponding grain. In Figure 12, the effects of different microstructural processes on the reflection spots are illustrated. During hot-deformation, a high number of defects are generated (Figure 12 d) which leads to peak-broadening. If the material accommodates the defects predominantly by means of dynamic recovery, dislocations annihilate, climb and arrange themselves in low-energy configurations such as low-angle grain boundaries (LAGBs) (Figure 12 b) [92].

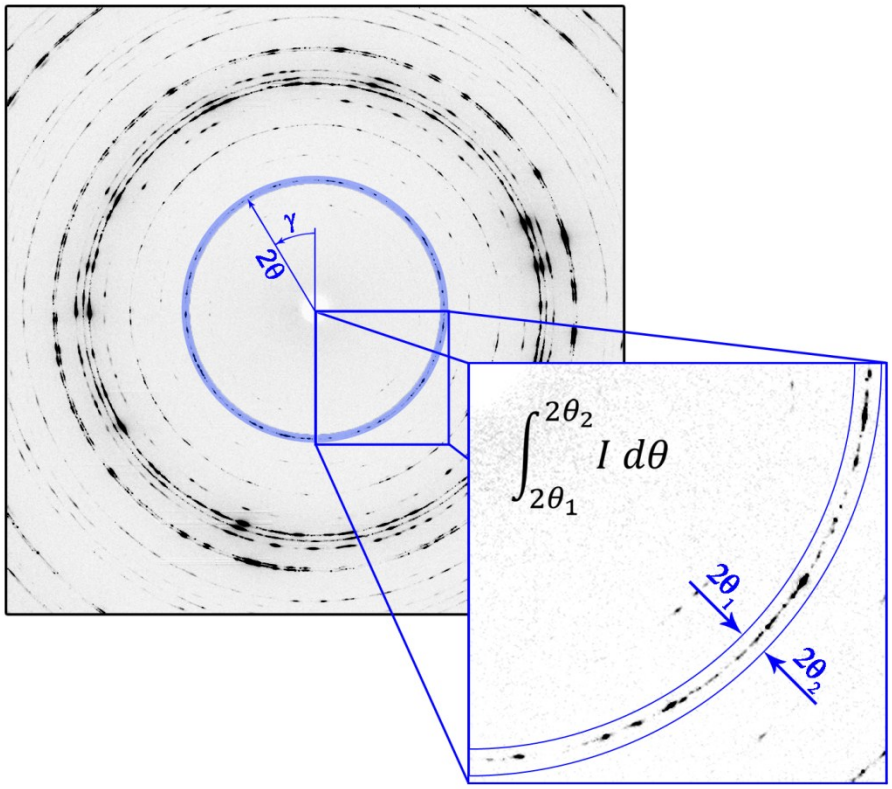

Figure 9: Schematic showing how an AT-plot is compiled. The selected Debye-Scherrer ring is high-lighted and the limits for the integration of the intensity (*I*) over the Bragg-angle (2*Θ*) are indicated. To attain an AT-plot, the integrated intensity is plotted as a function of the azimuthal angle *γ* (see inset) [100].

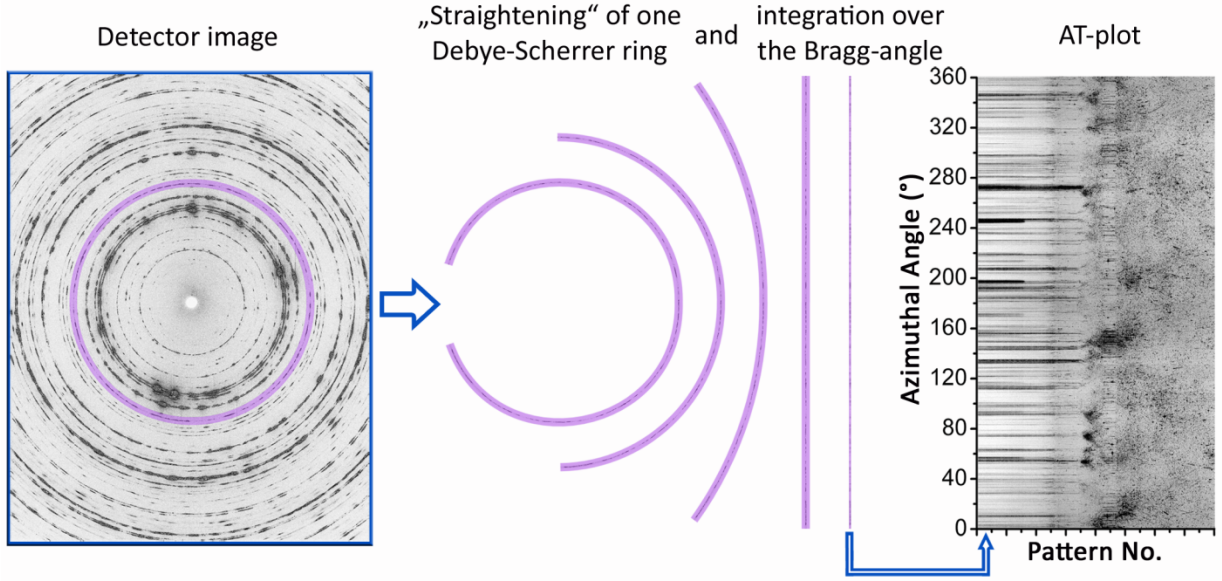

Figure 10: Image illustrating how an AT-plot is constructed from a series of detector images. A typical AT-plot is constructed from several hundred detector images.

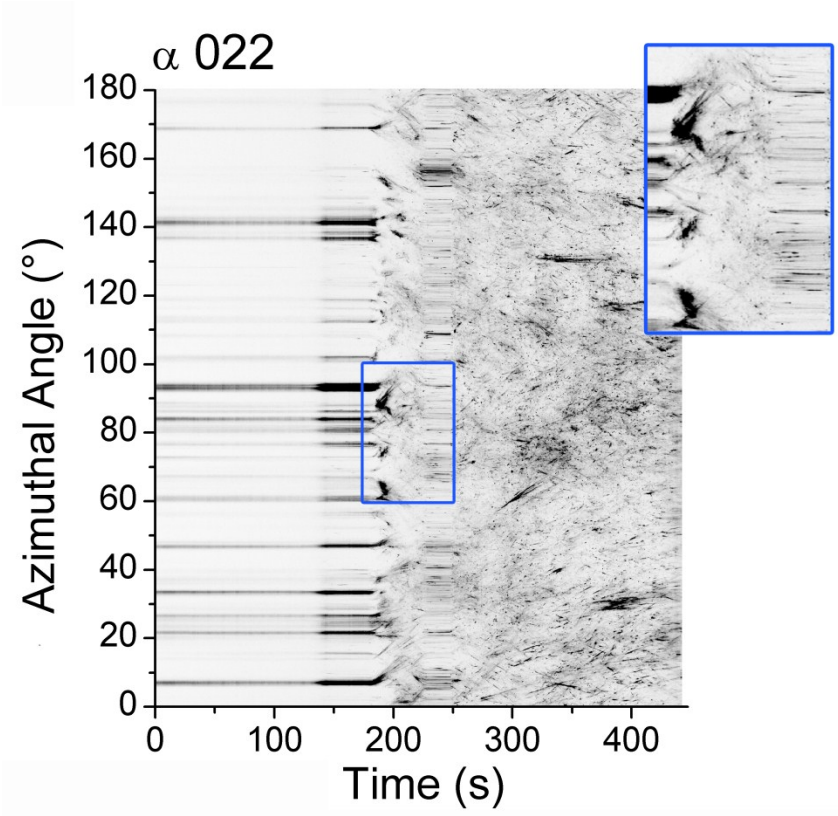

Figure 11: AT-plot of the α 022 reflections obtained on a TNM™ alloy during compression at a rate 0.0038 s^{-1} at 1300°C. During heating, parallel timelines are observed. As soon as deformation starts, the timelines tilt.

This effect can lead to a gradual increase in misorientation across the LAGB so that it transforms, eventually, into a HAGB (Figure 12 c). This is reflected by a bifurcating timeline in the AT-plot if the two sub-grains are rotated parallel to the beam axis. Otherwise the reflection spot diminishes and vanishes as the grains lattice ceases to satisfy the Bragg condition. Dynamic and static recrystallization lead both to the formation of new grains with low defect densities. Consequently a number of sharp reflection spots appear which grow in intensity at the expense of the parent grain (Figure 12 e).

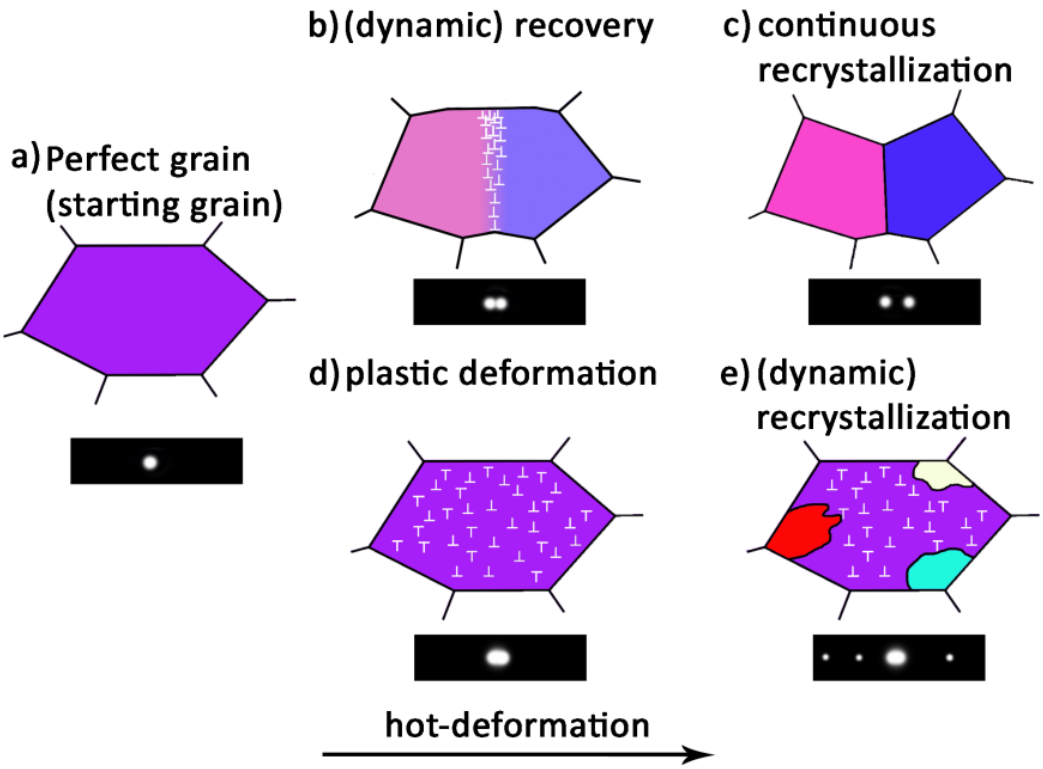

Figure 12: Dislocation and grain boundary arrangements in the material and their influence on the diffraction spots. The strain increases from left to right [25] (see also Appendix A).

In Figure 13, magnified sections of AT-plot illustrate the development of diffraction spots for different microstructural processes. Rotation of a grain about an axis parallel to the incident beam leads to the formation of a tilted timeline (Figure 13 a). The fact that the timeline remains sharp points toward the fact that the defect density is constant during the observed period. When defects within a grain arrange themselves into a LAGB, different regions of the grain diffract the incident intensity differently and the reflection spot bifurcates (Figure 13 b). It should be born in mind that also in this case the rotation axes must be parallel to the incident beam that both regions of the grain continue to satisfy the Bragg condition. If solely dislocation multiplication occurs within a grain during forming, the corresponding diffraction spots broaden. This condition is presented in Figure 13 c.

Recrystallization is indicated by the formation of new grains with low defect density within a microstructure with high defect densities. Consequently, RX images in the AT-plot as appearance of sharp reflection spots while many other timelines or spots are blurred. This condition is depicted in Figure 13 d, where the sudden appearance of sharp spots during hot-deformation indicates the occurrence of DRX.

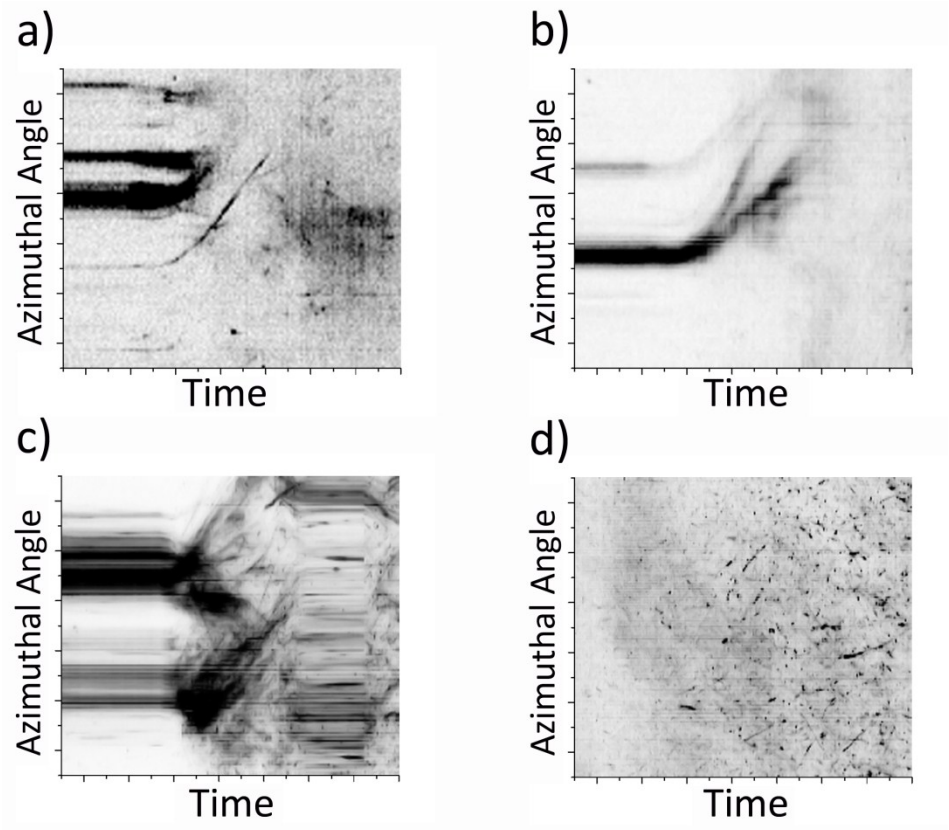

Figure 13: Effect of different microstructural processes on the development of diffraction spots. Rotation of a grain about an axis parallel to the beam is shown in (a). In (b), a diffraction spot bifurcates due to the formation of a LAGB. Broadening of spots is caused by the introduction of defects in the grain (c). If DRX occurs, sharp reflection spots appear from a diffuse background (d) (Appendix D).

Additionally, the formation of texture can easily be monitored in-situ with this method. Here, instead of regarding individual grains and spots, the intensity distribution of one Debye-Scherrer ring over the azimuthal angle γ is evaluated.

With this method, however, it is not possible to track individual grains throughout the entire compression experiment. Grains are only observed for short periods of times, namely, as long as they fulfill the Bragg condition. Nonetheless, is it possible to derive the behavior of the majority of grains from several AT-plots of one phase. Ideally, this method is

complemented with microscopic methods which allow investigating the microstructure post mortem.

Future improvements can be made by incorporating analysis of the average and individual peak widths. This would allow determining mean defect densities or even defect densities of a number of individual grains. Furthermore could an algorithm be implemented that enables attributing e.g. twin-reflections to parent grains. To make such improvements possible, further work on less complex material systems would be necessary. TiAl alloys are not well suited for this task, since effects like lamellar colonies and involved streaking complicate performing such fundamental development.

5 Complementary Methods

Diffraction methods offer the opportunity to investigate a number of material parameters in-situ. What these methods (with the exception of 3D-XRD) cannot provide is information about the morphology and arrangement of grains. For this reason, microscopic methods were used extensively to complement and confirm the findings of the in-situ diffraction investigations.

If information on transformation temperatures is desired, thermal analysis methods can yield valuable data. In this thesis these methods were primarily used to verify temperature recordings due to the fact that an accurate temperature measurement was difficult to establish (see Chapter 3.3). In the following, a short introduction to each of the methods employed is given.

5.1 Scanning Electron Microscopy and Electron Back-Scatter Diffraction

By means of SEM it is possible to obtain microstructural images from low to rather high magnifications. For TiAl specimens, fast and reliable metallographic preparation methods such as mechanical polishing or electrolytic polishing exist and are extensively treated in [101,102]. In this thesis microstructural images were obtained in BSE mode. It should be noted that the contrast between the phases in TiAl alloys is rather poor and that high beam currents are necessary to achieve images of sufficient quality. The use of an SEM equipped with a field emission gun (FEG) significantly improves the contrast and the sharpness of the micrographs. In the course of this thesis, the SEM was the workhorse for microstructural characterization of TiAl specimens. Most of the images were obtained at a ZEISS Evo 50 (ZEISS, Oberkochen, Germany).

EBSD was used for investigating the orientations and subgrain structures in hot-deformed specimens. Specimens were prepared by means of electrolytic polishing of a ground and mechanically polished surface. Information on the EBSD technique can be found in [103]. EBSD images were acquired on a Zeiss LEO FEG-SEM equipped with an EDAX EBSD system. The structural similarities between the phases present make it difficult to distinguish them in specimens with a high density of stored dislocations. Nonetheless was it possible to extract valuable information that complements the data obtained by HEXRD.

5.2 Differential Scanning Calorimetry

DSC experiments can be utilized to investigate a number of different solid state reactions such as phase transformations, precipitation, and recrystallization. Quantitative studies are possible by employing a Johnson-Mehl-Avrami method or activation energy analysis [104]. For literature on DSC methods, the reader is referred to [105,106]. In this thesis, however, DSC was only used to evaluate phase transformation temperatures in the investigated TiAl alloy system. To this end, experiments were performed at different heating

rates. The transformation temperature under equilibrium conditions was then calculated by linear extrapolation of the results to a heating rate of 0 $Kmin^{-1}$ [24]. All experiments were performed with a Setaram Labsys Evo (SETARAM, Caluire, France). Experimental details are given in Appendix E and for a schematic experimental setup, the reader is referred to [37].

5.3 Dilatometry

In dilatometry, the length of a specimen is recorded dependent on its temperature. Many phase transformations and precipitation reactions are associated with a change in specific volume and can therefore be investigated in the dilatometer [107]. For this thesis, mainly a modified Bähr DIL 805 dilatometer was used for performing in-situ experiments at the DORIS synchrotron source at DESY, Hamburg, Germany. For a short description of this device and its use in the synchrotron beam, the reader is referred to [108]. As a complementary method, dilatometry offers the possibility to observe phase transformations upon fast heating or cooling. Even if a fast state-of-the-art detector is used for in-situ diffraction experiments, the frame rates achieved are in the order of 1-10 Hz at best. In the dilatometer, the data acquisition rate is much higher which allows recording additional data points which can supplement the diffraction data.

6 Summaries of Appended Papers

TiAl alloys are intermetallic materials on the verge to commercial production. Although intense research effort was put into the development of this materials class for the last 20 years, several aspects of these materials class are still to be explored. The rapid development of characterization methods enables us today to gain new insights in the materials behavior. In the following some topics that were addressed in the course of this thesis are listed.

It would be highly beneficial to be able to calculate ternary or even quaternary phase diagrams for γ-TiAl based alloys. Although a thermodynamic database exists for the TiAl system it was shown by three publications of this thesis to yield inadequate results if applied to advanced γ-TiAl based alloys (see 6.1, 6.2, 6.3). Instead the phase fractions as functions of temperature were derived from experimental data. These results are now used in the framework of a different thesis to improve the existing thermodynamic database and ultimately be able to calculate phase diagrams also for high Nb and Mo containing TiAl alloys.

Cost-effective forming operations are a prerequisite for the widespread use of TiAl parts in different applications [1,2]. A near-conventional forging procedure was established for the TNM™ alloy family at temperatures significantly higher than those used for isothermal forging of different members of the γ-TiAl alloy family (~1150 °C) [17,49,109]. At these temperatures, dynamic processes such as recovery or recrystallization occur fast and rapid phase transformations upon cooling make it difficult to investigate them post-mortem. Therefore, a novel in-situ diffraction technique was applied that yielded new insights into the deformation behavior of γ-TiAl base alloys at high temperatures (see 6.4, 6.5).

In TiAl+M alloys (where M stands for Mo, Nb or combinations of the two elements) phases with low symmetry can be formed even at temperatures expected to occur under service conditions. Since the formation of such phases is usually associated with embrittlement of the material, this is of great concern for potential applications of these alloys. Formation and dissolution of a phase with B19 structure was observed during HEXRD experiments on a heat-treated and quenched specimen and is reported on in one of the following publications (6.6).

6.1 The Contribution of High-Energy X-Rays and Neutrons to Characterization and Development of Intermetallic Titanium Aluminides (Appendix A)

This publication is a review published in the special issue “Applications of Photons and Neutrons for the Innovation of Engineering Materials” of Advanced Engineering Materials. The focus of the paper lies on introducing the reader to different aspects of performing in-situ diffraction experiments on TiAl alloys and on the evaluation of the data generated thereby. For each topic, the existing literature is recapitulated and examples from own research are given. Special focus is put on the complementary nature of X-ray and Neutron diffraction experiments in the case of TiAl alloys and the consequences are discussed. Many in-situ experiments are concerned with the evolution of phase fractions with temperature and the order to disorder transitions upon heating and cooling. For these experiments, the main challenges like maintaining a valid temperature reading and taking the elevated noise level around the main peak positions into account are described. Experiments where the phase fractions as a function of temperature are investigated are sought to reflect the materials behavior under equilibrium conditions. In contrast to this, some experiments were performed in which phase transformations of metastable microstructures were of interest. Precipitation of γ lamellae from supersaturated α_2 grains is one example for phase transformations which can occur at rather high rates. Another vital part of the review is the brief description of the diffraction method proposed by Liss et al. [34,35] which enables investigating dynamic processes during hot working. For emphasizing the advantages and drawbacks of this method, It is put in the context of other emerging techniques in the field of X-ray diffraction methods such as 3D-XRD (e.g. [97,110]) and µ-Laue techniques (e.g. [111,112]). Covering these different fields the paper is intended to provide a hands-on guide to investigating engineering materials by means of diffraction techniques.

6.2 In-situ Diffraction Experiments for the Investigation of Phase Fractions and Ordering Temperatures in Ti-44 at% Al-(3-7) at% Mo Alloys (Appendix B)

In γ-TiAl alloys of the TNM™ type, Mo and Nb are used for stabilizing the β/β_o-phase which improves the hot-deformation characteristics and facilitates solidification via a β single-phase field. For investigating the effect of Mo additions on phase fractions and transition temperatures, two alloys with nominal compositions of Ti-44 Al-3 Mo and Ti-44 Al-7 Mo were produced. Specimens were then investigated by means of in-situ HEXRD experiments during which they were heated continuously to temperatures of 1350 °C. Order to disorder transition temperatures were determined by additional in-situ neutron diffraction experiments. The diffraction patterns obtained were used to determine the

phase fractions as functions of temperatures for the two alloy compositions. These data are compared with the appropriate quasi-binary sections of two Ti-Al-Mo ternary phase diagrams derived from thermodynamic calculations based on the CALPHAD method and literature data. It is shown that the calculated phase diagram did not correspond to the experimentally determined values. In contrast to that the phase diagram derived from literature data seems to fit better to the experimental data. Moreover, additional data for the correct thermodynamic modeling of ternary Ti-Al-Mo alloys were generated by this study.

6.3 Phase Fractions, Transition and Ordering Temperatures in TiAl-Nb-Mo Alloys: An In and Ex-situ Study (Appendix C)

Alloys of the TNM™ family attain their good hot-working characteristics by high amounts of disordered β-phase at those temperatures were the parts are formed. High creep-strength, however, can only be attained if the amount of ordered β_o-phase at service temperature is low. A prerequisite for the realization of an alloy exhibiting both, high creep resistance and good hot-working behavior is therefore a course of phase fractions over temperature that allows conducting heat-treatments which minimize the β/β_o-phase fraction after the forming operation. To this end, the curve of β/β_o-phase fraction over temperature has to have a minimum at temperatures high enough to attain a condition close to the equilibrium within a reasonable amount of time.

To find an alloy composition that shows this kind of behavior, three alloys with slightly different compositions were produced. Specimens of each alloy variant were investigated in-situ by means of HEXRD and neutron diffraction. In the HEXRD experiment, the phase fractions were determined as functions of temperature. Neutron diffraction experiments yielded the order to disorder transformation temperatures. Additionally, specimens were heat-treated and quenched prior to metallographic preparation and ensuing examination to verify the results obtained by the in-situ methods. The study showed that thermodynamic calculations performed for the investigated alloy compositions [2] did not reflect the observed behavior. Furthermore, it was possible to identify the alloy composition which is suited best for the adjustment of high β-phase contents during hot-forming and low β_o-phase fractions at operating temperatures.

6.4 An In-situ High-Energy X-Ray Diffraction Study on the Hot-Deformation Behavior of a β-Phase Containing TiAl Alloy (Appendix D)

Dynamic microstructural processes occurring during hot-forming operations critically determine the properties of the finished parts and components. Since TiAl alloys are frequently processed at high homologous temperatures (which also translates to high absolute temperatures), dynamic processes are expected to occur at high rates. Up to now, dynamic recovery and recrystallization processes in TiAl alloys were investigated by

performing instrumented hot deformation experiments and post mortem microscopic examinations of the specimens, e.g. [34,49,113–117].

In this publication the deformation behavior is monitored in-situ by means of the method developed by Liss et al. [34,35]. Previously to discussing the results of this study, the relevant mechanisms governing dynamic recovery and recrystallization are introduced and the corresponding literature is discussed. Coupling the in-situ diffraction technique with post-mortem EBSD investigations enabled to gain new insights into the microstructural evolution of TiAl specimens during hot-deformation. Hot-compression experiments were performed at 1300 °C (in the α+β phase field region) and at 1220 °C where, α, β, and γ are existent. It was possible to identify dynamic recovery as the dominant mechanism accommodating defects in the β-phase. As far as the α-phase is concerned, dynamic recovery is dominant at 1300 °C, whereas at 1220 °C also dynamic recrystallization seems to be of relevance. At 1220 °C γ-phase is present in the microstructure and dynamically recrystallizes during deformation. Additionally, the anisotropic deformation behavior of lamellar colonies was directly observed during the deformation experiment.

6.5 In-situ Study of Dynamic Recrystallization and Hot Deformation Behavior of a Multiphase Titanium Aluminide Alloy (Appendix E)

Performing hot-compression experiments in a synchrotron beam while a fast detector records the whole diffraction patterns allows investigating processes such as dynamic recovery and dynamic recrystallization. Furthermore, orientation relations between grains of different phases can be identified and information about textural development can be retrieved. To this end, the morphology of individual spots lying on Debye-Scherrer rings as well as the distribution of the spots on the ring are evaluated. Furthermore, the development of these parameters over time can be tracked if a sufficiently fast detector is used and yields valuable information on the dynamic processes occurring. In this publication a Ti-43.5 Al-4 Nb-1 Mo-0.1 B alloy was deformed at a temperature of 1300 °C. The data gained are represented by a so-called AT-plot (azimuthal angle-time plot) and exemplarily discussed. It was found that processes occur fast in the disordered β-phase, whereas the disordered α-phase shows a comparably sluggish recovery and recrystallization behavior.

6.6 In-situ Synchrotron Study of B19 Phase formation in a TiAl Alloy (Appendix F)

As already mentioned in Chapter 2, a number of phases with lower symmetry exists in TiAl alloys in addition to the three main phases (α_2, β_o, γ) and their disordered polymorphs [40]. One of these phases is the B19 phase which is of orthorhombic structure and is closely related to all main phases occurring in γ-TiAl based alloys. The existence of B19 phase was already reported earlier by Abe et al. [57] and Tanimura et al. [64] as well as

by Appel et al. [61]. All these studies were conducted by means of TEM on specimens that were either quenched or subjected to an annealing treatment after quenching. None of these previous studies was able to specify the temperature range in which the phase formed.

In the current study, a Ti-45 Al-3 Mo-0.1 B alloy was heat-treated at 1335 °C for 10 min and subsequently water quenched. After that, the specimen was heated at two different rates while X-ray diffraction patterns were continuously recorded. Originally it was only intended to investigate the change in lattice parameter with temperature for the quenched α_2-phase in this experiment. During data evaluation, however, it became obvious that a new phase was formed before γ-phase precipitated. Since this phase dissolved again as the formation of γ progressed it was concluded that a transitional phase had been observed.

A detailed analysis revealed that this transitional phase is of the B19 type and that all of the α_2-phase transformed to this transient structure before it decomposed into α_2 and γ again. Additionally, the temperatures of formation and dissolution were determined. It was shown that these temperatures are strongly dependent on the heating rate which suggests that diffusion processes govern the observed phase transformations. Furthermore, the crystallographic relations between the occurring phases are discussed in this publication.

7 Conclusion

Although intermetallic γ-TiAl alloys have been subject of intensive research efforts for more than two decades, a number of questions remain elusive. Among these challenges is the fact that calculation of phase fractions still suffers from insufficient thermodynamic databases, especially in the case of order to disorder transformations. Also, it is known that metastable low-symmetry phases may form in Nb and Mo containing TiAl alloys, but information on the chemical and temperature regimes of existence is scarce. Furthermore, little is known about the dynamic microstructural processes occurring during hot-working despite the fact that alloys have been developed that can be forged under near-conventional conditions.

In this thesis, it was attempted to address these problems by investigating advanced γ-TiAl alloys by means of in-situ synchrotron and neutron diffraction experiments. High-energy X-rays allow illuminating a large specimen volume and enable conducting fast in-situ experiments due to the high brilliance of the beam. Small diffraction angles are advantageous if large equipment is needed, e.g. for heating or deformation of a specimen. Fast flat-panel detectors can be operated at frame rates of up to two Hz and offer new possibilities for investigating dynamic processes.

Phase fractions and ordering temperatures were studied in TNM™ and various TiAl+Mo alloys. From the results of the study performed on TNM, the alloy composition suited best for adjusting tailored microstructures was derived, e.g. Ti-43.5 Al-4 Nb-1 Mo-0.1 B. Experiments on TiAl+Mo alloys revealed that the phase diagrams calculated with the CALPHAD approach yields erroneous results while a phase diagram constructed from literature data reflects the experimental results better.

The B19 phase was found to occur upon heating of a previously heat-treated and quenched Ti-45 Al-3 Mo alloy. It occurred only as a transient phase and facilitated the transformation from the quenched α_2-phase to γ. Further work will be necessary to be able to specify the entire field of existence of this phase.

By means of a novel in-situ method, the hot-deformation behavior of TNM was investigated. With this method, it is possible to observe the microstructural processes that accommodate plastic deformation in the material during a high-temperature compression experiment. While the setup is similar to that of a powder diffraction experiment, low grain statistics allow distinguishing individual spots. Consequently, information on individual grains can be retrieved. Although providing much less information than 3D-XRD, this method is sufficiently fast to be conducted during deformation which is not possible with the 3D-XRD technique. It was found that the deformation is inhomogeneously distributed within grains of the same population and that recrystallization and recovery occur at different temperatures in different phases.

In the future, faster detectors and more powerful light sources will promote the use of high-energy X-rays in materials science. Emerging techniques such as 3D-XRD will be able to provide spectacular new insights into the behavior of materials, also under extreme conditions. Without a doubt these techniques will also be used to investigate future generations of TiAl alloys as the alloy development progresses and the maximum temperatures at which these alloys can be used increase. It cannot be fathomed where the development of methods and materials will take us, but without a doubt, the journey will be an exciting one.

8 References

[1] H. Clemens, W. Smarsly, Advanced Materials Research 278 (2011) 551-556.

[2] H. Clemens, W. Wallgram, S. Kremmer, V. Güther, A. Otto, A. Bartels, Advanced Engineering Materials 10 (2008) 707-713.

[3] F. Appel, R. Wagner, Materials Science and Engineering: R: Reports 22 (1998) 187-268.

[4] E.A. Loria, Intermetallics 8 (2000) 1339-1345.

[5] Y.-W. Kim, H. Clemens, A. Rosenberger (Eds.), Gamma Titanium Aluminides 2003, TMS (The Minerals, Metals & Materials Society), Warrendale, PA, USA, 2003.

[6] H. Clemens, H.F. Chladil, W. Wallgram, B. Böck, S. Kremmer, A. Otto, V. Güther, A. Bartels, in:, Y.-W. Kim, D. Morris, R. Yang, C. Leyens (Eds.), Structural Aluminides for Elevated Temperatures, TMS (The Minerals, Metals & Materials Society), New Orleans, LA, 2008, pp. 217-228.

[7] F. Appel, J.D.H. Paul, M. Oehring, Gamma Titanium Aluminide Alloys: Science and Technology, Wiley-VCH, Weinheim, Germany, 2011.

[8] X. Wu, Intermetallics 14 (2006) 1114-1122.

[9] F. Appel, J.D.H. Paul, M. Oehring, H. Clemens, F.-D. Fischer, International Journal of Materials Research (formerly Zeitschrift Fuer Metallkunde) 95 (2004) 585-591.

[10] H. Clemens, H. Kestler, Advanced Engineering Materials 2 (2000) 551-570.

[11] M. Yamaguchi, H. Inui, K. Ito, Acta Materialia 48 (2000) 307-322.

[12] H. Kestler, H. Clemens, in:, C. Leyens, M. Peters (Eds.), Titanium and Titanium Alloys, WILEY-VCH, Weinheim, Germany, 2003, p. 351.

[13] A. Lasalmonie, Intermetallics 14 (2006) 1123-1129.

[14] T. Tetsui, K. Shindo, S. Kaji, S. Kobayashi, M. Takeyama, Intermetallics 13 (2005) 971-978.

[15] T. Tetsui, K. Shindo, S. Kobayashi, M. Takeyama, Scripta Materialia 47 (2002) 399-403.

[16] T. Tetsui, K. Shindo, S. Kobayashi, M. Takeyama, Intermetallics 11 (2003) 299-306.

[17] W. Wallgram, H. Clemens, S. Kremmer, A. Otto, V. Güther, in: Materials Research Society Symposium Proceedings, 2008.

[18] M. Grujicic, Y. Zhang, Journal of Materials Science 34 (1999) 1419–1437.

[19] J.-D. Shi, Z. Pu, Z. Zhong, D. Zou, Scripta Metallurgica et Materialia 27 (1992) 1331-1336.

[20] M. Schloffer, F. Iqbal, H. Gabrisch, E. Schwaighofer, F.-P. Schimansky, S. Mayer, A. Stark, T. Lippmann, M. Göken, F. Pyczak, H. Clemens, Intermetallics 22 (2012) 231-240.

[21] T. Schmoelzer, K.-D. Liss, G.A. Zickler, I.J. Watson, L.M. Droessler, W. Wallgram, T. Buslaps, A.J. Studer, H. Clemens, Intermetallics 18 (2010) 1544-1552.

[22] F.-S. Sun, C.-X. Cao, S.-E. Kim, Y.-T. Lee, M.-G. Yan, Metallurgical and Materials Transactions A 32 (2001) 1573-1589.

[23] D. Hull, D.J. Bacon, Introduction to Dislocations, 4th Ed., Butterworth-Heinemann, Oxford, UK, 2001.

[24] H.F. Chladil, H. Clemens, H. Leitner, A. Bartels, R. Gerling, F.-P. Schimansky, S. Kremmer, Intermetallics 14 (2006) 1194-1198.

[25] T. Schmoelzer, S. Mayer, C. Sailer, F. Haupt, V. Güther, P. Staron, K.-D. Liss, H. Clemens, Advanced Engineering Materials 13 (2011) 306-311.

[26] L. Spieß, R. Schwarzer, H. Behnken, G. Teichert, Moderne Röntgenbeugung, 2nd ed., Vieweg + Teubner, Wiesbaden, 2009.

[27] K.-D. Liss, A. Bartels, A. Schreyer, H. Clemens, Textures and Microstructures 35 (2003) 219-252.

[28] I.J. Watson, K.-D. Liss, H. Clemens, W. Wallgram, T. Schmoelzer, T.C. Hansen, M. Reid, Advanced Engineering Materials 11 (2009) 932-937.

[29] T. Schmoelzer, K.-D. Liss, P. Staron, S. Mayer, H. Clemens, Advanced Engineering Materials 13 (2011) 685-699.

[30] F. Appel, M. Oehring, in:, M. Peters, C. Leyens (Eds.), Titanium and Titanium Alloys, Wiley-VCH, Weinheim, Germany, 2003, p. 89.

[31] J.E. Daniels, M. Drakopoulos, Journal of Synchrotron Radiation 16 (2009) 463–468.

[32] K.-D. Liss, A. Bartels, H. Clemens, S. Bystrzanowski, A. Stark, T. Buslaps, F.-P. Schimansky, R. Gerling, C. Scheu, A. Schreyer, Acta Materialia 54 (2006) 3721-3735.

[33] K.-D. Liss, U. Garbe, H. Li, T. Schambron, J.D. Almer, K. Yan, Advanced Engineering Materials 11 (2009) 637–640.

[34] K.-D. Liss, T. Schmoelzer, K. Yan, M. Reid, R. Dippenaar, H. Clemens, Journal of Applied Physics 106 (2009) 113526.

[35] K.-D. Liss, K. Yan, Materials Science and Engineering: A 528 (2010) 11-27.

[36] T. Schmoelzer, K.-D. Liss, S. Mayer, K. Yan, M. Reid, R. Dippenaar, M. Peel, H. Clemens, Materials Science Forum 709 (2012) 1725-1730.

[37] H.F. Chladil, Entwicklung Und Charakterisierung Von Hoch Niob-haltigen γ-Titanaluminid Legierungen, Montanuniversität Leoben, 2007.

[38] V.T. Witusiewicz, A.A. Bondar, U. Hecht, S. Rex, T.Y. Velikanova, Journal of Alloys and Compounds 465 (2008) 64-77.

[39] O. Rios, F. Ebrahimi, Intermetallics 19 (2011) 93-98.

[40] A. Stark, Textur- und Gefügeentwicklung bei der Thermomechanischen Umformung Nb-reicher γ-TiAl-Basislegierungen, Shaker Verlag, Aachen, 2010.

[41] T. Nandy, D. Banerjee, A. Gogia, Scripta Metallurgica et Materialia 24 (1990) 2019-2022.

[42] T. Al-Kassab, Y. Yuan, C. Kluthe, T. Boll, Z.-G. Liu, Surface and Interface Analysis 39 (2007) 257-261.

[43] C. Scheu, E. Stergar, M. Schober, L. Cha, H. Clemens, A. Bartels, F.-P. Schimansky, A. Cerezo, Acta Materialia 57 (2009) 1504-1511.

[44] H. Hosoda, K. Inoue, Y. Mishima, in:, Y.-W. Kim, R. Wagner, M. Yamaguchi (Eds.), TMS Annual Meeting, The Minerals, Metals & Materials Society (TMS), Warrendale, PA, 1995, pp. 361-368.

[45] M. Takeyama, Intermetallics 6 (1998) 643-646.

[46] F. Appel, Intermetallics 8 (2000) 1283-1312.

[47] H.F. Chladil, H. Clemens, A. Otto, V. Güther, BHM 151 (2006) 356-361.

[48] H. Clemens, H.F. Chladil, W. Wallgram, G.A. Zickler, R. Gerling, K.-D. Liss, S. Kremmer, V. Guther, W. Smarsly, Intermetallics 16 (2008) 827-833.

[49] W. Wallgram, T. Schmoelzer, L. Cha, G. Das, V. Güther, H. Clemens, International Journal of Materials Research (formerly Zeitschrift Fuer Metallkunde) 100 (2009) 1021-1030.

[50] H. Clemens, B. Boeck, W. Wallgram, T. Schmoelzer, L.M. Droessler, G.A. Zickler, H. Leitner, A. Otto, in:, Mater. Res. Soc. Symp. Proc., MRS, Warrendale, 2008, pp. 115-120.

[51] Y.L. Hao, D.S. Xu, Y.Y. Cui, R. Yang, D. Li, Acta Materialia 47 (1999) 1129-1139.

[52] R. Kainuma, Y. Fujita, H. Mitsui, I. Ohnuma, K. Ishida, Intermetallics 8 (2000) 855-867.

[53] A. Menand, A. Huguet, A. Nérac-Partaix, Acta Materialia 44 (1996) 4729-4737.

[54] L.C. Zhang, G.L. Chen, J.G. Wang, H.Q. Ye, Materials Science and Engineering A 247 (1998) 1-7.

[55] H.F. Chladil, H. Clemens, G.A. Zickler, M. Takeyama, E. Kozeschnik, A. Bartels, T. Buslaps, R. Gerling, S. Kremmer, L.A. Yeoh, K.-D. Liss, International Journal of Materials Research (formerly Zeitschrift für Metallkunde) 98 (2007) 1131-1137.

[56] R. Kainuma, I. Ohnuma, K. Ishikawa, K. Ishida, Intermetallics 8 (2000) 869–875.

[57] E. Abe, T. Kumagai, M. Nakamura, Intermetallics 4 (1996) 327-333.

[58] L. Bendersky, W. Boettinger, B. Burton, F. Biancaniello, C. Shoemaker, Acta Metallurgica et Materialia 38 (1990) 931-943.

[59] T.T. Cheng, M.H. Loretto, Acta Materialia 46 (1998) 4801-4819.

[60] A. Stark, A. Bartels, H. Clemens, F.-P. Schimansky, Advanced Engineering Materials 10 (2008) 929-934.

[61] F. Appel, M. Oehring, J.D.H. Paul, Advanced Engineering Materials 8 (2006) 371-376.

[62] G. Lütjering, J.C. Williams, Titanium, 2nd ed., Springer, Berlin, 2007.

[63] D. Nguyen-Manh, D.G. Pettifor, in:, Y.-W. Kim, D.M. Dimiduk, M.H. Loretto (Eds.), Gamma Titanium Aluminides 1999, TMS (The Minerals, Metals & Materials Society), Warrendale, PA, 1999, pp. 175-182.

[64] M. Tanimura, Y. Inoue, Y. Koyama, Scripta Materialia 44 (2001) 365-373.

[65] M.J. Blackburn, in: R.I. Jaffee, N.E. Promisel (Eds.), The Science, Technology and Application of Titanium, Pergamon Press Ltd., Oxford, 1970, p. 663.

[66] L. Cha, H. Clemens, G. Dehm, International Journal of Materials Research (formerly Zeitschrift für Metallkunde) 102 (2011) 703-708.

[67] S. Mayer, C. Sailer, T. Schmoelzer, H. Clemens, T. Lippmann, P. Staron, V. Güther, M. Takeyama, BHM Berg-und Hüttenmännische Monatshefte 156 (2011) 438-442.

[68] J. Braun, M. Ellner, Zeitschrift Fuer Metallkunde/Materials Research and Advanced Techniques 91 (2000) 389-392.

[69] L.A. Yeoh, K.-D. Liss, A. Bartels, H.F. Chladil, M. Avdeev, H. Clemens, R. Gerling, T. Buslaps, Scripta Materialia 57 (2007) 1145-1148.

[70] H. Clemens, A. Bartels, S. BYSTRZANOWSKI, H.F. Chladil, H. Leitner, G. Dehm, R. Gerling, F.-P. Schimansky, Intermetallics 14 (2006) 1380-1385.

[71] V. Imayev, T. Khismatullin, T. Oleneva, R. Imayev, R. Valiev, R. Wunderlich, A. Minkow, U. Hecht, H.-J. Fecht, Advanced Engineering Materials 10 (2008) 1095-1100.

[72] H. Clemens, A. Kaysser-Pyzalla, W. Kaysser, A. Schreyer (Eds.), Application of Photons and Neutrons for the Innovation of Engineering Materials, Advanced Engineering Materials 13, 2011.

[73] W. Reimers, A.R. Pyzalla, A. Schreyer, Neutrons and Synchrotron Radiation in Engineering Materials Science, WILEY-VCH, Weinheim, Germany, 2008.

[74] L. Cha, H. Clemens, G. Dehm, Z.L. Zhang, Advanced Materials Research 146-147 (2010) 1365-1368.

[75] A. Rauch, W. Waschkowski, in: A.J. Dianoux, G. Lander (Eds.), Neutron Data Booklet, 2nd ed., Institut Laue-Langevin, Grenoble, France, 2003.

[76] N. Ashcroft, Solid State Physics, Holt Rinehart and Winston, New York, 1976.

[77] B.E. Warren, X-ray Diffraction, Dover ed., Dover Publications, New York, 1990.

[78] R. Treusch, in: W. Reimers, A.R. Pyzalla, A. Schreyer, H. Clemens (Eds.), Neutrons and Synchrontron Radiation in Engineering Materials Science, WILEY-VCH, Weinheim, Germany, 2008, p. 97.

[79] W. Knop, P. Klaus, K. Pranzas, P. Schreiner, in: W. Reimers, A.R. Pyzalla, A. Schreyer, H. Clemens (Eds.), Neutrons and Synchrontron Radiation in Engineering Materials Science, WILEY-VCH, Weinheim, Germany, 2008, p. 91.

[80] P. Debye, P. Scherrer, Nachrichten von der Gesellschaft der Wissenschaften zu Göttingen, Mathematisch-Physikalische Klasse 1916 (1916) 1.

[81] V.A. Haanappel, H. Clemens, M.F. Stroosnijder, Intermetallics 10 (2002) 293-305.

[82] A.P. Hammersley, S.O. Svensson, M. Hanfland, A.N. Fitch, D. Hausermann, High Pressure Research 14 (1996) 235-248.

[83] R.J. Hill, Journal of Applied Crystallography 25 (1992) 589-610.

[84] D.L. Bish, J.E. Post (Eds.), Modern Powder Diffraction, Reviews in Mineralogy, 20th ed., Mineralological Society of America, Washington, 1989.

[85] L.B. McCusker, R.B. Von Dreele, D.E. Cox, D. Louër, P. Scardi, Journal of Applied Crystallography 32 (1999) 36-50.

[86] A.A. Coelho, J. Evans, I. Evans, A. Kern, S. Parsons, Powder Diffraction 26 (2011) 22.

[87] D.R. Gaskell, Introduction to the Thermodynamics of Materials, Taylor & Francis, 2003.

[88] K.-D. Liss, A. Stark, A. Bartels, H. Clemens, T. Buslaps, D. Phelan, L.A. Yeoh, Advanced Engineering Materials 10 (2008) 389-392.

[89] J.L. Murray, in: T.B. Massalski (Ed.), ASM, OH, 1986, pp. 1915-1917.

[90] T. Biggs, L.A. Cornish, M.J. Witcomb, M.B. Cortie, Journal of Alloys and Compounds 375 (2004) 120-127.

[91] J.L. Murray, Bulletin of Alloy Phase Diagrams 3 (1982) 329-335.

[92] F.J. Humphreys, M. Hatherly, Recrystallization and Related Annealing Phenomena, Pergamon Press Ltd., 2004.

[93] R. Doherty, D. Hughes, F. Humphreys, J. Jonas, D.J. Jensen, M. Kassner, W. King, T. McNelley, H.J. McQueen, A. Rollett, Materials Science and Engineering A 238 (1997) 219–274.

[94] F. Humphreys, Acta Materialia 45 (1997) 5031–5039.

[95] H.J. McQueen, Journal of Alloys and Compounds 378 (2004) 35-43.

[96] U. Lienert, S.F. Li, C.M. Hefferan, J. Lind, R.M. Suter, J.V. Bernier, N.R. Barton, M.C. Brandes, M.J. Mills, M.P. Miller, B. Jakobsen, W. Pantleon, JOM 63 (2011) 70-77.

[97] H.F. Poulsen, Three-dimensional X-ray Diffraction Microscopy: Mapping Polycrystals and Their Dynamics, Springer, Berlin, Heidelberg, 2004.

[98] B. Jakobsen, H. Poulsen, U. Lienert, J.D. Almer, S.D. Shastri, H.O. Sørensen, C. Gundlach, W. Pantleon, Science (New York, N.Y.) 312 (2006) 889-92.

[99] L. Margulies, G. Winther, H. Poulsen, Science 291 (2001) 2392.

[100] T. Schmoelzer, K.-D. Liss, C. Kirchlechner, S. Mayer, A. Stark, M. Peel, H. Clemens, submitted to Intermetallics.

[101] M. Schloffer, Charakterisierung der Mikrostrukturentwicklung von “hot-die” geschmiedetem TNM - Titanaluminid, Montanuniversität Leoben, 2010.

[102] M. Schloffer, T. Schmoelzer, S. Mayer, E. Schwaighofer, G. Hawranek, F.-P. Schimansky, F. Pyczak, H. Clemens, Praktische Metallographie/Practical Metallography 48 (2011) 594-604.

[103] A.J. Schwartz, M. Kumar, B.L. Adams, D.P. Field (Eds.), Electron Backscatter Diffraction in Materials Science, 2nd ed., Springer US, Boston, MA, 2009.

[104] M.J. Starink, International Materials Reviews 49 (2004) 191-226.

[105] A. Borrego, G. González-Doncel, Materials Science and Engineering A 252 (1998) 149-152.

[106] G.W.H. Höhne, W.F. Hemminger, H.-J. Flammersheim, Differrential Scanning Calorimetry, 2nd ed., Springer-Verlag, Berlin, 2003.

[107] B. Heine, Werkstoffprüfung, Carl Hanser Verlag, Munich, Germany, 2003.

[108] P. Staron, T. Fischer, T. Lippmann, A. Stark, S. Daneshpour, D. Schnubel, E. Uhlmann, R. Gerstenberger, B. Camin, W. Reimers, E. Eidenberger, H. Clemens, Norbert Huber, A. Schreyer, Advanced Engineering Materials 13 (2011) 658-663.

[109] Z. Huang, Intermetallics 13 (2005) 245-250.

[110] B. Larson, W. Yang, G.E. Ice, J.D. Budai, J.Z. Tischler, Nature 415 (2002) 887–890.

[111] R.I. Barabash, G.E. Ice, F.J. Walker, Journal of Applied Physics 93 (2003) 1457.

[112] C. Kirchlechner, D. Kiener, C. Motz, S. Labat, N. Vaxelaire, O. Perroud, J.-S. Micha, O. Ulrich, O. Thomas, G. Dehm, J. Keckes, Philosophical Magazine 91 (2011) 1256-1264.

[113] B. Liu, Y. Liu, W. Zhang, J.S. Huang, Intermetallics 19 (2011) 154-159.

[114] G. Wang, L. Xu, Y. Tian, Z. Zheng, Y. Cui, R. Yang, Materials Science and Engineering: A 528 (2011) 6754-6763.

[115] J. Si, F. Gao, P. Han, J. Zhang, Intermetallics 19 (2011) 169-174.

[116] M.-J. Fu, F. Gao, Zhang J., Journal of Iron and Steel Research 23 (2011) 50-54.

[117] D. Peter, G.B. Viswanathan, A. Dlouhy, G. Eggeler, Acta Materialia 58 (2010) 6431-6443.

9 Publication List

9.1 Journal Papers

T. Schmoelzer, A. Stark, E. Schwaighofer, T. Lippmann, S. Mayer, H. Clemens, "In-Situ Synchrotron Study of B19 Phase Formation in an Intermetallic γ-TiAl alloy" accepted at Advanced Engineering Materials DOI: 10.1002/adem.201200047.

T. Schmoelzer, K.-D. Liss, C. Kirchlechner, S. Mayer, A. Stark, M. Peel, H. Clemens, "An In-Situ High-Energy X-Ray Diffraction Study on the Hot-Deformation Behavior of a β-Phase Containing TiAl Alloy" submitted to Intermetallics.

T. Schmoelzer, K.-D. Liss, M. Rester, K. Yan, A. Stark, M. Reid, M. Peel, H. Clemens, "Dynamic Recovery and Recrystallization During Hot-Working in an Advanced TiAl Alloy", *Practical Metallography*, vol. 48, no. 12, pp. 632-641, Dec. 2011.

T. Schmoelzer, K.-D. Liss, P. Staron, S. Mayer, and H. Clemens, "The Contribution of High-Energy X-Rays and Neutrons to Characterization and Development of Intermetallic Titanium Aluminides," *Advanced Engineering Materials*, vol. 13, no. 8, pp. 685-699, Aug. 2011.

T. Schmoelzer, S. Mayer, C. Sailer, F. Haupt, V. Güther, P. Staron, K.-D. Liss, and H. Clemens, "In-Situ Diffraction Experiments for the Investigation of Phase Fractions and Ordering Temperatures in Ti-44 at% Al-(3-7) at% Mo Alloys," *Advanced Engineering Materials*, vol. 13, no. 4, pp. 306-311, Apr. 2011.

T. Schmoelzer, K.-D. Liss, G.A. Zickler, I.J. Watson, L.M. Droessler, W. Wallgram, T. Buslaps, A.J. Studer and H. Clemens, "Phase Fractions, Transition and Ordering Temperatures in TiAl–Nb–Mo Alloys: An In- and Ex-situ Study," *Intermetallics*, vol. 18, no. 8, pp. 1544-1552, Aug. 2010.

9.2 Co-authored Journal Papers

L. Cha, T. Schmoelzer, Z. Zhang, S. Mayer, H, Clemens, P. Staron, G. Dehm, "In-situ Study of γ-TiAl Lamellae Formation in Supersaturated α_2-Ti_3Al Grains", accepted at *Advanced Engineering Materials*, DOI: 10.1002/adem.201100272.

M. Schloffer, T. Schmoelzer, S. Mayer, E. Schwaighofer, G. Hawranek, F.-P. Schimansky, F. Pyczak, H. Clemens, "The Characterisation of a Powder Metallurgically Manufactured TNM™ Titanium Aluminide Alloy using Complementary Quantitative Methods", *Practical Metallography*, vol. 48, no. 11, pp. 594-604, 2011.

S. Kabra, K. Yan, S. Mayer, T. Schmoelzer, M. Reid, R. Dippenaar, H. Clemens, and K.-D. Liss, “Phase Transition and Ordering Behavior of Ternary Ti–Al–Mo Alloys Using In-Situ Neutron Diffraction”, *International Journal of Materials Research (formerly Zeitschrift fuer Metallkunde)*, vol. 102, no. 6, pp. 697-702, Jun. 2011.

M. Rester, F.-D. Fischer, C. Kirchlechner, T. Schmoelzer, H. Clemens, and G. Dehm, “Deformation Mechanisms in Micron-sized PST TiAl Compression Samples: Experiment and Model”, *Acta Materialia*, vol. 59, no. 9, pp. 3410-3421, May. 2011.

E. Eidenberger, M. Schober, T. Schmoelzer, E. Stergar, P. Staron, H. Leitner, and H. Clemens, “Analysis of the Multistage Phase Separation Reaction in Fe–25 at% Co–9 at% Mo”, *Physica Status Solidi (A)*, vol. 207, no. 10, pp. 2238-2246, Oct. 2010.

K.-D. Liss, T. Schmoelzer, K. Yan, M. Reid, R. Dippenaar, and H. Clemens, “In-situ Study of Dynamic Recrystallization and Hot-Deformation Behavior of a Multiphase Titanium Aluminide Alloy”, *Journal of Applied Physics*, vol. 106, no. 11, p. 113526, 2009.

W. Wallgram, T. Schmoelzer, L. Cha, G. Das, V. Güther, and H. Clemens, “Technology and Mechanical Properties of Advanced γ-TiAl Based Alloys”, *International Journal of Materials Research (formerly Zeitschrift fuer Metallkunde)*, vol. 100, no. 8, pp. 1021-1030, 2009.

I.J. Watson, K.-D. Liss, H. Clemens, W. Wallgram, T. Schmoelzer, T.C. Hansen, and M. Reid, “In-situ Characterization of a Nb and Mo Containing γ-TiAl Based Alloy Using Neutron Diffraction and High-Temperature Microscopy”, *Advanced Engineering Materials*, vol. 11, no. 11, pp. 932-937, Nov. 2009.

9.3 Proceedings

T. Schmoelzer, K.-D. Liss, S. Mayer, K. Yan, M. Reid, R. Dippenaar, M. Peel, and H. Clemens, “Hot Deformation of Cast and Extruded TiAl : An In-situ Diffraction Study”, *Materials Science Forum*, vol. 709, pp. 1725-1730, 2012.

T. Schmoelzer, S. Mayer, F. Haupt, G.A. Zickler, C. Sailer, L. Lottermoser, V. Güther, K.-D. Liss, and H. Clemens, “Phase Transition and Ordering Temperatures of TiAl-Mo Alloys Investigated by In-Situ Diffraction Experiments”, *Materials Science Forum*, vol. 654-656, pp. 456-459, Jun. 2010.

9.4 Co-authored Proceedings

P. Simas, T. Schmoelzer, M. L. Nó, H. Clemens, and J. San Juan, “Mechanical Spectroscopy in Advanced TiAl-Nb-Mo Alloys at High Temperature”, in *Mater. Res. Soc. Symp. Proc. Vol. 1295*, 2011, pp. 139-144.

S. Mayer, C. Sailer, H. Nakashima, T. Schmoelzer, T. Lippmann, P. Staron, K.-D. Liss, H. Clemens, M. Takeyama, “Phase Equilibria and Phase Transformations in Molybdenum-containing TiAl Alloys”, in *Mater. Res. Soc. Symp. Proc. Vol. 1295*, 2011, pp. 113-118.

H. Clemens, B. Boeck, W. Wallgram, T. Schmoelzer, L.M. Droessler, G.A. Zickler, H. Leitner, and A. Otto, “Experimental Studies and Thermodynamic Simulations of Phase Transformations in Ti-(41-45)Al-4Nb-1Mo-0.1B Alloys”, in *Mater. Res. Soc. Symp. Proc. Vol. 1128*, 2008, pp. 115-120.

L. M. Droessler, T. Schmoelzer, W. Wallgram, L. Cha, G. Das, and H. Clemens, “Microstructure and Tensile Ductility of a Ti-43Al-4Nb-1Mo-0.1B Alloy”, in *Mater. Res. Soc. Symp. Proc. Vol. 1128*, 2008, pp. 121-126.

ADVANCED ENGINEERING MATERIALS

Appendix A:
The Contribution of High-Energy X-Rays and Neutrons to Characterization and Development of Intermetallic Titanium Aluminides

T. Schmoelzer, K.-D. Liss, P. Staron, S. Mayer und H. Clemens

Advanced Engineering Materials **13** (8), 2011, pp. 685-689

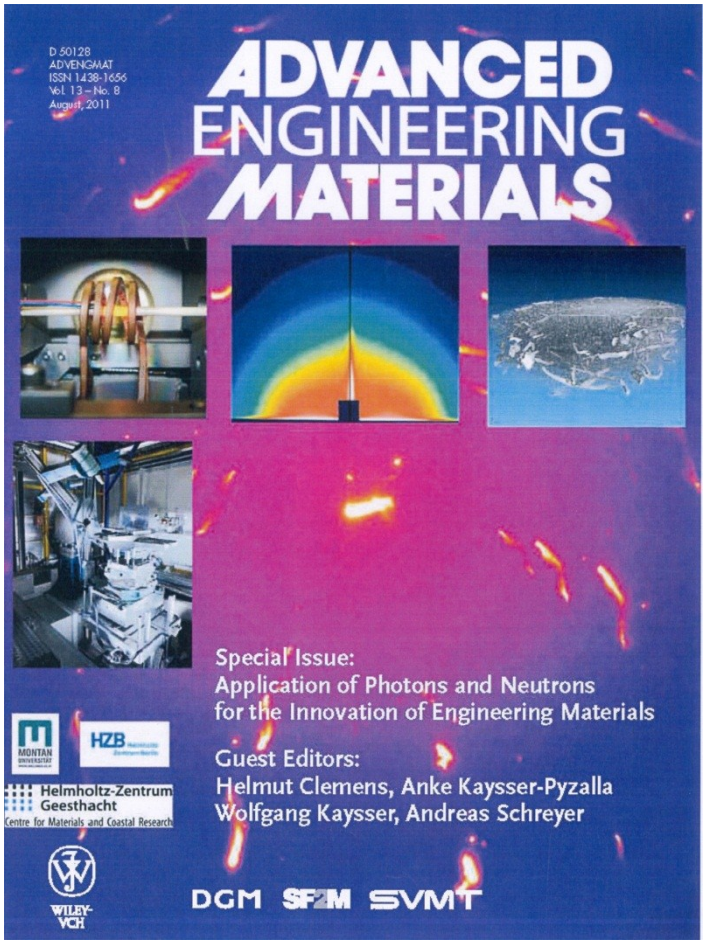

The Contribution of High-Energy X-Rays and Neutrons to Characterization and Development of Intermetallic Titanium Aluminides**

By *T. Schmoelzer**, *K.-D. Liss*, *P. Staron*, *S. Mayer*, and *H. Clemens*

[*] *T. Schmoelzer, Dr. S. Mayer, Prof. Dr. H. Clemens*
Department of Physical Metallurgy and Materials Testing,
Montanuniversität Leoben, 8700 Leoben, Austria.
E-mail: thomas.schmoelzer@unileoben.ac.at
Dr. K.-D. Liss
Australian Nuclear Science and Technology Organisation,
Lucas Heights, NSW 2232, Australia.
Dr. P. Staron
Institute of Materials Research,
Helmholtz-Zentrum Geesthacht, 21502 Geesthacht, Germany.

[**] *The support of the DESY and ESRF managements and user offices is gratefully acknowledged. We appreciate the commitment of the HZG and ESRF beamline staff which contributed greatly to the success of the experiments performed. Research activities performed at DESY have received funding from the European Community's Seventh Framework Programme (FP7/2007-2013) under grant agreement n°226716.*

Intermetallic γ-TiAl based alloys are a novel class of lightweight structural materials that exhibit excellent high-temperature strength while having low density. These properties make them ideal candidates for replacing dense Ni base alloys currently used in the temperature range from 550°C to 750°C. Therefore, extensive research activities were conducted during the last 20 years to make this innovative class of materials fit for service. In this task, diffraction methods have been an important tool for promoting the development of TiAl alloys. The ability to perform experiments in-situ and to determine phase fractions even in cases where two phases are present in ultrafine lamellar structures are only two examples for applications in which diffraction methods are indispensable. In this work, a review is given concerning the use of diffraction methods in the development of TiAl alloys. Different methods are introduced and highlighted by examples. This review lists the advantages of diffraction experiments and critically discusses the limits of the individual methods.

1. Introduction

Ever increasing economic and environmental pressure promotes the development of more fuel-efficient combustion engines. One way of decreasing the fuel consumption of vehicles and airplanes is to reduce component weights. In addition to careful design, new structural materials are necessary to achieve substantial weight reductions. Intermetallic γ-TiAl based alloys have low densities while exhibiting excellent high-temperature strength.[1-8] Therefore, this material class is expected to replace conventional high-temperature materials with high densities such as Ni base super-alloys in applications where temperatures range up to 750°C. Possible applications are turbocharger wheels for reciprocating combustion engines, valves in sports and racing cars and low pressure turbine blades in jet-engines.[1][3-5][9-16]

During the last twenty years, considerable effort has been made to develop γ-TiAl based alloys that are suited for service in these demanding areas while being economically competitive at the same time. To achieve this goal, different processing routes and alloy compositions have been intensively studied.[9][17][18] The multitude of phase transformations that occur in the Ti-Al binary system along with the pronounced dependency of transformation temperatures on chemical composition complicates the development of alloys that can be produced in a robust industrial production process.[19] Additionally, TiAl alloys frequently show rather coarse grained microstructures after casting. Efforts have been undertaken to develop heat-treatments that allow adjusting a microstructure with desired mechanical properties in cast TiAl parts.[20] An additional approach was chosen for wrought alloys where cast ingots are forged and heat-treated under conditions that result in the desired properties.[21][17] In both cases a profound knowledge of the phase diagram and the kinetics of the occurring phase transformations are prerequisites for the design of a reliable production route.

Conventional ex-situ characterization methods suffer from certain limitations in the case of the TiAl system. That the ordering reactions α (A3) → α_2 ($D0_{19}$) and β (A2) → β_o (B2) are too fast to preserve the disordered state by rapid quenching is only one example.[22] Complications might arise by the possible change in phase fractions if the phases present at high-temperatures are determined by microscopical methods on heat-treated and quenched specimens. Additional problems may occur due to the fine γ-phase ($L1_0$) lamellae that precipitate from supersaturated α/α_2 grains. With their width being as small as 10 nm, light-optical microscopy (LOM) or scanning electron microscopy (SEM) have insufficient resolution for determining phase fractions within lamellar regions.[23] Transmission electron microscopy (TEM) on the other hand suffers from its restriction to small sample volumes.

As a tool for materials characterization, conventional diffraction methods have been used since the early beginnings of research activities on TiAl alloys.[24-28] Phase fractions can be determined independently of grain sizes and ordering phenomena are observed through

the occurrence of superstructure reflections.[29][30] Thus, in many cases, these methods offer considerable advantages compared to microscopical methods. Due to the widespread availability, most diffraction experiments performed on TiAl alloys have been conducted by means of laboratory X-ray sources. In-situ studies were performed with a high-temperature diffractometer with all the ensuing limitations discussed in Section 3.1. An alternative that offers higher penetration depth, as compared to laboratory sources, is the use of synchrotron radiation. The high brilliance of the beam in combination with the availability of powerful area detectors allow highly time resolved in-situ studies.[31][32] Neutrons are also used for diffraction experiments on TiAl and offer even higher penetration depth than synchrotron radiation.[31] A more detailed introduction to the different types of radiation and their properties is given in Section 2.

In this review, methods used for characterizing TiAl alloys are illustrated by several examples. Advantages and limitations of different methods and experimental setups are discussed and possible pitfalls highlighted.

2. High Energy X-Rays and Neutrons

Despite their different nature, high energy X-rays and neutrons are both suited for performing diffraction as well as scattering experiments in materials science.[33] While neutrons are particle waves, X-rays are electromagnetic waves which causes the modes of interaction with the investigated material to differ correspondingly: For the case of non-magnetic materials, neutrons interact with the nucleus of the atoms, while X-rays are scattered by their electrons. This leads to different contrasts and atomic form factors. While the scattering length in case of X-rays is the classical electron radius r_e times the number of electrons, which corresponds in general to the atomic number of the investigated element, no clear dependency between atomic isotope and scattering length exists for neutrons.[34] Further, in the case of X-rays, the scattering centers in the electron cloud are extended, as compared to the wavelength, in contrast to point centers for neutrons. This causes the form factors to decrease with increasing momentum transfer **q** in the case of X-rays, while they remain constant for neutrons. Apart from a few highly absorbing isotopes, neutrons have generally a larger attenuation length than X-rays, which can range from centimeters to meters and micrometers to centimeters, respectively.[31]

Another important difference is imposed by the corresponding radiation sources. X-rays can be generated by standard laboratory sources that are easy to handle and comparatively cheap. If higher brilliance is required, synchrotron sources are used although at greatly increased costs and limited availability.[35] Neutrons, on the other hand, are only available at large-scale facilities such as research reactors and spallation sources.[36] Compared to synchrotrons, neutron sources are of low brilliance which entails correspondingly larger beam cross sections and longer acquisition times for obtaining

diffraction patterns. Despite these limitations, neutron diffraction experiments can yield important information on the behavior of materials in a variety of conditions.

The scattering behavior of atoms is characterized by b_c for neutrons and $r_e \cdot f(q)$ for X-rays. Here, b_c is the bound coherent neutron scattering length, while r_e is the classical electron radius and f(q) is the so-called atomic X-ray form factor. The spatial arrangement of the atoms is accounted for by the phase factor which is dependent on the position of an individual atom within the unit cell. Summing up the atomic scattering lengths weighted by the respective phase factors for all atoms within the unit cell yields the structure factor F_{HKL} which finally determines the intensity of the diffraction peaks.[37][38]

If the elements are distributed randomly in the crystal lattice, a virtual atom with a mean scattering length is calculated. Intensities of single reflections are derived from the structure factors which in turn are calculated by summing up the mean atomic scattering lengths of the atoms in one unit cell and weighting them by an individual phase factor that depends on the position of the respective atom in the unit cell. For the main reflections of a phase, the phase factors are close to one and the scattering lengths of the individual atoms add up directly. Therefore, high intensities are usually observed for these reflections. Superstructure reflections do not occur in disordered crystals because they exhibit phase factors that are equal but of opposite sign, which results in a structure factor that is zero and causes the corresponding reflections to vanish.

In the case of ordered structures, no average scattering length is calculated. The scattering lengths from the individual atomic sites are multiplied by the phase factors for the corresponding reflection. Summing up these values gives the structure factor which determines the intensity of the reflection. If the different elemental species exhibit different scattering lengths, the structure factor for superstructure reflections is no longer zero. Consequently, the intensity of the reflections then attains a finite value which indicates that some degree of order exists in the investigated phase.

In the case of γ-TiAl, which exhibits $L1_0$ structure, this behavior has a peculiar consequence: Since for neutrons the scattering lengths of Ti (-3.370 fm) and Al (3.449 fm)[39] are very similar but of opposite sign, the structure factor for the main reflections is close to zero and the observed intensities are therefore rather small. On the contrary, if this calculation is performed for superstructure reflections, large structure factors and therefore high intensities are obtained.

When X-rays are used to probe the material, superstructure reflections have rather low intensities while the main reflections exhibit high intensities. Since these statements are valid for α_2, β_o, and γ phase, neutron and X-ray diffraction are in fact complementary techniques if applied to TiAl alloys.[29][30] For neutron and high-energy X-ray diffraction (HEXRD) experiments, the diffraction pattern is recorded in transmission geometry which is

easily possible due to their high penetration depth. A typical example for a HEXRD experimental setup is shown in **Figure 1**.

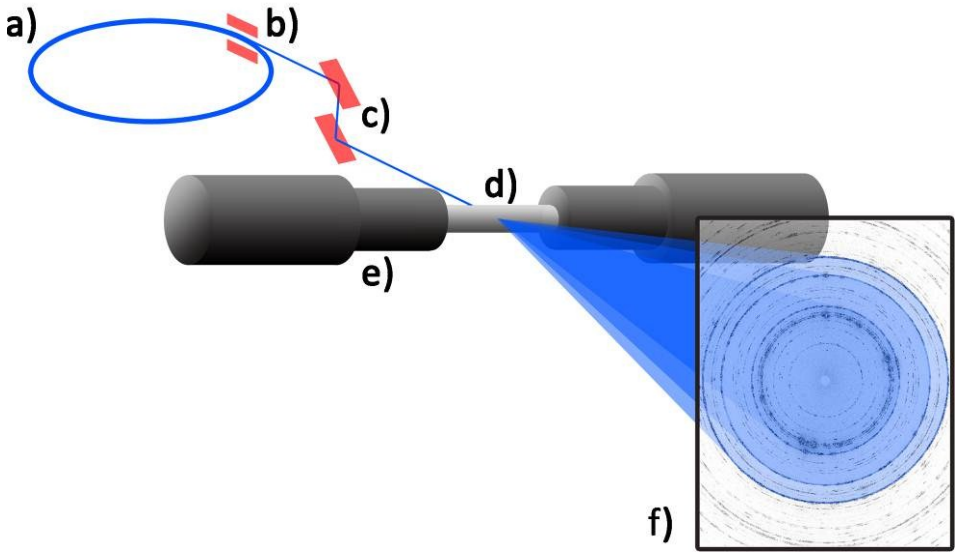

Figure 1: A typical experimental setup for a HEXRD experiment in transmission geometry is shown. Electrons or positrons in the storage ring (a) are deflected by an insertion device (b) which causes them to emit a white X-ray beam. After the monochromator (c) a beam with a narrow energy bandwidth penetrates the sample (d). Different environments can be adjusted by additional devices such as furnaces or load-frames (e). The diffracted intensity on the Debye-Scherrer Rings is then recorded by a flat-panel detector (f).

A white X-ray beam is produced by the deflection of charged particles (usually electrons or positrons) in a storage ring. In order to deflect the particles, an insertion device such as a bending magnet, wiggler, or undulator is used.[35] A narrow energy range is selected from the white beam by the monochromator.[31] After that, the monochromatic beam is collimated and interacts with the specimen. The diffracted intensity is recorded by a suitable detector. Common recording devices for high energy X-rays are fluorescent screens coupled to a charge-coupled Device (CCD) detectors, amorphous silicon pixel detectors or online image-plates. Further information on detectors can be found in.[31][32] For in-situ diffraction experiments, different environments can be adjusted at the sample position. A variety of furnaces and load-frames is available for heating the specimen in a controlled atmosphere or performing in-situ deformation experiments.

3. In-situ Investigation of Phase Evolution

3.1 General Aspects

A common feature of structural materials, including TiAl alloys, is the dependency of their properties on phase composition and the arrangement of the constituting phases. It is therefore decisive for the materials behavior under service conditions as well as during processing which phases are present to what amount.

There is a plethora of methods by which a quantitative evaluation of phase-fractions is possible. Light-optical microscopy on etched specimens for instance is usually readily available and a very cost-effective method for determining phase-fractions. In the case of advanced TiAl alloys, however, up to three different phases have to be distinguished. It is therefore difficult to find etchants that provide reproducible results and allow determining and quantifying the present phases unambiguously. Additionally, γ and α_2-phase frequently occur in the form of lamellar colonies. The thickness of the γ-lamellae depends on the thermal history of the specimen and can be as small as 10 nm.[23] Therefore, the evaluation of the overall phase fractions in lamellar microstructures by means of LOM is not possible. Even in the case of SEM investigations those two phases can usually not be properly distinguished. For the investigation of phase fractions, SEM images are recorded in back-scattered electron (BSE) mode. Due to the large volume from which back-scattered electrons emerge and the low contrast between α and γ-phase, the determination of phase fractions with SEM is not feasible if lamellar colonies are present. TEM is a method that would allow determining phase fractions in lamellar grains, although at the expense of time-consuming sample preparation and the restriction to small sample volumes.

By diffraction methods, the phase fractions can be determined with high accuracy even in the case that lamellar colonies are present in the material. Additionally, it is possible to adjust special sample environments that allow conducting these experiments at elevated temperatures or during deformation. Especially at synchrotrons, highly time-resolved in-situ experiments can be performed due to the high brilliance of the source.[32]

Due to the numerous advantages that the determination of phase fractions with diffraction methods offers, compared to competing techniques in the case of TiAl alloys, laboratory X-ray sources have been used since the beginning of research activities on TiAl alloys.[37][24][40][41] One way to investigate phase fractions present at elevated temperatures is to perform conventional XRD on heat-treated and quenched specimens. A drawback of this method is that changes in the microstructure might occur during cooling that could potentially lead to erroneous results.

To circumvent this problem, in-situ experiments have been performed by means of high-temperature X-ray diffractometry.[37][24][40] In this case a different complication arises: If exposed to temperatures >1000°C for a prolonged time span, the surface-near regions of

TiAl samples deplete in Al and a so called α-case forms, even in controlled atmospheres or vacuum. This surface layer can be (depending on temperature and holding time) several 100 µm thick and consists almost exclusively of α/α_2-phase.[30] Due to the low penetration depth of laboratory X-ray sources (e.g. 50% absorbed by 80 µm thick Al-plate for Cu$K\alpha$), high-temperature XRD experiments are limited to temperatures where no α-case formation is observed. At dedicated high-energy beamlines high penetration depths can be attained (e.g. 50% absorbed by 12.8 mm Al at 100 keV) so that α-case formation affects the experiments less severely.[32]

3.2 Phase evolution in β/γ-alloys

It has been shown that the presence of disordered β-phase at elevated temperatures improves the hot-workability of TiAl alloys significantly.[17][19][42] Although room temperature ductility and creep resistance at service temperature are negatively influenced by high β_o volume fractions [43], the concept of so-called β/γ-alloys has been conceived to facilitate the cost-effective production of TiAl parts for applications in which lower temperature and mechanical loads are imposed. In this type of alloys, the β/β_o-phase is stabilized by elements such as Mo and Nb.[44][45][20][46] One of the challenges to be faced is that the commercially available TiAl thermodynamic database [47] is insufficient for describing binary phase diagrams with high contents of β/β_o stabilizing elements properly.[21][48] Therefore, the predictions of the thermodynamic calculations are inaccurate and the dependence of the phase fractions and transition temperatures on the amount of β/β_o stabilizing elements is not well known.

In **Figure 2** a thermodynamically calculated Ti-Al-Mo phase diagram and one derived from data published in the open literature [49-51] are presented. Both diagrams are shown for an Al content of 44 at% and Mo contents in the range from 0 to 10 at%. It is obvious that significant differences between the two phase diagrams exist.

For validating the accuracy of calculated and literature data, alloys with nominal compositions of Ti-44 Al-3 Mo-0.1 B and Ti-44 Al-7 Mo-0.1 B were produced by GfE Materials and Metals GmbH (Nuremberg, Germany) and investigated by means of in-situ HEXRD at the HARWI II beamline of GKSS Research Centre at DESY in Hamburg (Germany).[52] Note that all compositions are stated in atomic percent unless indicated otherwise. In these experiments, cast and hot-isostatically pressed (HIP) specimens were heated rapidly to 1000°C, held for 2 min and then continuously heated to 1350°C at a rate of 0.033 K/s. Integration of the patterns acquired with a mar555 flat panel detector (MAR Research, Nordersted, Germany) was performed by the software fit2D.[53] Phase fractions present were evaluated by means of the intensity ratio method where the weighting factors were derived from the results of Rietveld analysis performed at different temperatures. Rietveld fitting was carried out with the commercial software package TOPAS (Brucker AXS,

Madison, USA). The SEM images were obtained from samples heated to the desired temperature, annealed for 1 h and subsequently water quenched.

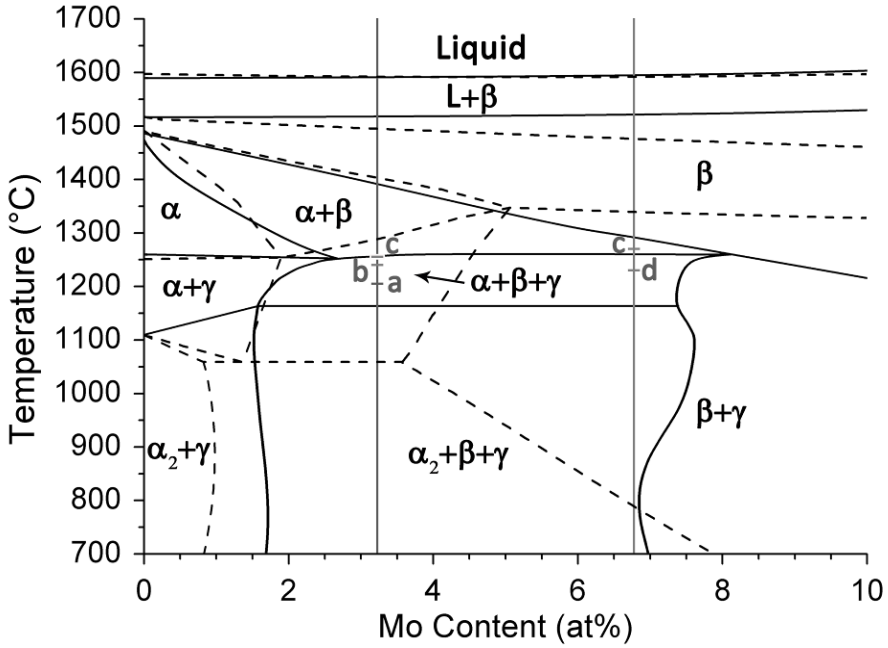

Figure 2: Two superimposed Ti-44 Al-(0-10) Mo phase diagrams derived from literature data (continuous) and obtained by thermodynamic simulations (dashed) are shown. Substantial differences exist in terms of transformation temperatures and in the shape and position of the occurring phase fields. The compositions of the two investigated alloys are given by vertical lines and their experimentally determined transformation temperatures by short horizontal dashes. The eutectoid temperature is indicated by the letter a, whereas b marks the disordering temperature of βo and at c the γ-phase dissolves. At the temperature indicated by d the onset of α-phase formation was observed.

The results of the phase fraction analyses are depicted in **Figure 3**. All microstructural images were acquired in BSE mode, in which the β/β_o phase appears brightest, the γ-phase is dark and the α/α_2 phase presents with an intermediate contrast. It is obvious that with increasing Mo content, the amount of α/α_2-phase diminishes. Consequently, the fraction of β/β_o-phase is increasing with increasing Mo content. Concerning the dissolution temperature of γ, the so-called α-transus temperature, a slight increase is observed with increasing Mo content.

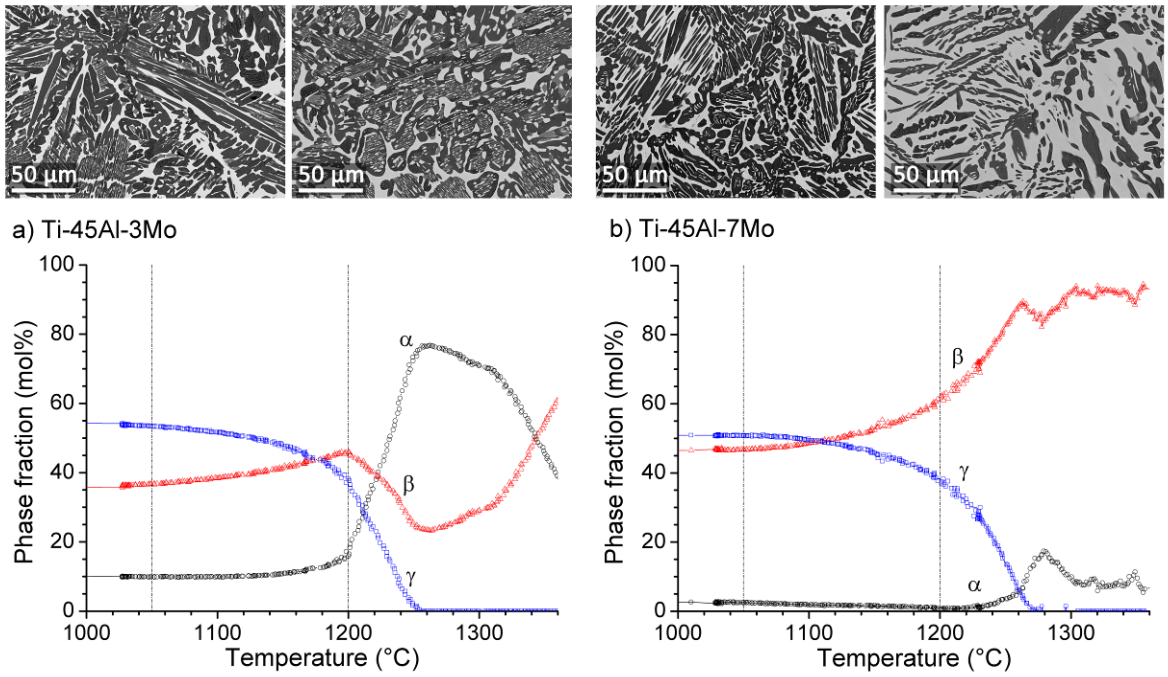

Figure 3: The course of phase fractions is shown for two alloys with a nominal composition of a)Ti-44 Al-3 Mo-0.1 B and b)Ti-44 Al-7 Mo-0.1 B. At the temperatures indicated by vertical lines, additional micrographs are provided which were obtained in the SEM in BSE mode.

A comparison of the results in Figure 3 with the phase diagrams derived from literature and thermodynamic calculations shows that a significant deviation between experimental results and the phase diagrams exists. While the calculated phase diagram and the course of phase fractions in Figure 3 show only a faint resemblance, both in terms of transition temperatures and phases present, the phase diagram derived from literature fits the experimental data better. Due to deviations of the actual from the nominal chemical composition of the specimens, slight differences in phase fractions or transformation temperatures could be explained. However, if the deviations are as large as in the case of the experimental results and the calculated phase diagram, it must be concluded that the calculation is erroneous.

In a next step, the database used for the calculation has to be modified on the basis of the experiments conducted in order to be able to correctly predict the phase diagram. Thus, the HEXRD experiment not only allowed to verify the accuracy of the prediction but also provided data that allow improvement of the thermodynamical model.

3.3 Formation of lamellar microstructure

In addition to the course of phase fractions over temperature, the processes during the formation or dissolution of phases are frequently of particular interest. In a recent study of Shuleshova et al. [54], the solidification behavior of Ti-Al-Nb ternary alloys was investigated by means of HEXRD which allowed a reassessment of the thermodynamic database used for phase calculations. Senkov et al. [55] investigated the crystallization behavior of an amorphous TiAl film produced by physical vapor deposition and was able to show that this process occurred in a two-step fashion. Studies concerning the formation and coarsening of Perovskite-type precipitates in carbon containing TiAl alloys were conducted by means of small angle neutron scattering.[56]

In TiAl alloys, the γ-phase dissolves at the α-transus temperature. If the specimen is cooled slowly afterwards, the formation of γ-lamellae occurs within the supersaturated, disordered α-grains.[2][57][58] If the alloy is cooled from the (α+β) two-phase region at a sufficiently high rate, the two-phase microstructure can be preserved down to room temperature and no γ-phase is formed. The only phase transformation occurring is the ordering of the supersaturated α-phase. By a subsequent heat-treatment, γ-lamellae are formed in the supersaturated α_2-grains.[59][19] The formation of fine γ-lamellae strongly increases the performance of the material in terms of strength, plastic fracture strain, fracture toughness, and creep resistance at service temperature.[60][23][25][58] If the γ-lamellae are formed upon cooling, the cooling rate is the decisive parameter for the interlamellar spacing.[57][61] In fast cooled material, in which the formation of γ-phase was suppressed, γ-lamellae can form during an ensuing heat-treatment step.[62] The lamellar spacing then depends on the heating rate and maximum temperature reached if continuously heated or solely on the temperature if the heat-treatment is performed isothermally.[63][23]

To determine the onset of γ-lamellae precipitation during continuous heating in a Ti-45 Al-7.5 Nb alloy, experiments were conducted at the ESRF in Grenoble, France.[62] Diffraction data acquired with a two-dimensional detector allowed investigating the diffuse and inter-Bragg-peak scattering. Streaking of the reflections in reciprocal space has been observed, which is correlated to the precipitation and formation of ultrafine γ-lamellae within globular α_2-grains. The obtained results were verified by repeating the experiment in a high temperature laser scanning confocal microscope.[62]

In an ensuing experiment, a two-step heat-treatment was conducted on a Ti-43.5 Al-4 Nb-1 Mo-0.1 B specimen to quantify the development of phase fractions. At first, the sample was heated to 1230°C which is slightly below the dissolution temperature of the γ phase and held for 300 s at this temperature to reduce the amount of γ-phase. Subsequently, the specimen was quenched to room temperature in order to produce supersaturated α_2 grains. During the second heat treatment step a continuous heating

ramp with a constant heating rate of 2 K/s was adjusted and γ lamellae precipitate in the supersaturated α_2 grains.[19][59]

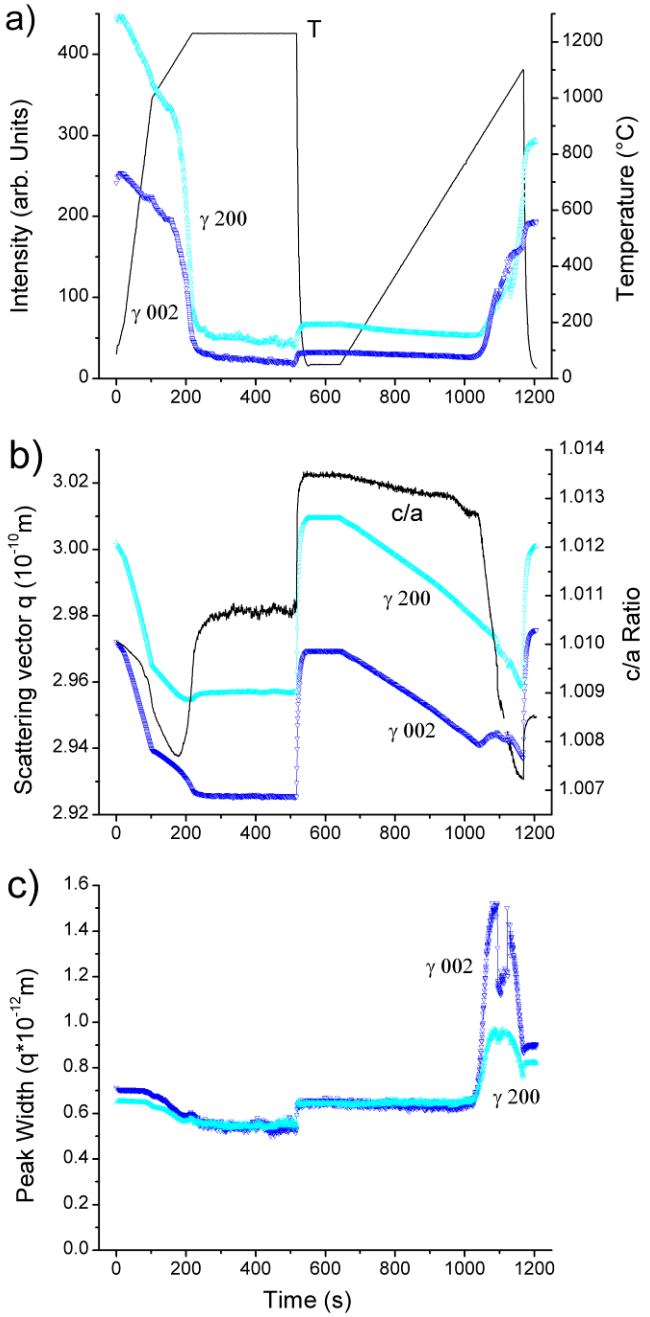

Figure 4: Parameters of the γ 200 and γ 002 peaks as well as the temperature are plotted versus time for a Ti-43.5 Al-4 Nb-1 Mo-0.1 B alloy. In (a) the peak intensity and the temperature are shown. (b) indicates the peak position and the tetragonality of the γ unit cell. Diagram (c) represents the peak width. After dissolution of most of the γ-phase at 1230°C, the specimen is quenched. Upon reheating with a rate of 2 K/s, the γ-phase fraction starts to increase. Simultaneously, the tetragonality of the unit-cell is changing and the peak widths are increasing.

Figure 4 a superimposes the γ 200 and γ 002 peak intensities with the temperature program of the conducted heat treatment as a function of time. Upon heating, a drop in peak intensity is observed which indicates that the volume fraction of γ-phase decreases. At the same time, the peak positions plotted in Figure 4 b shift towards lower q-values due to the thermal expansion of the material. Furthermore, the tetragonality c/a of the γ unit cell initially decreases but as the γ-phase fraction diminishes, this trend is reversed and the c/a ratio increases rapidly. While the temperature is kept constant at 1230°C, the γ-phase fraction decreases slightly while peak positions and c/a ratio remain approximately constant. The peak width does not change significantly during the holding time, while it decreases slightly upon heating to 1230°C. As the sample is quenched, the peak positions move towards larger scattering vectors and the c/a ratio rises further. Small increases in peak intensity and width are also observed on quenching which indicates a small increase in the γ-phase volume fraction.

After quenching, the specimen was heated at a rate of 2 Ks^{-1} as indicated in Figure 4 a. Except from the thermal expansion of the sample, no major changes are observed until 1000 s (765°C) are reached. At this time, the c/a ratio starts to decrease. At t>1050 s (867°C) dramatic changes in all parameters become visible. The γ-phase fraction starts to increase rapidly, while the c/a ratio is diminishing. Additionally, the peak width of both γ reflections (γ 200 and γ 002) increases. After reaching a maximum at 1090 s (947°C), the peak width decreases while the intensity of the γ-peaks continues to rise. The c/a ratio also keeps following its initial trend and is getting smaller until, at 1170 s the specimen is cooled.

It is obvious from Figure 4 that only little γ-phase forms during quenching. As the sample is reheated the γ-phase fraction increases which indicates the precipitation of γ-lamellae within the supersaturated α_2 grains. Although more detailed investigations would be necessary to make any definitive statements, it is tempting to speculate that the changes in c/a ratio and in peak width are caused by coherency strains as well as by the chemical composition being far from thermodynamic equilibrium. As the precipitation process progresses, which is indicated by an increase in intensity, the γ-lamellae grow in thickness, causing the coherency strains to diminish. This effect could explain the decrease in width of the γ peaks.

Peak height, width, and intensity were determined by fitting two Gaussians to the double-peak of γ-002/200. As the peak width increases and the c/a ratio decreases, the separation of the two peaks becomes smaller which causes the fitting algorithm to produce incoherent results. This explains the discontinuities in the data plots of Figure 4 c. Despite the poor fitting in Figure 4 c, there is no doubt that the reflections broaden significantly.

The precipitation of γ lamellae during reheating of the specimen was also observed in TEM investigations.[19][59] The corresponding images are shown in **Figure 5**.

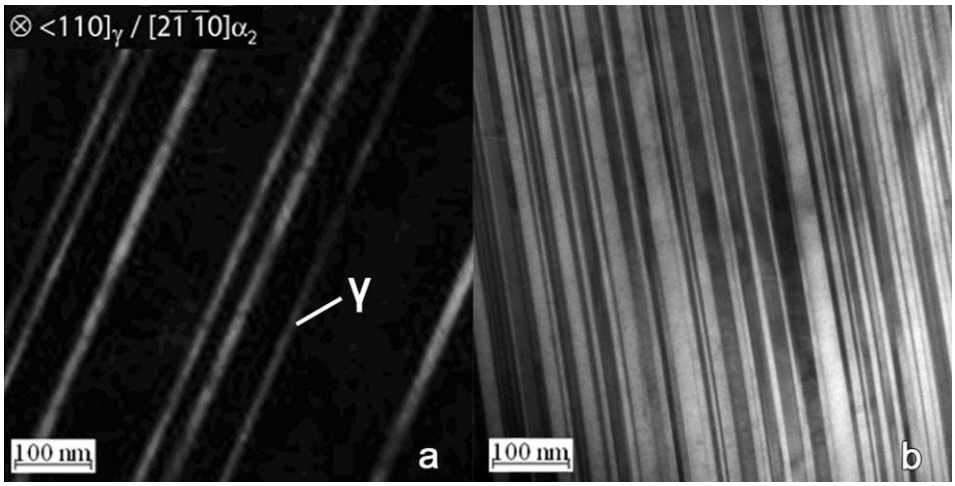

Figure 5: TEM images of lamellar colonies in a Ti-43.5 Al-4 Nb-1 Mo-0.1 B alloy. An α_2-grain is shown after quenching from 1230°C (a) in which only few γ-lamellae have formed. Lamellar colonies exist after annealing at 850°C as shown in (b). It is obvious, that the number and volume of γ-lamellae has increased upon annealing.[19]

After annealing at 1230°C and subsequent water quenching, only few γ lamellae are visible in the TEM. Within the lamellar colonies, the orientation of γ and α_2-lamellae is described by the so-called Blackburn orientation relationship where γ(111) ‖ α_2(0001) and γ[110] ‖ α_2[11-20].[64] In contrast to this, a large number of γ lamellae can be observed when the material is isothermally annealed at 850°C for 6 h subsequently to quenching. It is therefore concluded that after annealing at 1230°C and water quenching the α_2-grains are supersaturated and γ-lamellae precipitate during an ensuing heat-treatment.

The in-situ HEXRD experiments complement the TEM investigations because they allow determining the temperature at which the precipitation process starts. Additionally, the data show that the c/a ratio changes with temperature and during the formation of γ-lamellae.

As shown in this section, in-situ HEXRD experiments yield a multitude of data on phase transformations. Not only phase fractions are extracted, but also the evolution of lattice parameters and the width of the reflections are simultaneously obtained. The lattice parameter may be of interest since the formation of a new phase from a supersaturated parent phase usually entails a change in the chemical composition and, therefore, according to Vegards law, a change in the lattice parameter of the corresponding phases.[65-67] From the measured peak widths, information on the defect density and the internal strains can be derived.[68]

4. Atomic Order and Disorder in TiAl Alloys

Ordering phenomena are important in TiAl alloys, because the mechanical behavior of the occurring phases changes upon ordering. The disordered β-phase, for instance, improves the hot-workability of TiAl alloys at elevated temperatures [69-71] whereas the ordered β_o phase affects the room-temperature ductility negatively.[43] An additional motivation for determining ordering temperatures is that the accuracy of thermodynamic calculations can be validated by comparing ordering temperatures obtained from experiments with calculated ones.

Ex-situ studies have been performed with laboratory X-ray sources in order to study the site occupancy in different phases.[72][73][26] Complementary investigations concerning the ordering behavior were conducted by means of TEM.[22] HEXRD was used to investigate the site occupancy in the α-phase by means of Rietveld analysis and thereby derive the disordering temperature of α_2 in a Ti-45 Al-7.5 Nb-0.5 C alloy.[74] Due to the fast kinetics of the ordering reactions, it is not possible to preserve the disordered states of α and β-phase down to room-temperature even if the specimens are water-quenched.[22][75] It is therefore inevitable to investigate the ordering behavior at those temperatures where the ordering reactions occur.

As described in Section 2, neutron diffraction is particularly well suited for investigating the ordering behavior of TiAl. Experiments for determining the ordering/disordering temperatures of α/α_2 and β/β_o-phase in a Ti-43.9 Al-4 Nb-1 Mo-0.1B alloy were performed with the structure powder diffractometer SPODI [76][77] at the FRM II neutron source in Garching, Germany. Since the acquisition time for one diffraction pattern was set to three hours, the specimen was heated in a stepwise fashion where the temperature remained constant during pattern acquisition. In **Figure 6** the patterns acquired at four different temperatures are shown exemplarily.

While at 1000°C and 1100°C superstructure reflections of all three phases are visible, the α_2 reflections have vanished at 1200°C. Between 1200°C and 1250°C, the β_o reflections also attain zero intensity. The presence of α and β phase above 1300°C has been proven by earlier work [21] and the vanishing of the superstructure reflections indicates the loss of order in the respective phase due to the average scattering length of the disordered material being close to zero.

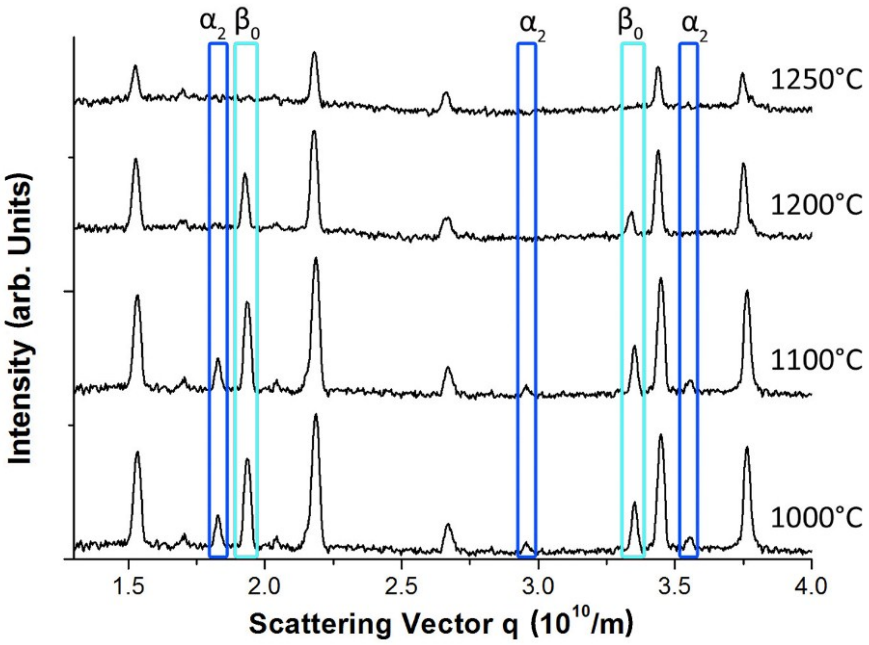

Figure 6: Neutron diffraction patterns of a Ti-43.5 Al-4 Nb-1 Mo-0.1 B alloy obtained with the powder diffraction spectrometer SPODI at the FRM II research reactor (Garching, Germany). Peaks of the α_2 and β_o-phases are indicated by rectangles and labeled at the top. The temperatures at which the patterns were recorded are given on the right hand side of the image. Between 1100°C and 1200°C, the α_2 reflections vanish, whereas the β_o phase disorders between 1200°C and 1250°C.

During the experiment at SPODI, only few data-points were generated due to the long acquisition times for the individual patterns. To be able to determine the order-to-disorder transition temperatures more accurately, neutron diffraction experiments were performed at the WOMBAT facility at the OPAL reactor of the Australian Nuclear Science and Technology Organization (ANSTO) in Lucas Heights, Australia.[78] The facility is optimized for high intensity rather than resolution and hosts a true two-dimensional, position sensitive detector covering 120° in-plane and 15° out-of-plane. The area is binned into 968×128 pixels, each with intrinsic time response (microseconds), which makes the acquisition fast and only intensity limited. With the two-dimensional detector installed, a single pattern with sufficient counting statistics was obtained within an exposure time of 18.2 s.[29] At a heating, respectively cooling rate of 0.166 Ks^{-1}, this frame rate is sufficiently high for determining the order-to-disorder transition temperatures with adequate accuracy. The results of these experiments are shown in **Figure 7**.

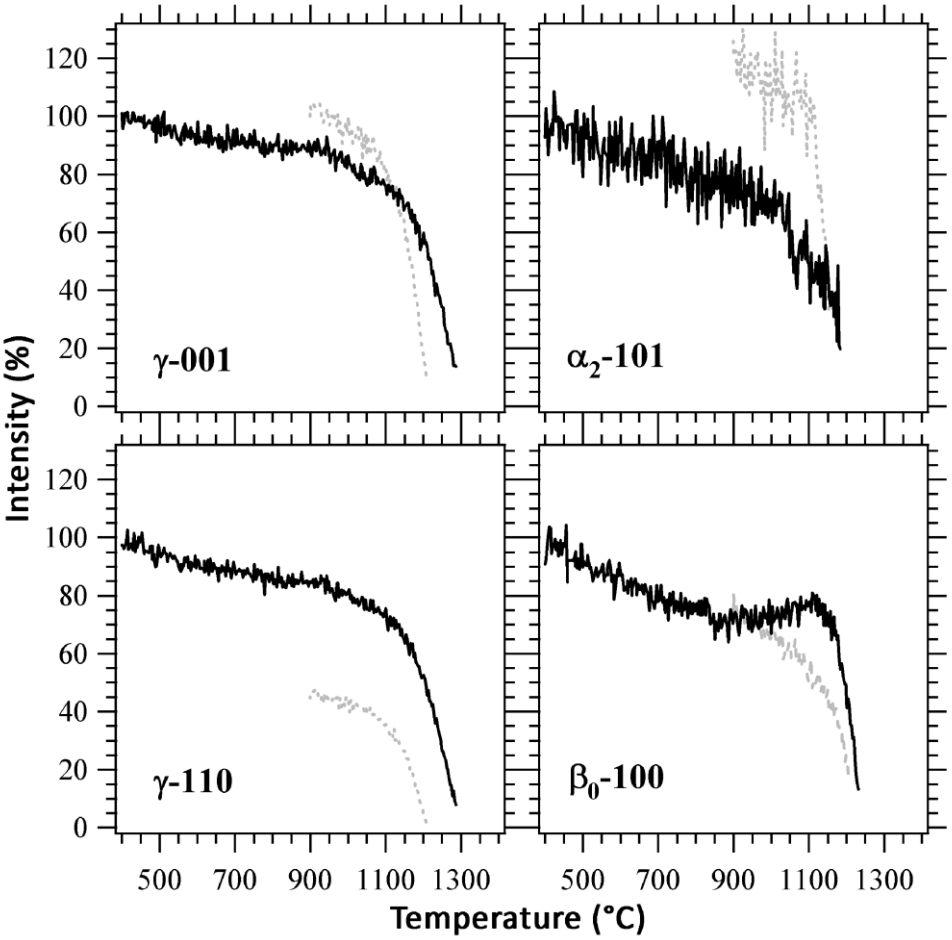

Figure 7: Ordering-disordering temperatures of α/α_2 and β/β_o in a Ti-43.27 Al-3.84 Nb-1.01 Mo-0.11 B alloy. Additionally, the dissolution and formation temperatures of the γ phase are shown. Data obtained on heating are shown as solid lines whereas intensity values recorded during cooling are represented by dashed lines. The intensities of superstructure peaks are plotted as a function of temperature. Intensity values are normalized to the intensity observed at 400°C. Disordering or dissolution of a phase is marked by a sharp decrease in intensity of the corresponding peak.[29]

In Figure 7, the intensity of the corresponding reflection is plotted versus temperature for a heating and a cooling ramp. It is clearly visible that different transition temperatures are observed upon heating and cooling which is attributed to the kinetics of the corresponding material. As reported earlier, the $\alpha_2 \leftrightarrow \alpha$ and $\beta_o \leftrightarrow \beta$ reactions progress relatively fast, whereas the dissolution and formation of γ phase occurs more reluctantly.[29]

Although the ordered phases in TiAl alloys show only weak intensities for superstructure peaks in X-ray diffraction, they are usually sufficiently high for determining the order/disorder transition temperatures. It is important to note that the alloying

elements (e.g. Mo and Nb) have large scattering lengths and can, therefore, influence the structure factors significantly. In **Figure 8** the intensities are plotted for superstructure reflections of the ordered phases in a Ti-44 Al-3 Mo alloy. The data for this plot were obtained from the same experiment described in Section 3.2.

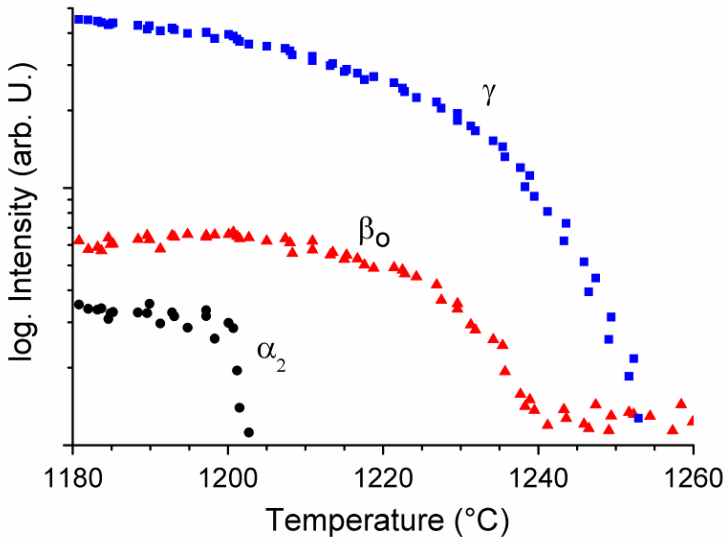

Figure 8: Disordering of α_2 and β_o as well as dissolution of the γ-phase in Ti-44 Al-3 Mo during continuous heating with a rate of 0.033 Ks^{-1} The intensity of superstructure peaks is plotted as a function of temperature. Intensity values were obtained by fitting a Gaussian to the corresponding peak of the azimuthally integrated HEXRD pattern.

In Figure 8 the loss of order in the α_2 and β_o phase upon heating is indicated by vanishing of the intensity, while the disappearance of the γ-phase reflection indicates its dissolution at the α-transus temperature. The results were obtained from fitting a Gaussian to the corresponding peak after performing a background correction. As soon as the intensity reached zero values, the fitting routine was disrupted.

From these results, it is obvious that the ordering behavior of intermetallic TiAl alloys can be investigated elegantly by means of in-situ diffraction methods. While the interpretation of neutron diffraction data is comparatively simple, smaller intensities of superstructure reflections may complicate the interpretation in HEXRD experiments.

5. Recovery and Recrystallization during Deformation of TiAl

5.1 General aspects

A various range of methods exists for performing X-ray diffraction experiments with the scope to investigate structural changes in crystalline materials. Conventional angle-dispersive or energy-dispersive powder diffraction methods, which average over a large number of crystallites, allow obtaining information on phase fractions, texture, and lattice parameters. If, however, a small number of crystallites are illuminated by a monochromatic beam, information on individual crystallites can be gained from their reflection spots on the Debye-Scherrer rings.[70] Alternatively, white beam Laue diffraction can be used to perform diffraction experiments in which only a few grains are illuminated. In principle, there are two different methods of performing diffraction experiments in materials science: If a monochromatic beam is used, a sample with many crystallites is illuminated which creates Debye-Scherrer cones that image as rings or sections of rings on a two-dimensional area detector. If experiments with a white X-ray beam are performed, usually only one or very few crystallites are illuminated during the experiment. This results in a Laue pattern which is characteristic for the crystal lattice and its orientation with respect to the incident beam. A synchrotron based method of micro beam Laue diffraction has recently evolved large impact in the materials science and engineering community.[79-81]

One classical field of application of the white beam Laue technique is the adjustment of the orientation of TiAl single crystals as performed by Inui et al.[82] In contrast to powder diffraction experiments, the reflections of the lattice planes stay visible in Laue experiments if the crystal is rotated about an arbitrary axis. Therefore, the Laue technique is very well suited for investigating the deformation and recrystallization behavior of single crystals. With this method, the occurrence of dynamic recrystallization in high purity Al single crystals has been shown.[83][84] While this method offers new insights in the behavior of one or a few crystals, it is less suited for investigating a fine-grained polycrystalline sample.

In contrast to this, a large number of grains is usually illuminated in powder diffraction experiments. Investigations with monochromatic radiation were originally performed in such a way that only a small section of the Debye-Scherrer rings was recorded on a photographic film or with a one-dimensional detector. In these cases it is necessary to use texture-free samples with a small grain size in order to obtain an intensity profile that is representative for the whole specimen. These requirements can be met by using a powder sample, which is the reason why the term powder diffraction has been established for this type of investigations, even if solid polycrystalline samples are concerned. As the electronic detector technology evolved, first one-dimensional and later on two-dimensional detectors became available. With modern CCD detectors used at synchrotron sources, it is possible to acquire a complete two-dimensional powder diffraction pattern in fractions of a second.[85]

However, for most applications such as the evaluation of phase fractions, 3rd order internal stresses etc. the two-dimensional detector images are usually integrated over the azimuthal angle ψ in order to obtain a pattern in which the intensity is plotted versus the scattering vector q. Thereby, the influence of fiber textures averages out for the condition that the fiber is perpendicular to the incident beam and the requirement of illuminating a large number of grains is much less stringent compared to powder diffraction experiments with a point detector. If investigations are targeted towards directionally dependent properties, integration is performed only over azimuthal angle segments [86]. With this method it is possible to determine for instance the macroscopic strain perpendicular to the beam direction from one single detector image.

One drawback of the classical powder diffraction approach is that no information on individual grains can be retrieved from such an experiment. A new technique has emerged during the last years by which it is possible to track the reflections of individual grains over time. This is achieved by rotating the specimen in such a way that reflections from all grains in the investigated volume are obtained. For further information on this so-called three dimensional X-ray diffraction microscopy (3D-XRD) technique the reader is referred to the corresponding literature.[87-89] The result of a 3D-XRD experiment is a reconstructed volume in which the shape and orientation of the individual grains are indicated. Drawbacks of this technique are that only a limited number of grains can be tracked at the same time and that a large number of detector images have to be acquired at different detector positions to be able to reconstruct the illuminated sample volume. Since this is time consuming, 3D-XRD is only suited for in-situ studies if the processes of interest are occurring at a slow rate. In addition to that it has to be born in mind that the reconstruction process is mathematically demanding and requires the use of fast algorithms.[89]

A different approach to study processes such as recovery, recrystallization and grain growth is to monitor the intensity distribution of one or more Debye-Scherrer rings over time. If a large number of grains are illuminated by the incident beam, so that the reflection spots of single crystallites are no longer discernable, only information concerning texture and strain can be derived from the intensity distribution as a function of ψ. However, if reflections from single grains can be distinguished, additional information is contained in the data.[32] The patterns can be evaluated with respect to a variety of parameters, such as number of spots, morphology of individual reflection spots, arrangement of different spots, and their evolution with time.

A simplified model of the development of individual reflection spots dependent on the different processes that occur in the material during hot-working is presented in **Figure 9**.

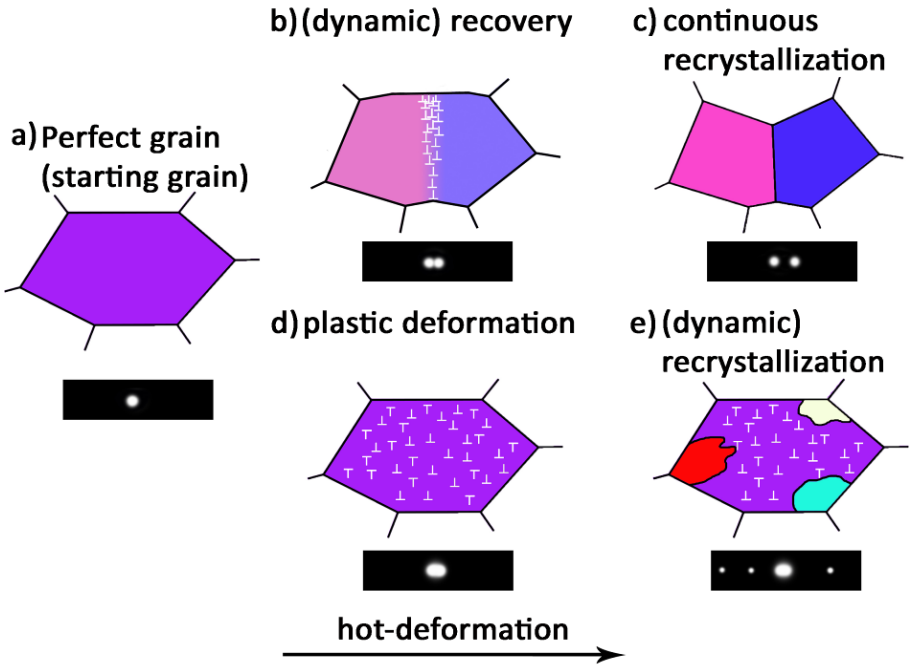

Figure 9: Schematic model that illustrates the development of reflection spots dependent on the different processes that might occur during hot-deformation of TiAl alloys. Starting with a perfect grain, plastic deformation increases from left to right. The development of the corresponding reflection spot is indicated below. In (a), a sharp reflection spot of a perfect grain is visible. Images (b) and (c) show how dislocations are introduced by plastic deformation which form a subgrain boundary in (b) through dynamic recovery processes and eventually a high-angle grain boundary in (c). In contrast to this, images (d) and (e) show a case where the defect density increases until the onset of recrystallization which is illustrated by the nucleation of new grains. The sketch reflects the development if the incident beam is monochromatic.

In Figure 9 a, a perfect grain is depicted which produces a reflection spot whose width is only determined by the instrumental parameters and the grains size. If the grain undergoes plastic deformation, defects are generated. Frequently, the deformation in metals is facilitated by dislocation motion which was also assumed for Figure 9. If the temperature during deformation is sufficiently high, dynamic recovery might occur, which is characterized by the arrangement of dislocations in low-energy configurations (Figure 9 (b)). Newly formed low-angle grain boundaries tilt different regions of the grain by a small angle. This causes the corresponding reflection spot to broaden in the direction normal to the tilt axis. Recovery can occur to such an extent that high angle grain boundaries are formed in which case this process is referred to as continuous recrystallization.[90] The reflection spot then splits in two, each one corresponding to an individual crystallite (Figure 9 (c)).

An alternative method of decreasing the defect density is illustrated in the lower section of Figure 9. In (d), the dislocations are randomly distributed which causes the reflection to broaden with respect to the azimuthal angle and the scattering vector distribution (i.e. the Bragg angle). If a certain defect density is attained and the temperature for dynamic recrystallization reached, the grain begins to recrystallize (Figure 9 (e)). The newly nucleated grains have low defect density and, therefore, produce sharp reflection spots. They also have a different orientation than the parent grain which causes reflection spots to appear at different azimuthal angles if they fulfill the Bragg condition (Figure 9 (e)). Depending on whether the material or phase of interest predominantly shows recovery or recrystallization under the conditions of the experiment, the diffraction patterns are affected in different ways. By the development of the patterns during deformation it is therefore possible to distinguish these two processes.

5.2 Analysis of diffraction data

By evaluating the relative positions of reflection spots on different Debye-Scherrer rings, which is referred to as reciprocal space mapping, it was possible to investigate how differently oriented grains in a massively transformed TiAl sample rearrange into single grains upon heating.[75][91] Careful analysis of single diffraction patterns even allowed tracing the phase transformation of single grains by the observation of diffuse streaking between parent and newly emerging grains in a TiAl alloy.[62] To be able to observe streaking or the grouping of reflection spots of different phases at similar azimuthal angles, individual detector images have to be analyzed manually. With modern flat panel detectors operated at several frames per second this is tedious and time consuming even for rather short in-situ experiments. Additionally, the tracking of individual reflections over time is difficult to achieve. A simple and elegant method for visualizing the development of spots of the same crystallographic plane is to integrate over a small range of the Bragg angle θ in which the corresponding reflections occur and to plot the thereby acquired intensity as a function of azimuthal angle ψ and time which results in a so-called azimuthal angle-time (AT) plot.[32]

This kind of data representation was used by Yan et al. to illustrate the formation of texture during deformation of an initially coarse grained Cu specimen.[92] In this study, the occurrence of microstructural processes, such as dislocation activity and subgrain formation is mentioned, but not elaborated on. In contrast to this, recovery and recrystallization processes were found to occur in a Zr alloy during hot compression in a similar experimental setup.[93] The angular spread of single reflection spots allowed deriving the mosaicity of the corresponding grains and the formation of subgrains was observed by the development of single spots with large angular spread into many sharp reflections separated only by a small angle. Recrystallization was identified by the rapid appearance and disappearance of reflections during a latter stage of the experiment. Austenitic steel, which can deform by a

twinning induced plasticity mechanism, has also been subject to investigation by this newly developed method.[94] In this case, it was shown that the material deforms by dislocation slip as well as twinning and the texture development during deformation was compared with the results of an elasto-plastic self-consistent model.

5.3 Hot deformation of Ti-43.5 Al-4 Nb-1 Mo-0.1 B

With the above described approach, the hot-deformation behavior of a Ti-43.5Al-4Nb-1Mo-0.1B (in at%) was investigated at the ESRF in Grenoble, France.[70] This is of particular interest since the difficult hot-working characteristics of TiAl alloys are one of the reasons why this material class has found only limited applications so far. Therefore, the aim of these investigations was to obtain a better understanding of the materials behavior during hot-forming operations. To this end, specimens were resistively heated between the anvils of an electro thermomechanical tester from Instron, Norwood (MA), USA, to 1300°C and subsequently compressed. Details on the experimental procedure are given elsewhere.[70] Specimens were cylindrical with a diameter of 4 mm and a length of 8 mm. These dimensions were chosen because they enable characterizing the materials behavior in the bulk of the sample rather than its properties close to the surface. For recording the diffraction patterns, a Pixium 4700 (Thales Group, Neuilly-sur-Seine, France) flat panel detector [85] was used and operated at a frame rate of approximately 2 Hz. Throughout the experiment, the temperature was controlled with a type S thermocouple spot welded to the sample surface.

In **Figure 10** AT-plots of two selected reflections (a, b) and graphs of applied temperature, true stress, and true strain (c) are presented. Lines produced by the evolution of individual spots with time are designated as timelines. Continuous timelines during heating are observed for both phases, α and β. As the specimen is held within the (α+β) phase field at 1300°C, fluctuations in the β-phase reflections are visible while the α-reflections remain static. When deformation starts, immediate changes in the appearance of the intensity distribution are apparent in the insets of Figure 10 (a) and (b). While the α-phase exhibits inclined, continuous timelines, the β-phase reflections broaden and become dotty. Another distinctive attribute is the blurred appearance of the α-phase timelines, while those of the β-phase remain sharp dots in the AT-plot. At t = 215 s, the sample was unloaded for 30 s to investigate the materials response. It can be seen in Figure 10 (a) that the α-timelines remain continuous during this period, but still appear to be blurred. In contrast to this, the β-phase reflections fluctuate fast and the timelines are sharp (Figure 10 (b)).

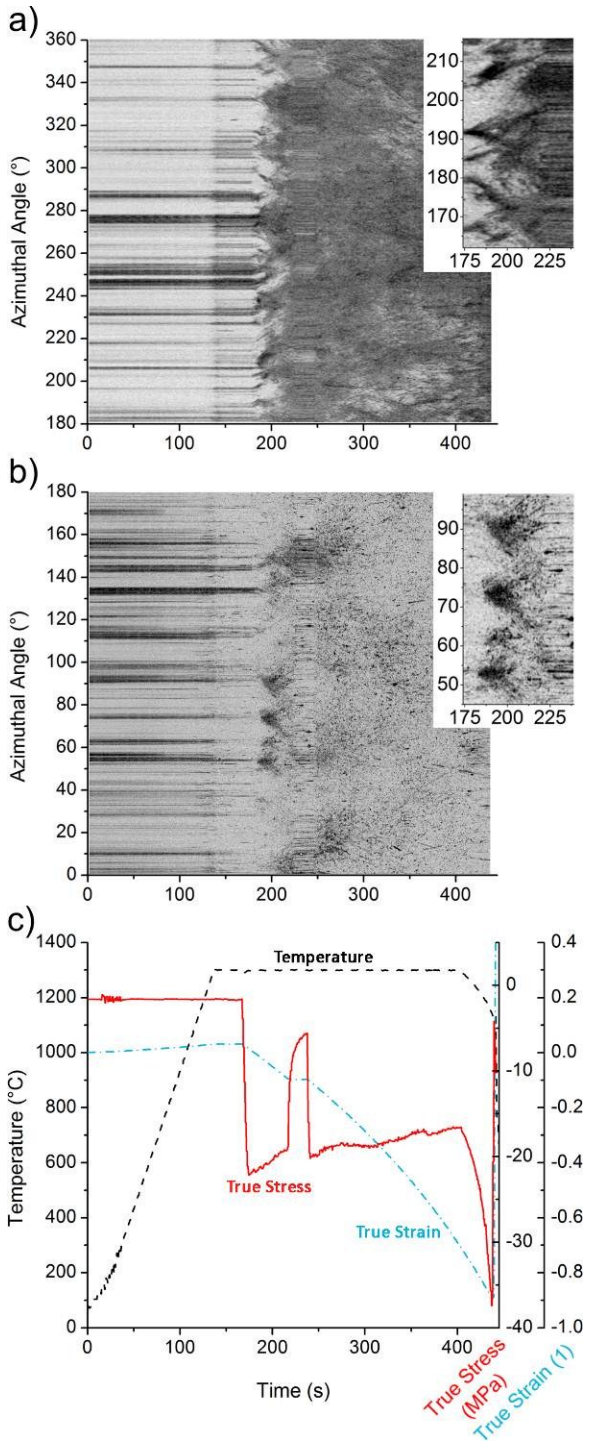

Figure 10: In-situ hot-deformation experiment conducted on a Ti-43.5 Al-4 Nb-1 Mo-0.1 B alloy (nominal).[70] Azimuthal angle-time plots of the (a) α 012 reflection and the (b) β 002 reflection. The experimental parameters such as temperature (dashed line), true stress (solid line), and true strain (dash-dotted line) are shown in (c). The insets visible at the upper right corner of (a) and (b) indicate the development of the reflections at the beginning of the hot-compression test at higher magnification.

Inclined timelines are observed if the crystal lattice of a grain rotates about an axis that is parallel to the incident beam, whereas broadening of a reflection is indicative of an increasing defect density within the corresponding grain.[95][68] The formation of many sharp dots stemming from one original reflection and occurring within a small angular range is caused by the formation of subgrains through a dynamic recovery process.[93][70] Since peak broadening immediately followed by the formation of reflection dots was observed in Figure 10 b it was derived that fast dynamic recovery processes are dominating in the β-phase. In the α-phase, however, the reflections are inclined and blurred indicating the deformation by dislocation slip and the presence of high defect densities. The absence of reflections with low angular spread points towards a slow recovery process instead of a discontinuous recrystallization process.

To validate the results from the in-situ HEXRD experiment, electron-backscatter diffraction (EBSD) experiments were performed on the deformed specimens. The images shown in **Figure 11 a** and b were acquired with a LEO 1525 field emission SEM equipped with an EDAX EBSD system.

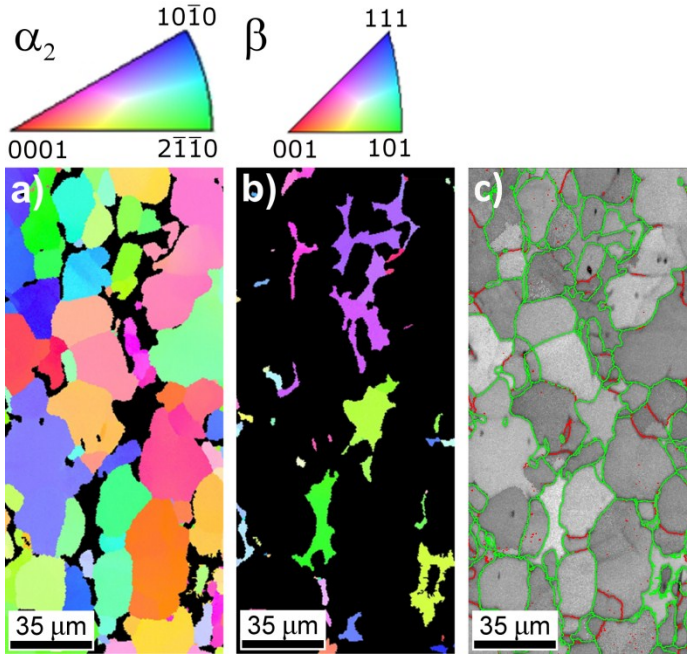

Figure 11: Micrographs obtained after the in-situ hot-compression experiment on a Ti-43.5 Al-4 Nb-1 Mo-0.1 B alloy (nominal) by means of EBSD (a, b) and SEM in BSE mode (c). Image (a) shows elongated grains of the α_2-phase, whereas the intricately shaped β_o-phase is visible in (b). In image (c), high-angle grain boundaries (misorientation greater 15°) are indicated by green lines, whereas small-angle grain boundaries are red. The loading direction was horizontal.

Orientations are indicated in color-code, the legends for the corresponding phases are located above the EBSD images. Figure 11 c shows a micrograph of the same sample area obtained in BSE mode. From this image, it is obvious that the deformation experiment was conducted in the (α+β) phase region.

From Figure 11 it can be seen that the α-phase formed elongated grains during deformation that are divided into a small number of equiaxed subgrains, whereas practically no small angle grain boundaries are visible in the β/β_o-grains. It should also be noted that the β_o-grains exhibit complex shapes which can be attributed to the fact that at high-temperatures, the β-phase accommodates a disproportionately large fraction of the plastic strain.[96-98] In both phases, no indication for dynamic recrystallization was found. Consequently, the conclusions drawn from the results of the AT plots could be verified by EBSD.

With the method described above, it is possible to derive the deformation, recovery and recrystallization behavior of the individual phases during in-situ experiments conducted on multi-phase alloys. It is, however, not possible to monitor and track a single grain throughout the whole experiment or to determine the shape and position of individual grains. Nonetheless, valuable information about the microstructural development can be derived by applying this method.

A complementary approach to investigate the materials evolution during production processes is to measure the texture before and after forming or heat-treatment steps of interest. Orientation distribution functions can be determined by means of neutron diffraction [99][100] as well as by XRD by using laboratory [101-103] or synchrotron sources [31][92]. Neutrons and high-energy X-rays offer the benefit of high penetration depths and, therefore, allow investigating large sample volumes which leads to excellent grain statistics. Another advantage of neutron diffraction in case of TiAl alloys is that only a reduced number of Bragg-reflections are visible which minimizes problems that arise from overlapping α and γ reflections.[99]

Brokmeier et al. [99] used this method for investigating the texture of TiAl alloys after extrusion. It was found that the sharpness of the texture is dependent on extrusion temperature as well as on alloy composition. The influence of carbon additions to a TiAl alloy on texture formation during hot-rolling was investigated by Stark et al. [102], while Schillinger et al. [103] derived the primary deformation mechanisms during rolling from texture measurements. Texture development during hot compression of Cu, Ni, and a γ-TiAl alloy was investigated by Hasegawa et al. which compared the dynamic recrystallization behavior of these three metals.[101] From the results of these experiments, these authors were able to derive the primary deformation mechanisms at different temperatures and deformation conditions.

6. Lattice Parameter and Thermal expansion

For a material class that is intended for use in high-temperature applications, the response of the material on exposure to high-temperatures is of vital interest. Lattice parameters in all three dimensions can be tracked with relative ease in diffraction experiments. If the volume of the unit cell is plotted as a function of temperature, the gradient of the resulting curve at a certain temperature is the linear coefficient of thermal expansion (CTE) at this temperature.[104]

With this method Novoselova et al. [104] have determined the CTE of a Ti-46 Al-1.9 Cr-3 Nb alloy. It has to be stressed that the values measured in diffraction experiments only reflect the increase in lattice parameter, whereas the CTE is known to be affected also by the formation of thermal vacancies. Additionally, the lattice parameter may be influenced by the formation of elastic strains between adjacent phases due to differences in the CTEs.[68] In other publications only the development of lattice parameters was investigated and related to changes in the microstructure and phase composition.[74][75] **Figure 12** shows the temperature dependence of the c/a ratio of the γ-phase in a Ti-43.5 Al-4 Nb-1 Mo-0.1 B alloy. In this experiment, a heating rate of 10 K/s was used. Yeoh et al. [74] investigated a Ti-45 Al-7.5 Nb-0.5 C alloy and related the development of the c/a ratio of the γ-phase similar to the one observed in Figure 12 to the decrease in its Al content at temperatures higher than 900°C.

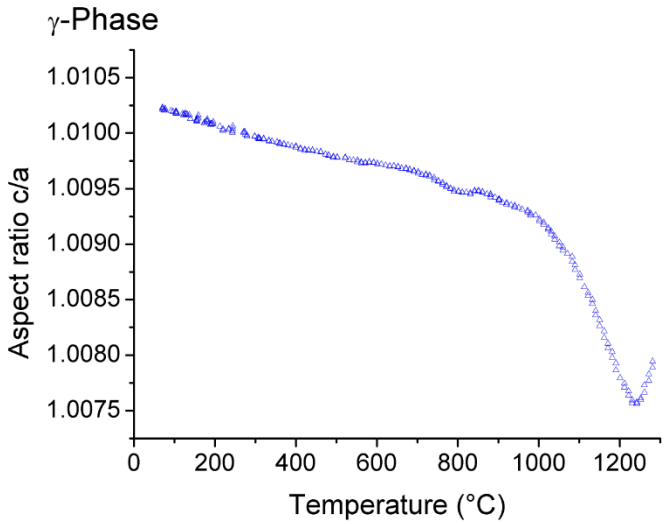

Figure 12: Ratio of the lattice parameters in crystallographic c and a axis of the γ-phase in Ti-43.5 Al-4 Nb-1 Mo-0.1 B as a function of temperature.

At 1230°C, the γ-phase exhibits the lowest c/a ratio before it starts to increase again. From this behavior it is concluded that the Al content is lowest at that temperature. This shows exemplarily how information on the materials behavior can be derived from the

development of the lattice parameter. In many applications, knowledge on the development of the lattice parameters with temperature is important, i.e. when the use of protective coatings is considered or the impact of phase transitions on internal stresses is of relevance. Diffraction experiments allow obtaining information on the lattice parameters of individual phases in a multi-phase material. Additionally, they reveal effects such as the one shown in Figure 12 that strongly influence the thermal behavior.

7. Summary and Outlook

Diffraction methods using neutrons and/or high-energy X-rays offer unique opportunities for investigating various aspects of importance for the development of TiAl alloys. The possibility of performing experiments in-situ is a great advantage especially for investigating fast phase transformations, such as the $\alpha \leftrightarrow \alpha_2$ and $\beta \leftrightarrow \beta_o$ ordering/disordering reactions. Additionally, diffraction methods are capable of incorporating small regions of an individual phase if phase fractions are determined. This is especially important in this alloy system, since lamellar grains that consist of fine γ and α_2-lamellae are a common microstructural feature. The different contrast formation for neutrons and X-rays in TiAl alloys is a peculiarity that makes these quite similar techniques complementary ones, which was emphasized in this review with selected examples. Progresses in detector technology and the construction of dedicated high-energy X-ray diffraction beamlines have enabled conducting diffraction experiments at high frame rates, offering the opportunity to directly observe processes that occur comparatively fast. Parallel to the hardware development, new techniques have emerged that comprise valuable tools for various applications in materials science. Experiments with nano-beams and the three-dimensional X-ray diffraction microscopy are examples for methods that have great potential for future investigations. Without doubt, during the last 20 years, the use of diffraction methods has significantly contributed to the development of TiAl alloys and production routes and will continue to provide interesting results in the near future.

References

[1] M. Yamaguchi, H. Inui, K. Ito, *Acta Materialia* **2000**, *48*, 307-322.

[2] F. Appel, R. Wagner, *Materials Science and Engineering: R: Reports* **1998**, *22*, 187-268.

[3] Y. Kim, H. Clemens, A. Rosenberger, *Gamma Titanium Aluminides 2003*, The Minerals, Metals And Materials Society (TMS), Warrendale, PA, USA **2003**.

[4] Y. Kim, in *Structural Aluminides for Elevated Temperature Applications*, TMS, Warrendale **2008**, 215.

[5] M. Peters, P. Leyens, *Titanium and Titanium Alloys*, Wiley-VCH, Weinheim, Germany **2003**.

[6] Y. Kim, *J. Met.* **1994**, 30.

[7] M.S. Kesler, S. Goyel, O. Rios, D.M. Cupid, H.J. Seifert, F. Ebrahimi, *Materials Science and Engineering: A* **2010**, *527*, 2857-2863.

[8] X. Wu, *Intermetallics* **2006**, *14*, 1114-1122.

[9] F. Appel, M. Oehring, R. Wagner, *Intermetallics* **2000**, *8*, 1283-1312.

[10] W.F. Cui, *Intermetallics* **2007**, *15*, 675-678.

[11] H. Baur, R. Joos, W. Smarsly, H. Clemens, in *Intermetallics and Superalloys*, Wiley-VCH, Weinheim, Germany **2000**, 384.

[12] T. Tetsui, in *Gamma Titanium Aluminides 1999*, The Minerals, Metals And Materials Society, TMS, Warrendale, PA, USA **1999**, 15.

[13] W. Smarsly, H. Baur, G. Glitz, H. Clemens, T. Khan, M. Thomas, in *Structural Intermetallics 2001*, The Minerals, Metals And Materials Society, TMS, Warrendale, PA, USA **2001**, 25.

[14] A. Sommer, G. Keijzers, The Minerals, Metals And Materials Society (TMS), Warrendale, PA, USA **2003**, 3-8.

[15] A. Lasalmonie, *Intermetallics* **2006**, *14*, 1123-1129.

[16] H. Clemens, A. Bartels, S. Bystrzanowski, H. Chladil, H. Leitner, G. Dehm, R. Gerling, F.P. Schimansky, *Intermetallics* **2006**, *14*, 1380-1385.

[17] H. Clemens, W. Wallgram, S. Kremmer, V. Güther, A. Otto, A. Bartels, *Advanced Engineering Materials* **2008**, *10*.

[18] R.M. Imayev, V.M. Imayev, M. Oehring, F. Appel, *Intermetallics* **2007**, *15*, 451-460.

[19] W. Wallgram, T. Schmoelzer, L. Cha, G. Das, V. Güther, H. Clemens, *International Journal of Materials Research* **2009**, *100*, 1021-1030.

[20] R.M. Imayev, V.M. Imayev, M. Oehring, F. Appel, *Intermetallics* **2007**, *15*, 451-460.

[21] H. Clemens, H.F. Chladil, W. Wallgram, G.A. Zickler, R. Gerling, K.D. Liss, S. Kremmer, V. Güther, W. Smarsly, *Intermetallics* **2008**, *16*, 827-833.

[22] E. Abe, T. Kumagai, M. Nakamura, *Intermetallics* **1996**, *4*, 327-333.

[23] L. Cha, C. Scheu, H. Clemens, H. Chladil, G. Dehm, R. Gerling, A. Bartels, *Intermetallics* **2008**, *16*, 868-875.

[24] R.D. Shull, *High Temperature Science* **1988**, *26*, 95-117.

[25] Y.W. Kim, *Materials Science and Engineering A* **1995**, *192-193*, 519-533.

[26] S. Swaminathan, *Philosophical Magazine Letters* **1996**, *73*, 319-330.

[27] Y.W. Kim, *Acta Metallurgica Et Materialia* **1992**, *40*, 1121-1134.

[28] M.A. Grinfeld, *Metallurgical and Materials Transactions A: Physical Metallurgy and*

Materials Science **1998**, *29*, 937-942.

[29] T. Schmoelzer, K.D. Liss, G.A. Zickler, I.J. Watson, L.M. Droessler, W. Wallgram, T. Buslaps, A.J. Studer, H. Clemens, *Intermetallics* **2010**, *18*, 1544.

[30] I.J. Watson, *Advanced Engineering Materials* **2009**, *11*, 932-937.

[31] K. Liss, A. Bartels, A. Schreyer, H. Clemens, *Textures and Microstructures* **2010**, *35*, 219-252.

[32] K. Liss, K. Yan, *Materials Science and Engineering: A* **2010**, 528, 11-27.

[33] W. Reimers, A. Pyzalla, A. Schreyer, H. Clemens, *Diffraction Methods in Engineering Materials Science*, Wiley-VCH, Weinheim, Germany **2008**.

[34] A. Schreyer, in *Diffraction Methods in Engineering Materials Science*, Wiley-VCH, Weinheim, Germany **2008**, 79.

[35] R. Treusch, in *Diffraction Methods in Engineering Materials Science*, Wiley-VCH, Weinheim, Germany **2008**, 97.

[36] W. Knop, P. Pranzas, P. Schreiner, in *Diffraction Methods in Engineering Materials Science*, Wiley-VCH, Weinheim, Germany **2008**, 91.

[37] K. Hashimoto, *Intermetallics* **1998**, *6*, 667-672.

[38] N. Ashcroft, *Solid State Physics*, Holt Rinehart And Winston, New York **1976**.

[39] H. Rauch, W. Waschowski, in *Neutron Data Booklet*, Old City Publishing, Philadelphia **2003**, 1-17.

[40] M. Kimura, *Journal of Phase Equilibria* **1999**, *20*, 224-230.

[41] G.W. Qin, *Metallurgical and Materials Transactions A: Physical Metallurgy and Materials Science* **2001**, *32*, 1927-1938.

[42] S. Kremmer, H. Chladil, H. Clemens, A. Otto, V. Güther, in *Ti-2007 Science and Technology*, The Japan Institute Of Metals (JIM), Sendai, Japan **2008**, 989-992.

[43] F.S. Sun, C.X. Cao, S.E. Kim, Y.T. Lee, M.G. Yan, *Metallurgical and Materials Transactions A: Physical Metallurgy and Materials Science* **2001**, *32*, 1573-1589.

[44] R. Kainuma, Y. Fujita, H. Mitsui, I. Ohnuma, K. Ishida, *Intermetallics* **2000**, *8*, 855-867.

[45] H. Clemens, W. Wallgram, S. Kremmer, V. Güther, A. Otto, A. Bartels, *Advanced Engineering Materials* **2008**, *10*.

[46] M. Takeyama, S. Kobayashi, *Intermetallics* **2005**, *13*, 993-999.

[47] N. Saunders, in *Gamma Titanium Aluminides*, TMS, Warrendale, PA **1999**, 183.

[48] H. Clemens, B. Boeck, W. Wallgram, T. Schmoelzer, L.M. Droessler, G.A. Zickler, H. Leitner, A. Otto, in *Materials Res. Soc. Symp. Proc.*, MRS Warrendale **2008**, 115-120.

[49] T. Hamajima, G. Luetjering, S. Weissmann, in *Red Books, Vol. XVIII*, **1972**.

[50] R. Hansen, R. Aravamudham, *Metallkunde* **1970**, 115.

[51] A.K. Singh, D. Banerjee, *Metallurgical and Materials Transactions A: Physical Metallurgy and Materials Science* **1997**, *28*, 1745-1753.

[52] T. Schmoelzer, S. Mayer, C. Sailer, F. Haupt, V. Güther, P. Staron, K. Liss, H. Clemens, *Accepted for publication in Advanced Engineering Materials,* DOI:10.1002/adem.201000263.

[53] A.P. Hammersley, S.O. Svensson, M. Hanfland, A.N. Fitch, D. Häusermann, *High Pressure Research* **1996**, *14*, 235-248.

[54] O. Shuleshova, D. Holland-Moritz, W. Löser, A. Voss, H. Hartmann, U. Hecht, V.T. Witusiewicz, D.M. Herlach, B. Büchner, *Acta Materialia,* **2010**, 58, 2408-2418.

[55] O.N. Senkov, *Scripta Materialia* **2002**, *46*, 187-192.

[56] P. Staron, U. Christoph, F. Appel, H. Clemens, *Applied Physics A: Materials Science and Processing* **2002**, *74*.

[57] M. Beschliesser, A. Chatterjee, A. Lorich, W. Knabl, H. Kestler, G. Dehm, H. Clemens, *Materials Science and Engineering A* **2002**, *329-331*, 124-129.

[58] H.A. Zhu, *Scripta Materialia* **2005**, *52*, 45-50.

[59] L.M. Droessler, T. Schmoelzer, W. Wallgram, L. Cha, G. Das, H. Clemens, in *Materials Res. Soc. Symp. Proc.*, MRS, Warrendale **2008**, 121-126.

[60] G.A.B. Dehm, *Advanced Engineering Materials* **2006**, *8*, 1033-1045.

[61] J. Tang, *Materials Research Bulletin* **2001**, *36*, 1737-1742.

[62] K-D. Liss, A. Stark, A. Bartels, H. Clemens, T. Buslaps, D. Phelan, L.A. Yeoh, *Advanced Engineering Materials* **2008**, *10*, 389-392.

[63] H. Zhu, *Materials Science and Engineering A* **2005**, *397*, 58-64.

[64] M. Blackburn, in *The Science, Technology and Application of Titanium*, Pergamon Press Ltd., Oxford **1970**, 633-643.

[65] E. Eidenberger, M. Schober, T. Schmoelzer, E. Stergar, P. Staron, H. Leitner, H. Clemens, *Physica Status Solidi A* **2010**, 207, 2238-2246.

[66] K-D. Liss, R.E. Whitfield, W. Xu, T. Buslaps, L.A. Yeoh, X. Wu, D. Zhang, K. Xia, *Journal of Synchrotron Radiation* **2009**, *16*, 825-834.

[67] K. Yan, D.G. Carr, S. Kabra, M. Reid, A. Studer, R. Harrison, R. Dippenaar, K-D. Liss, *World Journal of Engineering* **2010**, in press.

[68] B. Warren, *X-Ray Diffraction*, Dover Publications, New York **1990**.

[69] M. Grujicic, Y. Zhang, *Journal of Materials Science* **1999**, *34*, 1419-1437.

[70] K. Liss, T. Schmoelzer, K. Yan, M. Reid, M. Peel, R. Dippenaar, H. Clemens, *J. Appl. Phys.* **2009**, *106*, 113526.

[71] T. Tetsui, K. Shindo, S. Kaji, S. Kobayashi, M. Takeyama, *Intermetallics* **2005**, *13*, 971-978.

[72] S. Kim, *Materials Science and Engineering A* **1998**, *250*, 77-82.

[73] S. Kim, *Materials Science and Engineering A* **1997**, *239-240*, 229-234.

[74] L.A. Yeoh, K. Liss, A. Bartels, H. Chladil, M. Avdeev, H. Clemens, R. Gerling, T. Buslaps, *Scripta Materialia* **2007**, *57*, 1145-1148.

[75] K.D. Liss, A. Bartels, H. Clemens, S. Bystrzanowski, A. Stark, T. Buslaps, F.P. Schimansky, R. Gerling, C. Scheu, A. Schreyer, *Acta Materialia* **2006**, *54*, 3721-3735.

[76] M. Hoelzel, *Physica B: Condensed Matter* **2004**, *350*, E671-E673.

[77] R. Gilles, *Zeitschrift Fur Kristallographie* **2006**, *221*, 183-188.

[78] A.J. Studer, M.E. Hagen, T.J. Noakes, *Physica B: Condensed Matter* **2006**, *385-386*, 1013-1015.

[79] R.I. Barabash, G. Ice, F. Walker, *Journal of Applied Physics* **2003**, *93*, 1457-1464.

[80] B.C. Larson, W. Yang, G. Ice, J. Budai, J. Tischler, *Nature* **2002**, *415*, 887-890.

[81] C. Kirchlechner, D. Kiener, C. Motz, S. Labat, N. Vaxelaire, O. Perroud, J. Micha, O. Ulrich, O. Thomas, G. Dehm, J. Keckes, *Phil. Mag.* **2010**, 1-9.

[82] H. Inui, M. Matsumuro, D.-. Wu, M. Yamaguchi, *Phil. Mag. A* **1997**, *75*, 395-423.

[83] K. Ihara, Y. Miura, *Materials Science and Engineering A* **2004**, *387-389*, 651-654.

[84] Y. Miura, K. Ihara, K. Fukaura, *Materials Science and Engineering A* **2000**, *280*, 134-138.

[85] J.E. Daniels, M. Drakopoulos, *Journal of Synchrotron Radiation* **2009**, *16*, 463-468.

[86] J.E. Daniels, *Journal of Applied Crystallography* **2008**, *41*, 1109-1114.

[87] L. Margulies, G. Winther, H.F. Poulsen, *Science* **2001**, *291*, 2392-2394.

[88] L. Margulies, T. Lorentzen, H.F. Poulsen, T. Leffers, *Acta Materialia* **2002**, *50*, 1771-1779.

[89] H. Poulsen, *Three-Dimensional X-Ray Diffraction Microscopy : Mapping Polycrystals and Their Dynamics*, Springer, Berlin, New York **2004**.

[90] R.D. Doherty, *Materials Science and Engineering A* **1997**, *238*, 219-274.

[91] K.D. Liss, H. Clemens, A. Bartels, A. Stark, T. Buslaps, in *Materials Res. Symp. Proc.,* MRS Warrendale, **2006**, 425-430.

[92] K. Yan, K.D. Liss, U. Garbe, J. Daniels, O. Kirstein, H. Li, R. Dippenaar, *Advanced Engineering Materials* **2009**, *11*, 771-773.

[93] K.D. Liss, U. Garbe, H. Li, T. Schambron, J.D. Almer, K. Yan, *Advanced Engineering Materials* **2009**, *11*, 637-640.

[94] K. Yan, D.G. Carr, M.D. Callaghan, K. Liss, H. Li, *Scripta Materialia* **2010**, *62*, 246-249.

[95] P. Sahu, *Intermetallics* **2006**, *14*, 180-188.

[96] F. Appel, *Advanced Engineering Materials* **2006**, *8*, 371-376.

[97] T.A. Tetsui, *Scripta Materialia* **2002**, *47*, 399-403.

[98] T.A. Tetsui, *Intermetallics* **2003**, *11*, 299-306.

[99] H-G. Brokmeier, M. Oehring, F. Appel, H. Clemens, *Applied Physics A: Materials Science and Processing* **2002**, *74*, S1222-S1223.

[100] H-G. Brokmeier, *Metallurgical and Materials Transactions A: Physical Metallurgy and Materials Science* **2004**, *35 A*, 3563-3579.

[101] M. Hasegawa, M. Yamamoto, H. Fukutomi, *Acta Materialia* **2003**, *51*, 3939-3950.

[102] A. Stark, A. Bartels, R. Gerling, F.P. Schimansky, H. Clemens, *Advanced Engineering Materials* **2006**, *8*, 1101-1108.

[103] W. Schillinger, A. Bartels, R. Gerling, F.P. Schimansky, H. Clemens, *Intermetallics* **2006**, *14*, 336-347.

[104] T. Novoselova, S. Malinov, W. Sha, A. Zhecheva, *Materials Science and Engineering A* **2004**, *371*, 103-112.

ADVANCED ENGINEERING MATERIALS

Appendix B:
In-situ Diffraction Experiments for the Investigation of Phase Fractions and Ordering Temperatures in Ti-44 at% Al-(3-7) at% Mo Alloys

T. Schmoelzer, S. Mayer, C. Sailer, F. Haupt, V. Güther, P. Staron, K.-D. Liss and H. Clemens

Advanced Engineering Materials **13** (4), 2011, pp. 306-311.

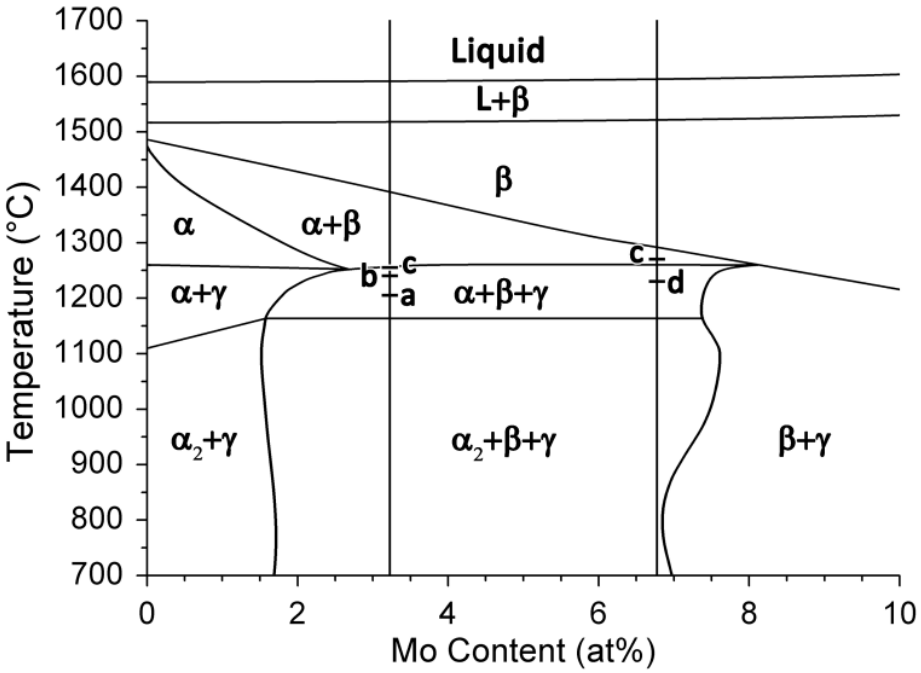

In-situ Diffraction Experiments for the Investigation of Phase Fractions and Ordering Temperatures in Ti-44 at% Al-(3-7) at% Mo Alloys.**

By *T. Schmoelzer*,* *S. Mayer*, *C. Sailer*, *F. Haupt*, *V. Güther*, *P. Staron*, *K.-D. Liss* and *H. Clemens*.

[*] *T. Schmoelzer, Dr. S. Mayer, C. Sailer, Prof. Dr. H. Clemens*
Department of Physical Metallurgy and Materials Testing,
Montanuniversität Leoben, 8700 Leoben, Austria.
E-mail: thomas.schmoelzer@schmoelzer.net
Dr. F. Haupt
GfE Fremat GmbH,
09599 Freiberg, Germany.
Dr. V. Güther
GfE Metalle und Materialien GmbH,
90431 Nuremberg, Germany.
Dr. P. Staron
Institute of Materials Research,
Helmholtz-Zentrum Geesthacht, 21502 Geesthacht, Germany.
Dr. K.-D. Liss
Australian Nuclear Science and Technology Organisation,
Lucas Heights, NSW 2232, Australia.

[**] *The support of DESY management, User Office and GKSS beamline staff is highly acknowledged. Research activities leading to the presented HEXRD results received funding from the European Community's Seventh Framework Programme (FP7/2007-2013) under grant agreement n°226716. A part of this study was conducted within the framework of the BMBF project O3X3530A, Germany, and the Styrian Materials Cluster, Austria.*

Being a strong β stabilizer, Mo has gained importance as an alloying element for so-called β/γ-TiAl alloys. Intermetallic TiAl-based alloys which contain a significant volume fraction of the body-centered cubic β-phase at elevated temperatures have proven to exhibit good processing characteristics during hot-working. Unfortunately, the effect of Mo on the appearing phases and their temperature dependence is not well known. In this work, sections of the Ti-Al-Mo ternary phase diagram derived from thermodynamic calculations as well as experimental data are presented. The phase transition temperatures stated in these phase diagrams are compared with the results of high-temperature diffraction studies using high-energy synchrotron radiation. Additionally, the disordering temperature of the β_o-phase is determined.

During the last twenty years, research and development efforts have been undertaken to develop γ-TiAl based alloys as a replacement for Ni-based superalloys for high-temperature applications in turbine blades of advanced aero engines and turbo-chargers of automotive combustion engines.[1] Intermetallic γ-TiAl based alloys are intended for use in the temperature range from 600 to 900°C and there is growing demand for alloys which can be deformed easily by cost-effective forming operations. One possible approach is to design alloys with microstructures in which homogenously distributed β and γ-phase are the main constituents.[2] Therefore, these alloys are named β/γ-alloys.[3] Since Mo is a strong β stabilizer, the ternary system Ti-Al-Mo is well suited for studying this type of alloys.[4] Despite the importance of Mo as an alloying element, the knowledge of its effect on phase diagram, transformation temperatures and order/disorder transition temperatures is limited. In many advanced multi-phase TiAl alloys, three intermetallic phases, γ, α_2, and β_o, are the dominating microstructural constituents, all of which are ordered at room temperature. At elevated temperatures, the ordered hexagonal α_2-phase ($D0_{19}$) disorders to α (A3) and the ordered cubic β_o-phase (B2) disorders to the body-centered cubic β-phase (A2) while the γ-phase ($L1_0$) remains ordered up to its dissolution temperature (T_γ). The phase fractions present have a strong influence on the mechanical properties of the material and on the processing characteristics at hot-working temperatures. High β/β_o-phase contents, for instance, improve the deformation behavior during hot-working, but simultaneously decrease the creep resistance if prevailing at service temperature.[5] Additionally, the room temperature ductility is negatively affected by high β_o-phase fractions.[6]

In the present work, sections of the ternary phase diagram Ti-Al-Mo, obtained by thermodynamic calculations and compiled from published experimental results, are presented. For the prediction of the constituent phases and related transition temperatures, thermodynamic calculations based on the CALPHAD method were conducted. To this end, the software package ThermoCalc® was applied using a commercial TiAl database.[7] In recent publications, however, the thermodynamic database used was found to poorly describe the transition temperatures and phase proportions in γ-TiAl based alloys bearing high contents of β stabilizing elements.[8][9]

To critically assess the calculated as well as the experimentally determined phase diagrams, two model alloys with a nominal composition of Ti-44Al-3Mo and Ti-44Al-7Mo were investigated. Note that all concentrations are given in atomic percent henceforth. For determining the phase evolution and phase transition temperatures, *in-situ* high-energy X-ray diffraction (HEXRD) experiments were conducted during continuous heating.[10] Additionally, differential scanning calorimetric (DSC) experiments were performed in order to determine T_γ with high accuracy. This allowed verifying the temperature values measured during the diffraction experiment. The results obtained by the diffraction experiments are

compared to the quasi-binary phase diagrams derived from thermodynamic calculations as well as from literature data and the differences are discussed.

Material and Experimental Methods

The two model alloys, Ti-44Al-3Mo (alloy 3M) and Ti-44Al-7Mo (alloy 7M), investigated were provided by GfE Metalle und Materialien GmbH, Nuremberg, Germany. Cylindrical ingots which were 200 mm long and 53 mm in diameter were produced by means of centrifugal casting. Subsequently, the ingots were hot-isostatically pressed (HIP) in order to close residual casting porosity and to bring the material closer to thermodynamical equilibrium conditions. HIPing was conducted at 200 MPa and 1200°C for 4 hrs followed by slow cooling within the HIP apparatus. By means of X-ray fluorescence spectroscopy, actual compositions of alloy 3M and 7M were determined to be Ti-44.58 Al-3.23 Mo-0.12 B and Ti-43.94 Al-6.78 Mo-0.09 B, respectively. For the correct interpretation of the experimental results, please note the deviation of the actual from the nominal Al content of the two alloys. Boron was added for refining the microstructure during solidification by the formation of borides. A significant influence on phase fractions or transformation temperatures, however, is not expected. The phases present and their distribution within the two alloys was analyzed using a Zeiss Evo 50 scanning electron microscope (SEM) in back-scattered electron (BSE) mode which exploits the different phase contrasts. Additionally, the chemical composition of the present phases was determined by energy dispersive X-ray spectroscopy (EDS) with an INCA system by Oxford Instruments, Tubney Woods, UK.

HEXRD experiments were performed at the HARWI II beamline of the GKSS Research Centre at the DORIS III synchrotron at DESY in Hamburg, Germany.[10-12] For heating the specimens, a custom built induction furnace was operated under Ar-atmosphere. The temperature of the 15 mm long cylindrical samples with a diameter of 5 mm was controlled by a differential pyrometer. A mean energy of 104.7 keV was adjusted for the 0.5×0.5 mm^2 beam. As detector a mar555 by MAR Research, Norderstedt, Germany was employed. The samples were rapidly heated to 1000°C, held at that temperature for 2 min, and then continuously heated to 1350°C at a rate of 2 $Kmin^{-1}$.

DSC measurements were performed on a labSys evo system from Setaram with a sample mass of 40 mg. The γ dissolution temperature was determined at three different heating rates and linearly extrapolated to a heating rate of 0 $Kmin^{-1}$ in order to obtain the dissolution temperature of the γ-phase in thermodynamical equilibrium. Since the temperature measurement of the pyrometer is sensitive to processes such as oxide-scale formation at high temperatures, T_γ obtained by DSC was used for correcting the temperature measurement during the in-situ experiment. To this end, all temperature

values acquired by means of the pyrometer were shifted by 30°C towards higher temperatures.

For azimuthal integration of the acquired diffraction patterns the software fit2D[13] was used. Rietveld analysis was performed with the commercial software package TOPAS by Brucker AXS, Madison, USA. The areas of diffraction peaks were calculated by a self-developed software tool. Individual peaks of all phases were fitted with a Gaussian function and multiplied by a weighting factor in order to obtain phase fractions by the intensity ratio method. The weighting factors were derived from the results obtained by Rietveld analysis. More information regarding the investigation of γ-TiAl based alloys by means of synchrotron radiation is provided in references.[10][14][15]

For the prediction of the constituent phases and related transition temperatures, thermodynamic equilibrium calculations were performed using the software ThermoCalc® [16] employing a commercially available TiAl database.[7] Details regarding modelling can be found in the reviews of Ansara [17] and Saunders and Miodownik [18]. For comparison, a section through the Ti-Al-Mo ternary phase diagram for a constant Al concentration of 44% was constructed from experimental data published in the literature.[19-22]

Results and Discussion

Figure 1 shows the microstructure of the two investigated alloys in the as-HIPed condition. The microstructure of the Mo leaner alloy 3M, displayed in Figure 1a, consists of lamellar (γ + α_2)-colonies. The β_o-phase is located mainly along colony boundaries, only a small volume fraction is present within the colonies. Additionally, the existence of globular γ-grains can be detected. EDS analysis has provided clear evidence that the β/β_o-phase is enriched in Mo compared to the other phases. From this observation, it is concluded that the β-stabilizing elements have segregated to β/α-interface boundaries during the $\beta \rightarrow \alpha$ reaction, which took place after solidification via the β-phase as well as during the HIP process.

Alloy 7M (Figure 1b) shows former β-grains which are intersected by elongated γ-phase grains, which were formed during the solid state phase transformations following solidification. Additionally, small single α_2-grains are visible in the micrograph. The β_o phase fraction of alloy 7M at room temperature (Figure 1b) is significantly higher than that of alloy 3M (Figure 1a). Concerning the evolution of the microstructure during solidification, HIPing, short, and long-term ageing treatments further investigations are underway and will be published in a forthcoming paper.[23]

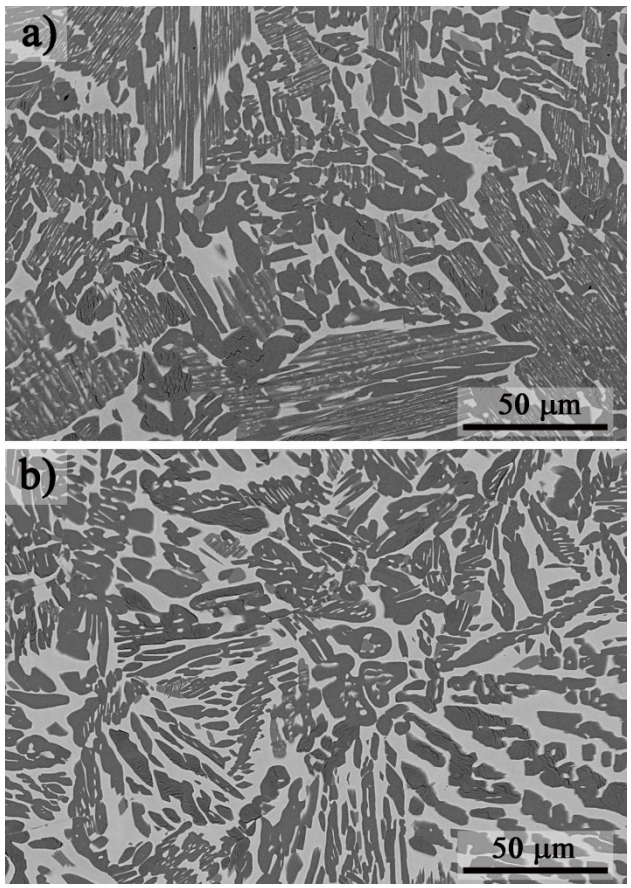

Figure 1: Microstructure of the cast alloy variants after HIPing at 200 MPa and 1200°C for 4 h and subsequent furnace cooling to room temperature: a) Ti-44Al-3Mo (alloy 3M) and b) Ti-44Al-7Mo (alloy 7M). SEM images taken in BSE mode, i.e., γ-TiAl appears dark, α_2-Ti_3Al light-grey and the β_o-phase shows the brightest contrast. In a) all three phases are clearly visible, whereas in b) α_2 is present only in small amounts and β_o and γ-phase are the main constituents.

A section of the phase diagram of the ternary Ti-Al-Mo system was calculated by the CALPHAD method for a constant Al content of 44 at% and Mo contents in the range of 0-10 at% (**Figure 2**). For this calculation, a commercial Ti-Al database [7] was employed. The Mo contents of the investigated alloys 3M and 7M are indicated by vertical lines. From Figure 2 it is evident that both alloys solidify via the β-phase.

For alloy 3M, the following solidification pathway is expected: $L \rightarrow L + \beta \rightarrow \beta \rightarrow \alpha + \beta \rightarrow \alpha + \beta + \gamma \rightarrow \alpha_2 + \beta + \gamma$, where the transition $\alpha + \beta + \gamma \rightarrow \alpha_2 + \beta + \gamma$ occurs at the eutectoid temperature. Alloy 7M solidifies and transforms according to $L \rightarrow L + \beta \rightarrow \beta \rightarrow \beta + \gamma \rightarrow \alpha_2 + \beta + \gamma$. Note that the calculation indicates no order/disorder temperature for the $\beta_o \leftrightarrow \beta$ reaction. **Figure 3** shows a section of the Ti-Al-Mo ternary phase diagram for a

constant Al concentration of 44% which was derived from experimental data taken from.[19-22]

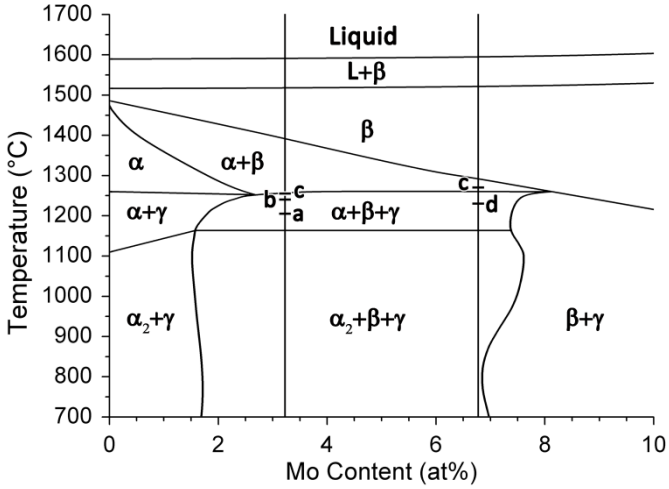

Figure 2: Section of the phase diagram Ti-44Al-(0-10)Mo calculated with the CALPHAD method. The alloys Ti-44Al-3Mo (alloy 3M) and Ti-44Al-7Mo (alloy 7M) investigated in this study are indicated by vertical lines. The transition temperatures determined by in-situ HEXRD are indicated by horizontal marks and letters: letter a indicates the eutectoid temperature, b the $\beta_o \rightarrow \beta$ disordering temperature and c the γ dissolution temperature. The letter d indicates the onset of α-phase formation upon heating of alloy 7M.

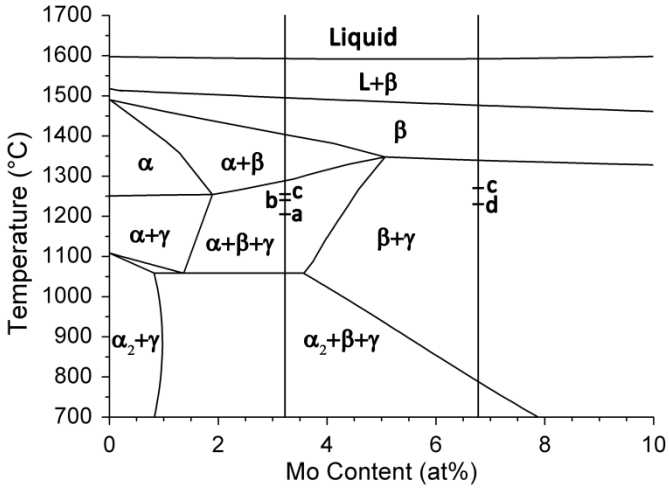

Figure 3: Section of the ternary Ti-Al-Mo phase diagram for an Al-content of 44% established from literature data.[19-22] The investigated alloys with the nominal composition Ti-44Al-3Mo (alloy 3M) and Ti-44Al-7Mo (7M) are indicated by vertical lines. Transition temperatures determined by HEXRD are indicated by horizontal marks and letters: letter a indicates the eutectoid temperature, b the $\beta_o \rightarrow \beta$ disordering temperature and c the γ dissolution temperature. The letter d indicates the onset of α-phase formation upon heating of alloy 7M.

Similar to Figure 2, no distinction between ordered and disordered β-phase is made. On one hand, the solidification sequence of alloy 3M is identical to the one found in the thermodynamic calculation. On the other hand, however, alloy 3M and 7M exhibit a similar solidification pathway in the phase diagram derived from literature data, which is in stark contrast to the results of the thermodynamic calculation.

A comparison of Figure 2 and Figure 3 reveals significant differences between the two phase diagrams. A very pronounced deviation exists for the eutectoid temperature where the calculation suggests a value of 1060°C, whereas the eutectoid reaction is suggested to occur at 1165°C by the phase diagram derived from experimental data. However, it should be noted that previous thermodynamic calculations of transition temperatures for other highly β-stabilized TiAl alloys showed a strong deviation from experimental data, especially with respect to the eutectoid temperature.[8][9] Secondly, in the experimental phase diagram (Figure 3), the point in which the single β-phase field meets with the three other phase-field regions is shifted to a lower temperature and to a significantly higher Mo concentration. For alloy 7M, α/α_2-phase is present below 1295°C according to Figure 3, whereas α_2-phase is predicted to occur only below 790°C by the thermodynamic calculation (Figure 2). For alloy 7M, the absence of α/α_2-phase in the thermodynamic simulation at elevated temperatures precludes the occurrence of the eutectoid reaction, whereas it is predicted to take place at 1160°C by the phase diagram based on literature data. Furthermore, the predictions for the γ dissolution temperature of the two phase diagrams differ significantly. All transformation temperatures derived from the two phase diagrams and experimental data are summarized in **Table 1**.

In **Figure 4** the phase evolution as determined by in-situ HEXRD experiments is shown for alloy 3M and 7M. The results of the Rietveld analyses are represented by the larger, filled symbols in Figures 4a and b.

	Alloy 3M			Alloy 7M		
	calculated (Figure 2)	literature data (Figure 3)	experimentally determined	calculated (Figure 2)	literature data (Figure 3)	experimentally determined
T_{eu} (°C)	1058	1160	1205	-	1160	-
T_{γ} (°C)	1289	1257	1255	1339	1260	1271

Table 1. Transformation temperatures for alloys 3M and 7M as derived from different methods. For alloy 7M the determination of T_{eu} from the calculated phase diagram is not possible since no $\alpha_2 \rightarrow \alpha$ transformation is predicted to occur. No eutectoid temperature was determined from diffraction data for alloy 7M since the intensity of the corresponding superstructure peak was too small.

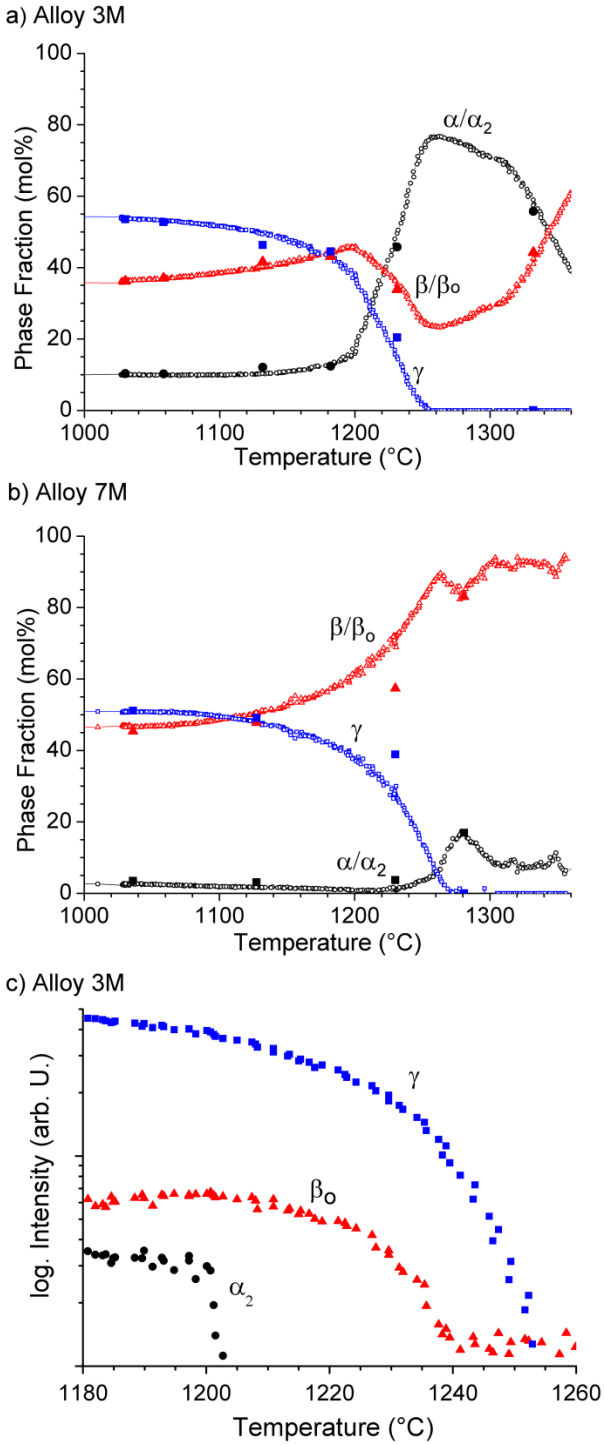

Figure 4: Phase evolution of a) Ti-44Al-3Mo and b) Ti-44Al-7Mo as derived from X-ray diffraction measurements. Circles represent the α-phase, whereas triangles and squares correspond to the β and γ-phase, respectively. Filled symbols indicate results obtained from Rietveld analysis, open ones were derived from peak area evaluation. Diagram c) shows the $\alpha_2 \rightarrow \alpha$ and $\beta_o \rightarrow \beta$ transition temperatures as well as the γ dissolution temperature $\gamma \rightarrow 0$ for alloy Ti-44Al-3Mo.

With the exception of the fits performed at 1230°C, good accordance between Rietveld and peak area evaluation is observed. The deviation at 1230°C can be attributed to the error introduced by the proximity of the diminishing γ-111 peak to the increasing β-011 peak.

At temperatures below 1200°C, alloy 3M with 3.23% Mo shows substantial amounts of α/α_2 phase (Figure 4a), whereas only an insignificant fraction is observed for alloy 7M exhibiting a Mo content of 6.78% (Figure 4b). This observation is consistent with the phase diagram shown in Figure 3 which predicts the occurrence of small amounts of α/α_2 at low temperatures. It must, however, be noted that after HIPing the material is not in equilibrium conditions. Thus, at low temperatures, where diffusion processes are sluggish, the measured phase fractions may not correspond to the equilibrium conditions that are reflected by the phase diagram. Under these conditions, phases might be observed that are thermodynamically unstable and only present because of the slow kinetics of phase transformation or dissolution processes. Due to this reason, especially at low temperatures, Figures 4a and b rather show trends which describe the materials behaviour in conditions present during technical processes than in thermodynamic equilibrium.

At temperatures above 1200°C the α/α_2-phase fraction increases for alloy 3M, whereas for alloy 7M α-phase starts to form at 1230°C. After reaching a maximum, the α-phase fraction decreases in both alloys. Qualitatively, this behaviour is in accordance with the phase diagram shown in Figure 3. In contrast to this, both alloys exhibit a continuous decrease in γ-phase fraction during heating. Values for the γ dissolution, i.e. T_γ, are given in Table 1. Alloy 7M exhibits a β/β_o-phase content that continuously increases until a temperature of 1263°C is attained. After a small drop, the β/β_o-phase fraction continues to increase. In case of alloy 3M, the β/β_o phase fraction increases slightly before it starts to decrease at 1200°C. After reaching a minimum of ~23 mol% at 1260°C, the β/β_o-phase fraction increases again.

Comparison of the experimentally determined phase transition temperatures of alloy 3M (Figure 4a) with both phase diagrams reveals that the eutectoid temperature determined by HEXRD (T_{eu}=1205°C) is significantly higher than that predicted by the calculated phase diagram (T_{eu}=1058°C) (Figure 2). The eutectoid temperature in the phase diagram derived from experimental results (T_{eu}=1160°C) shows a smaller but still substantial deviation from the experimentally determined value (Figure 3).

The temperatures where the γ-phase dissolves upon heating, as obtained from the calculated phase diagram, are 1289°C and 1339°C for alloys 3M and 7M, respectively. Corresponding values from Figure 3 are 1257°C for alloy 3M and 1260°C for alloy 7M. Comparison of these values with the experimentally determined ones (3M: 1255°C; 7M: 1271°C) shows that only small deviations exist between Figure 3 and the experimental data, whereas the differences to the calculated phase diagram are considerable. It has to be

borne in mind that the transformation temperatures of TiAl alloys are strongly dependent on the Al content. Especially the γ dissolution temperature increases strongly with increasing Al content, whereas T_{eu} shows a weaker dependency [5]. Since the actual Al content of alloy 3M (44.58%) is slightly higher than the Al content for which the phase diagrams were compiled, the transformation temperatures indicated in the phase diagrams are systematically too low. It should be pointed out, however, that these deviations are negligible compared to the ones that were found to exist between the experimental results and the two phase diagrams. From Figures 4a and b it can be concluded that the phase diagram depicted in Figure 3 corresponds better to the results obtained by *in-situ* HEXRD.

Additionally, the order/disorder temperatures can be derived from Figure 4c. Here, the intensity of the α_2-011 and β_o-001 reflections as well as the intensity of the γ-011/110 double peak are displayed for the Mo-leaner alloy 3M. Vanishing of these peaks corresponds to the loss of order in the α_2 and β_o phase or the dissolution of γ-phase, respectively. For alloy 3M these temperatures were determined to be 1205°C for the eutectoid reaction $\alpha_2 \rightarrow \alpha$, 1240°C for $\beta_o \rightarrow \beta$, and 1255°C for $\gamma \rightarrow 0$. Compared to data determined on a Ti-43Al-4Nb-1Mo alloy, the $\alpha_2 \rightarrow \alpha$ temperature is shifted to higher temperatures, whereas T_γ is similar.[24] For the $\beta_o \rightarrow \beta$ reaction, only a small shift to higher temperatures was observed.[25]

In a previous study [24] it was shown that the $\alpha_2 \rightarrow \alpha$ and the $\beta_o \rightarrow \beta$ disordering temperatures are rather insensitive to the heating rate applied, whereas the γ dissolution temperature shows a pronounced dependency. However, the ambiguities introduced by this effect are significantly smaller than the differences between the HEXRD data and the phase diagrams shown in Figures 2 and 3. Additionally, at high temperatures α-phase might be stabilized in surface-near regions due to the evaporation of Al, which in turn could lead to artefacts when evaluating phase fractions from diffraction experiments. This possibility, however, was precluded by metallographic examination of the specimen after the experiment.

Thus, it can be concluded that in the case of the investigated Ti-Al-Mo alloys, the quality of the phase diagrams calculated by CALPHAD on the basis of the available database is not yet sufficient for a correct prediction of the prevailing phase fractions.

Conclusions

Sections of the Ti-44Al-(0-10)Mo ternary phase diagram were derived from thermodynamic calculations as well as from literature data. The obtained phase diagrams show significant differences concerning the extension of phase field regions as well as phase transition temperatures. For Mo concentrations <5% the main difference is observed between the position of the phase transition temperatures, whereas for Mo concentrations >5% additional differences in the extension of the phase regions at elevated temperatures

occur. Here, the phase diagram established from literature data predicts the appearance of α-phase, while the calculated one does not. In order to validate the phase transition temperatures of the phase diagrams, *in-situ* HEXRD experiments have been conducted on two alloys with a nominal composition of Ti-44Al-3Mo and Ti-44Al-7Mo. The experimentally determined transformation temperatures, i.e. the eutectoid temperature and the γ dissolution temperature, deviate from the temperatures suggested by the two quasi-binary phase diagrams. From this study it is concluded that the phase diagram derived from literature fits better to the experimental data than the calculated one. Nonetheless, additional investigations are required to describe the transition temperatures and phase fractions of Ti-44Al-(0-10)Mo alloys more accurately. This is especially important for temperatures where phase transformations occur slowly and where heating experiments reflect conditions that are far from thermodynamic equilibrium.

References

[1] Y.-W. Kim, D. Morris, R. Yang, C. Leyens, *Structural Aluminides for Elevated Temperature Applications*, Tms, Warrendale **2008**.

[2] T. Schmoelzer, S. Mayer, F. Haupt, G.A. Zickler, C. Sailer, L. Lottermoser, V. Güther, K.-D. Liss, H. Clemens, in *PRICM 7 Conference Proceedings*, Transtech Publishing **2010**.

[3] Y.-W. Kim, in *Structural Aluminides for Elevated Temperature Applications*, Tms, Warrendale **2008**, 215.

[4] R. Kainuma, Y. Fujita, H. Mitsui, I. Ohnuma, K. Ishida, *Intermetallics* **2000**, *8*, 855-867.

[5] H. Clemens, W. Wallgram, S. Kremmer, V. Güther, A. Otto, A. Bartels, *Advanced Engineering Materials* **2008**, *10*.

[6] F.-S. Sun, C.-X. Cao, S.-E. Kim, Y.-T. Lee, M.-G. Yan, *Metallurgical and Materials Transactions A: Physical Metallurgy and Materials Science* **2001**, *32*, 1573-1589.

[7] N. Saunders, in *Gamma Titanium Aluminides*, TMS, Warrendale, PA **1999**, 183.

[8] H.F. Chladil, H. Clemens, H. Leitner, A. Bartels, R. Gerling, F.-P. Schimansky, S. Kremmer, *Intermetallics* **2006**, *14*, 1194-1198.

[9] H.F. Chladil, H. Clemens, G.A. Zickler, M. Takeyama, E. Kozeschnik, A. Bartels, T. Buslaps, R. Gerling, S. Kremmer, L. Yeoh, K-D. Liss, *International Journal of Materials Research* **2007**, *98*, 1131-1137.

[10] K.-D. Liss, A. Bartels, A. Schreyer, H. Clemens, *Textures and Microstructures* **2003**, *35*, 219-252.

[11] T. Lippmann, L. Lottemoser, F. Beckmann, R. Martins, T. Dose, R. Kirchhof, A. Schreyer, in *Hasylab Annual Report*, Hasylab/DESY, Hamburg **2007**, 113.

[12] W. Reimers, A. Pyzalla, A. Schreyer, H. Clemens, *Diffraction Methods in Engineering Materials Science*, Wiley-VCH, Weinheim, Germany **2008**.

[13] A.P. Hammersley, S.O. Svensson, M. Hanfland, A.N. Fitch, D. Häusermann, *High Pressure Research* **1996**, *14*, 235-248.

[14] K.-D. Liss, A. Bartels, H. Clemens, S. Bystrzanowski, A. Stark, T. Buslaps, F-P. Schimansky, R. Gerling, C. Scheu, A. Schreyer, *Acta Materialia* **2006**, *54*, 3721-3735.

[15] T. Novoselova, S. Malinov, W. Sha, A. Zhecheva, *Materials Science and Engineering A* **2004**, *371*, 103-112.

[16] B. Sundman, B. Jansson, J. Andersson, *Calphad* **1985**, *9*, 153-190.

[17] I. Ansara, *Int Met Rev* **1979**, *24*, 20-53.

[18] N. Saunders, P. Miodownik, *CALPHAD - A Comprehensive Guide*, Elsevier Science, New York, USA **1998**.

[19] T. Hamajima, G. Luetjering, S. Weissmann, in *Red Books, Vol. XVIII*, **1972**.

[20] R. Hansen, R. Aravamudham, *Metallkunde* **1970**, 115.

[21] A.K. Singh, D. Banerjee, *Metallurgical and Materials Transactions A: Physical Metallurgy and Materials Science* **1997**, *28*, 1745-1753.

[22] G. Czi-Min, E. Pylaeva, in *Red Books, Vol IX*, **1963**.

[23] S. Mayer, C. Sailer, T. Schmoelzer, H. Clemens, *International Journal of Materials Research* **2010**, *in preparation*.

[24] T. Schmoelzer, K-D. Liss, G.A. Zickler, I.J. Watson, L.M. Droessler, W. Wallgram, T. Buslaps, A.J. Studer, H. Clemens, *Intermetallics* **2010**, *18*, 1544.

[25] I.J. Watson, K-D. Liss, H. Clemens, W. Wallgram, T. Schmoelzer, T.C. Hansen, M. Reid, *Advanced Engineering Materials* **2009**, *11*, 932-937.

Contents lists available at ScienceDirect

Intermetallics

journal homepage: www.elsevier.com/locate/intermet

Appendix C:
Phase Fractions, Transition and Ordering Temperatures in TiAl-Nb-Mo Alloys: An In and Ex-Situ Study

T. Schmoelzer, K.-D. Liss, G.A. Zickler, I.J. Watson, L.M. Droessler, W. Wallgram, T. Buslaps, A. Studer and H. Clemens

Intermetallics 18 (8), 2010, pp. 1544-1552.

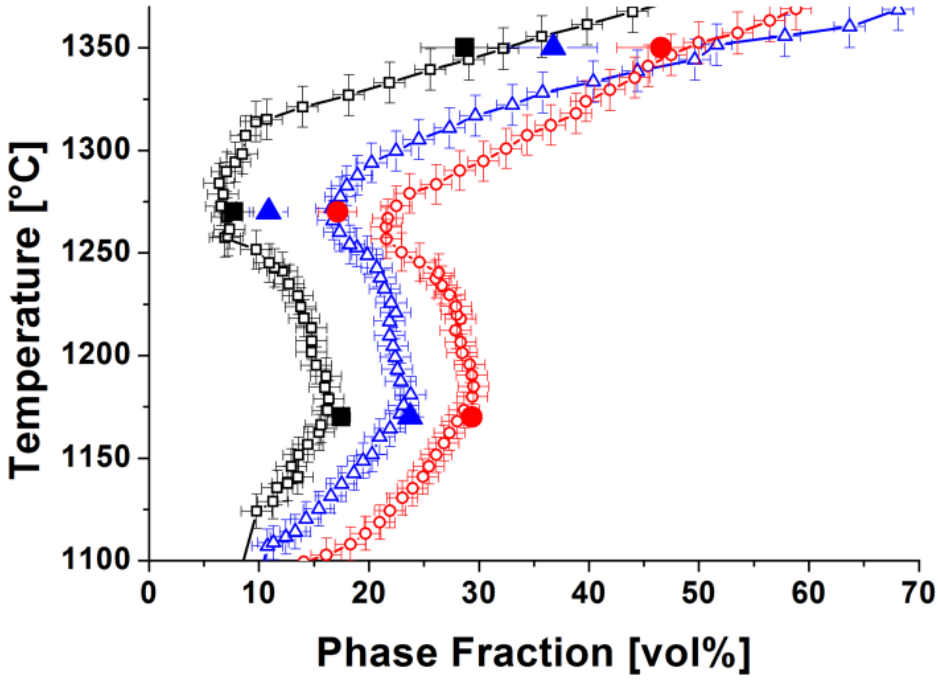

Phase fractions, transition and ordering temperatures in TiAl-Nb-Mo alloys: an in- and ex-situ study.

Thomas Schmoelzer[a], Klaus-Dieter Liss[b], Gerald A. Zickler[c], Ian J. Watson[b], Laura M. Droessler[a], Wilfried Wallgram[d], Thomas Buslaps[e], Andrew Studer[b], Helmut Clemens[a]

[a] Department Physical Metallurgy and Materials Testing, University of Leoben, Franz-Josef-Straße 18, A-8700 Leoben, Austria

[b] Australian Nuclear Science and Technology Organisation, PMB 1, Menai, NSW 2234, Australia

[c] Christian Doppler Laboratory for Early Stages of Precipitation, Department Physical Metallurgy and Materials Testing, University of Leoben, Franz-Josef-Straße 18, A-8700 Leoben, Austria

[d] Böhler Schmiedetechnik GmbH&Co KG, Mariazellerstraße 25, A-8605 Kapfenberg, Austria

[e] European Synchrotron Radiation Facility (ESRF), Polygone Scientifique Louis Néel, 6 rue Jules Horowitz, F-38000 Grenoble, France

Abstract

Intermetallic γ-TiAl based alloys of the TNM™ alloy family attain their excellent processing characteristics by a high β-phase content present at hot-working temperatures. Subsequent to hot-working the β-phase content is decreased by a heat treatment step performed at temperatures where the β-phase fraction exhibits a minimum. In this study, in- and ex-situ experiments were conducted on three alloys with different contents of β/β_0 stabilizing elements. The course of phase fractions as a function of temperature as well as phase transition temperatures were determined by means of in-situ high-energy X-ray diffraction experiments. Additionally, dynamic scanning calorimetry investigations were performed to obtain complementary data on the transition temperatures. Quantitative metallography was conducted on heat treated and quenched specimens to acquire additional information on the dependence of the phase fractions on temperature. By neutron diffraction experiments the ordering temperatures of the constituent phases were determined. It was shown that the experiments yielded consistent results which differ significantly from ThermoCalc simulations for which a commercial TiAl database was used. The differences between the experimental results and the thermodynamic predictions are discussed.

Keywords
Titanium aluminides (based on TiAl), alloy design, order/disorder transformations, phase transformation, heat treatment, diffraction;

1 Introduction

Intermetallic γ-TiAl based alloys are believed to have great potential in high temperature applications, mainly due to their high specific tensile and creep strength at elevated temperatures [1-3]. One of the reasons why this material class has not found widespread application yet are the difficulties associated with its processing [4]. Conventional high Nb bearing γ-TiAl alloys, which show only a small volume fraction of β-phase at hot-working temperature [5], can only be forged under isothermal conditions, which is not economically feasible for most applications [6]. Therefore, the development of alloys that can be processed by near conventional forging operations is an important step towards the mass production of TiAl parts.

So-called TNM™ alloys are among the most promising candidates to meet this requirement. This name is derived from Nb and Mo which are the decisive alloying elements. The overall composition of these alloys is in the range of Ti - (42-45) Al - (3-5) Nb - (0.1-2) Mo - (0.1-0.2) B (in at%) [4]. It has been proven that good processing characteristics are achieved by high β-phase contents at hot-working temperatures [4, 6-7]. The presence of the disordered bcc β-phase is beneficial to the deformation behaviour because dislocation motion as well as dynamic recrystallization is easily facilitated in this phase [8-10]. At service temperature (600-750 °C) the β-phase shows an ordered B2-structure, which is termed β_0 in the following. To avoid the adverse effect of high β_0-phase contents on creep behaviour and room-temperature ductility [11-13], efforts were made to design alloys in a way that allows to minimize the remaining β_0-phase fraction by special two-step heat treatments after forging [4, 7, 14].

One requirement for the realization of this approach is the existence of low equilibrium β/β_0-phase fractions at temperatures high enough to attain equilibrium conditions rather rapidly. The first step of the heat treatment is performed to reduce the β/β_0-phase fraction to the desired level. After the second heat treatment step, which is conducted well below the eutectoid temperature, the microstructure consists of three prominent phases: (a) γ-TiAl exhibiting an ordered tetragonal $L1_0$-structure, (b) α_2-Ti_3Al showing a $D0_{19}$ structure which disorders at the eutectoid temperature to an unordered hcp-structure and (c) the β_0-phase with B2 structure which disorders at elevated temperatures to bcc β-phase. For details concerning the alloy design strategy, hot working behaviour, heat treatments, and mechanical properties the reader is referred to [4, 7, 12, 15-16].

To design an alloy that exhibits the above described behaviour, thermodynamic calculations were performed for alloys containing different amounts of the β/β_0-stabilizing elements Mo and Nb [4]. This study was conducted by employing the CALPHAD (CALculation of PHAse Diagrams) method, using a commercially available database [17]. The results of this investigation are summarized in Fig. 1. Clemens et al. [12] demonstrated that all alloy variants solidify via the β-phase. From comparison of the evolution of phase fractions in the alloys termed A, B, and C it is obvious that Mo is a stronger β/β_0 stabilizer than Nb, which is in agreement with the results of other studies [18-19].

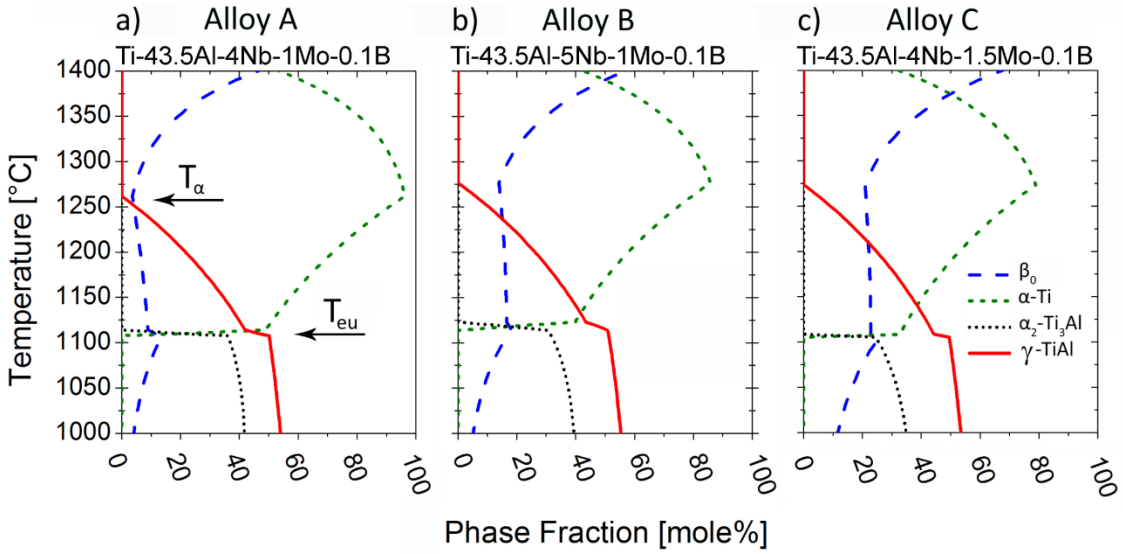

Fig. 1: Calculated phase fractions as a function of temperature for three alloys, termed A, B, and C, exhibiting different amounts of β/β_0 stabilizing alloying elements and 450 mass ppm O. The simulations were performed with the ThermoCalc software using a commercially available TiAl database [17]. The plotted temperature range corresponds to the range investigated by in- and ex-situ methods. T_{eu} and T_α denote the eutectoid and the α-transus temperature, respectively. At T_{eu} the $\alpha_2 \rightarrow \alpha$ disordering reaction takes place, whereas at T_α the ordered γ-phase disappears. It should be noted, that for all three alloys the predicted disordering temperature of the β_0-phase is above 1400 °C.

Furthermore, for all three alloys the thermodynamic calculations show a local minimum of the β_0-phase mole fraction at around 1275 °C. Above this temperature the fraction of β_0-phase strongly increases with temperature. However, at the temperature where the minimum in β_0-phase appears, Ti-43.5Al-4Nb-1Mo-0.1B (Alloy A) shows the smallest fraction of β_0-phase. By increasing the amount of Nb or Mo by 1 at% or 0.5 at%, respectively, the mole fraction of the β_0-phase in its minimum is considerably increased. Below 1275 °C the β_0-fraction slightly increases with decreasing temperature (Fig. 1a; alloy

A) or shows an approximately constant value (Figs. 1b and c; alloys B and C). At temperatures lower than the eutectoid temperature (~ 1115 °C) the β_0-phase fraction decreases with decreasing temperature for all three alloys. From the phase predictions displayed in Fig. 1 it is obvious that none of the three alloys exhibit a single phase region at temperatures below 1400 °C.

Since the thermodynamic database [17] used for the ThermoCalc calculations is not well suited for describing the behaviour of highly alloyed TiAl-systems [5, 20-21], doubt has been cast on the reliability of the results obtained by the thermodynamic simulations shown in Fig. 1. Furthermore, the simulation predicted that the ordered β_0-phase is stable up to temperatures as high as 1420 °C [16]. In contrast to that, non-isothermal hot-forging tests conducted on industrial-scale equipment showed that alloys with comparable composition exhibit good deformation behaviour at temperatures well below 1400 °C [4, 7]. Since ordered β_0 shows higher deformation resistance than disordered β, the validity of the predicted ordering temperature was questioned [22-23].

In the light of these findings, it has been established that thermodynamic predictions as shown in Fig. 1 yield trends rather than accurate values of the phase fractions and transition temperatures [16, 21]. Recent investigations indicate that the results of thermodynamic calculations reflect the materials behaviour observed in short-time annealing experiments [21]. Evidence for this assertion was obtained from differential scanning calorimetry (DSC) investigations and long-term annealing experiments which have revealed the existence of an α-single-phase field that was not predicted by the ThermoCalc simulations shown in Fig. 1 and was not observed at moderate annealing times. However, understanding the phase equilibria and transition temperatures of the investigated alloy system is a prerequisite for performing hot-working operations and for defining appropriate heat treatment parameters.

A thorough knowledge of the constituent phase fractions and their dependence on temperature and time are, therefore, crucial for the present and further development of the investigated alloys. In this study, a number of complementary experiments were conducted to investigate how accurate the predictions of the thermodynamic calculations shown in Fig. 1 are. The dependence of the phase fractions on temperature was determined by means of in- and ex-situ methods. During continuous heating the evolution of phase fractions was monitored by in-situ high energy synchrotron X-ray diffraction (HEXRD). Applications and techniques concerning HEXRD experiments can be found in [24-27]. DSC experiments were carried out to verify the transformation temperatures obtained by HEXRD. Additionally, annealing experiments at elevated temperatures followed by rapid air cooling were conducted to analyse the phase fractions by a metallographic approach. Finally, the ordering temperatures of the constituting phases were determined by means of in-situ neutron diffraction experiments.

2 Material and experimental

In the present study, three different alloys were investigated which are termed A (Ti-43.5Al-4Nb-1Mo-0.1B), B (Ti-43.5Al-5Nb-1Mo-0.1B) and C (Ti-43.5Al-4Nb-1.5Mo-0.1B). Note that all chemical compositions are stated in atomic percent unless otherwise indicated. All three alloys exhibit an Al content of 43.5 at%, but different concentrations of the β/β_0 stabilizing elements Nb and Mo. Buttons with a mass of 150 g were melted in a laboratory arc-melting furnace on a water-cooled copper plate under Ar atmosphere. As starting materials, high-purity metals and Mo-Al, Al-B and Nb-Ti-Al master alloys were used [28]. Sufficient chemical homogeneity was ensured by re-melting the buttons twice. The nominal chemical composition of the alloys and the results of the chemical analyses are summarized in Tab. 1. For all alloys, the total amount of interstitial impurities (O, N, C, H) was smaller than 1000 wt.-ppm.

	Alloy A	Alloy B	Alloy C
Ti	51.4 (51.77)	51.4 (50.54)	51.4 (51.04)
Al	43.5 (43.27)	43.5 (43.38)	43.5 (43.37)
Nb	4 (3.84)	5 (4.93)	4 (3.97)
Mo	1 (1.01)	1 (1.01)	1.5 (1.51)
B	0.1 (0.11)	0.1 (0.11)	0.1 (0.12)

Tab. 1: Nominal and experimentally determined composition of the alloys A, B, and C. The results of X-ray fluorescence spectroscopy are given in parenthesis. All values in atomic percent.

The microstructure of the three variants after solidification and after subsequent heat treatments was characterized by means of a Zeiss Evo 50 scanning electron microscope (SEM). All images were acquired in back-scattered electron (BSE) mode at an acceleration voltage of 20 kV. Details concerning the metallographic sample preparation are given in [29]. To be able to determine the β/β_0-phase content present at different temperatures, samples of the three alloys with dimensions of 10×10×10 mm^3 were heat-treated at 900 °C and 1000 °C for 6 h and at 1170, 1270 and 1350 °C for 1 h. Subsequently, the specimens were air-cooled, and metallographically examined. Image analysis with regard to the β/β_0-phase content was performed with the commercially available software package Analysis by Olympus Soft Imaging Solutions (Münster, Germany).

DSC experiments were conducted to investigate the eutectoid temperature (T_{eu}, $\alpha_2 \rightarrow \alpha$) and the α-transus temperature (T_α, γ dissolves). Both temperatures were

determined for heating rates of 20 and 40 K/min and then linearly extrapolated to a heating rate of 0 K/min in order to obtain phase transition temperatures for equilibrium conditions [5]. All experiments were carried out in a dynamic Ar atmosphere with a flow rate of 50 ml/min. To account for the influence of the alumina crucibles DSC curves of the empty crucibles were subtracted from the experimentally obtained curves. The experiments were performed with a Setaram Setsys Evolution 24 instrument on specimens with a mass of approximately 40 mg.

In the in-situ HEXRD experiments the phase fractions were determined during continuous heating in an induction furnace. Details on the construction and the performance of the furnace are given in [30]. All specimens were cylinders with a diameter of 4 mm and a length of approximately 10 mm. During the experiments the furnace was flushed with Ar to reduce sample oxidation, the temperature was controlled by two pyrometers. A low temperature pyrometer was used below 650 °C, while a spectro-pyrometer with an accuracy of 0.75 % was utilized for controlling the high temperature range. The specimen was rotated about its vertical axis alternating between +180° and -180° in order to improve grain statistics. Due to technical limitations it was not possible to use a thermocouple for monitoring and validating the pyrometer reading.

All HEXRD experiments were performed at ID15B of the European Synchrotron Radiation Facility (ESRF) in Grenoble, France [16, 25, 31]. To cover the desired range of the scattering vector q a monochromatic beam with a mean energy of 86.78 keV and an energy resolution of $\Delta E/E=10^{-3}$ was used. This energy evaluates to a wavelength λ of 0.1430 Å and a wave number k of 43.94 $Å^{-1}$. The cross-section of the primary beam at the sample position was adjusted to 0.1×0.1 mm^2. During the experiments, the samples were heated to 1100 °C with a rate of 300 K/min, after that a 2 K/min temperature ramp was adjusted up to 1400 °C. This heating rate is a compromise between limited beam-time and insufficient counting statistics due to grain growth effects on one hand and the need to use low heating rates in order to attain phase fractions close to equilibrium conditions on the other hand.

For detecting the diffracted photons, a Thales Pixium 4700 (Thales Group, Neuilly-sur-Seine, France) area detector was used [32]. It features a resolution of 2640x1920 pixels which are 154x154 μm^2 in size. To avoid overexposure of the detector while maintaining sufficient counting statistics, 12 detector images - each of 1 s exposure time - were averaged. Thus a single diffraction image with a cumulative exposure time of 12 s was generated. For data reduction and as a preliminary step for Rietveld analysis, the images were azimuthally averaged, corrected for background scattering and re-binned to a 2Θ scale. This task was performed with the software FIT2D which is described in detail in [33]. The phase fractions present at different temperatures were determined with the commercial software package Topas (Brucker AXS, Madison, WI, USA) which allows diffraction patterns to be analysed using the Rietveld method.

In-situ neutron diffraction experiments were performed to determine the temperature of the $\beta_0 \rightarrow \beta$ disordering reaction. Continuous data acquisition during heating was performed using the high intensity diffractometer WOMBAT installed at the OPAL reactor of the Australian Nuclear Science and Technology Organisation (Australia) [34].

At the two-axes powder diffractometer WOMBAT, a Ge 115 monochromator at 100° takeoff angle was used to obtain neutrons with a mean wavelength of $\lambda = 1.67$ Å, which corresponds to a wave number of $k = 3.77$ Å^{-1}. The instrument hosts a genuine, cylindrical 2D position sensitive detector of 968 × 128 pixels^2 covering 120° in the scattering plane and approximately ±7.82° out of plane [33] [34]. Since no detector scanning is needed, time frames only depend on the counting statistics and here a counting time of 18.2 s per frame has been chosen. For the following data evaluation, the recorded parts of the Debye-Scherrer rings were azimuthally integrated in order to obtain conventional powder diffraction patterns in a range of interest of $q \in [1\ldots7]$ Å^{-1}.

Heating of the specimens was performed in an high-temperature vacuum furnace produced by AS-Scientific (Abingdon, Oxfordshire, U.K.) equipped with Nb heating filaments. The oscillating, radial collimator of WOMBAT was used to discriminate diffraction not coming from the sample position, e.g. radiation scattered by the furnace heating elements and walls [23]. From the end of the top-loading sample stick the Ø 10 mm × 50 mm sample was suspended and the temperature was measured ~15 mm from one of its ends. In the specimen chamber a pressure of less than 1.34×10^{-4} mbar was attained. Two samples have been subjected to the same heating cycle to ensure the reproducibility of the results.

3 X-ray and neutron diffraction

Despite the fact that HEXRD and neutron diffraction experiments are based on the same principle they exhibit some pronounced differences. These stem in part from the limitations that are imposed by the corresponding radiation sources in terms of brilliance and beam size, but also from the different interactions of neutrons and photons with matter. As a first analysis step, the diffraction patterns were calibrated and the scattering angles in 2Θ were converted to positions in reciprocal space which are denoted by the scattering vector q. The length of the scattering vector q is given by

$$q = |\mathrm{q}| = (2k)\sin(\Theta) = (4\pi/\lambda)\sin(\Theta) \quad (1)$$

and is also referred to as 'momentum transfer'.

Neutrons and X-rays have different scattering contrasts, which are described by their scattering lengths b_c and $r_e \cdot f(q)$, respectively. Here b_c denotes the bound coherent neutron scattering length, which is strongly dependent on the kinds of nuclear isotopes present [35-36], r_e is the classical electron radius and $f(q)$ the so called atomic X-ray form factor which scales with the number of electrons in an atom at $q = 0$ and decreases asymptotically to 0

with increasing q values, depending on the electronic charge distribution around the nucleus. In the case of titanium aluminides, HEXRD and neutron diffraction are complementary methods. For X-rays, Ti and Al, with atomic numbers 22 and 13 respectively, both exhibit positive scattering lengths ($(r_e \cdot f)_{Al}$ =3.664 fm, $(r_e \cdot f)_{Ti}$ =6.207 fm). On the other hand for neutrons, Ti and Al have scattering lengths, b_c, that are of almost the same absolute value but have opposite signs: $b_{c,Al}$ = 3.449 fm, $b_{c,Ti}$ = -3.370 fm [35] [35].

For a random solid solution, such as the atomically disordered Ti-Al phases, a virtual atom with its scattering length equal to the weighted average of the scattering lengths of the constituents is used when calculating structure factors (F, see below). While for X-rays the weighted average scattering length is a large positive number, it is close to zero for neutrons:

$$b_{c,TiAl} = b_{c,Ti} + b_{c,Al} = -3.370 \text{ fm} + 3.449 \text{ fm} = 0.079 \text{ fm}. \quad (2)$$

For any crystal, the intensity determining structure factors are the sum of the atomic scattering lengths weighted by an individual phase factor given by the position of the corresponding atom in the unit cell. If the unit cell contains several atoms, the individual atomic scattering lengths directly add up for the main reflections because in this case the phase factors are close to one. This yields high structure factors for X-ray diffraction and small ones for neutron diffraction. For some reflections, the phase factors attain values that are equal but of opposite signs due to the symmetry of the unit cell. For atomically disordered crystals, this results in reflections with zero intensity, e.g. for the 100 reflection of the disordered β-phase $b_{c,1} = b_{c,2}$ and thus $F = (b_{c,1} - b_{c,2}) = 0$. In contrast to that, for an ordered crystal these so-called superstructure peaks might attain finite intensities, since for β_0-100, $b_{c,1} \neq b_{c,2}$ the structure factor attains large absolute values for neutrons:

$$F = b_{c,Al} - b_{c,Ti} = 3.449 \text{ fm} - (-3.370 \text{ fm}) = 6.819 \text{ fm}. \quad (3)$$

If performed for X-rays, this calculation yields rather small structure factors. Thus, for disordered phases present in the Ti-Al system, X-rays produce strong main reflections, whereas almost no intensity is observed in neutron diffraction. In case of ordered phases, weak superstructure reflections appear in addition to the main reflections for X-ray diffraction, while only the strong superstructure reflections are visible for neutrons. Due to this characteristic behaviour, neutron diffraction is an ideal method for investigating order/disorder transitions in the Ti-Al system [23]. Alloying elements such as Nb ($b_{c,Nb}$ = 7.054 fm) and Mo ($b_{c,Mo}$ = 6.715 fm) [35] exhibit large scattering lengths and may therefore alter this behaviour. The sensitivity to order in neutron scattering experiments remains high nonetheless. On the contrary, HEXRD experiments are better suited for determining the overall phase fractions.

Quantitative evaluation of the scattering patterns acquired by HEXRD experiments was carried out by means of the Rietveld method, which allows a whole-pattern fit to be performed and thereby uses all the information contained in the diffraction patterns [37].

4 Results

Figure 2 shows SEM micrographs taken in BSE mode from the arc-melted alloy buttons. The microstructure consists of lamellar γ/α_2-colonies which are separated by the brightly appearing β_0-phase. The microstructural features clearly indicate that solidification proceeded via the β-phase, i.e. $L \rightarrow L + \beta \rightarrow \beta \rightarrow ...$, followed by a multitude of solid-state transformations and reactions as described in [4]. Due to the high cooling rate the γ/α_2-lamellae cannot be resolved at the magnification used. The microstructure is fine grained with an average size of the lamellar colonies in the order of 30 - 60 µm and does not seem to depend on the level of β/β_0-stabilization.

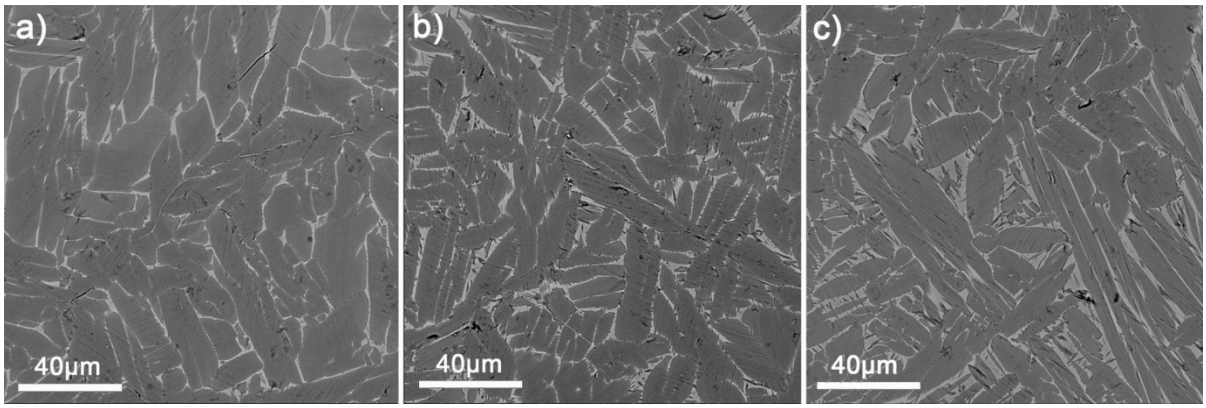

Fig 2: Microstructure of the arc-melted alloy buttons: a) Ti-43.5Al-4Nb-1Mo-0.1B (alloy A), b) Ti-43.5Al-5Nb-1Mo-0.1B (alloy B) and c) Ti-43.5Al-4Nb-1.5Mo-0.1B (alloy C). SEM images were taken in BSE mode, i.e. lamellar γ/α_2-colonies appear grey, γ-grains dark and β_0 exhibits the brightest contrast.q

A close look at the morphology of the β_0-phase evidences the presence of lens-shaped γ-phase grains, which are the product of a $\beta/\beta_0 \rightarrow \gamma$ solid-state transformation bringing the phase fractions closer to equilibrium. While the phase arrangement and grain size of the three investigated alloys are comparable, Fig. 2 reveals that the β_0-phase fraction depends on the content of Nb and Mo. Whereas alloy A (Ti-43.5Al-4Nb-1Mo-0.1B) shows the lowest volume fraction of β_0-phase (Fig. 2a), alloy C (Ti-43.5Al-4Nb-1.5Mo-0.1B) exhibits the highest amount (Fig. 2c). The β_0-phase fraction of alloy B (Ti-43.5Al-5Nb-1Mo-0.1B) lies between alloys A and C (Fig. 2b). It should be noted that the experimentally observed trend is also predicted by the ThermoCalc simulations shown in Fig. 1.

A classic ex-situ approach was used to study the phases prevailing at different temperatures: samples of all three alloys were annealed in the temperature range from 900 to 1350 °C. After a certain annealing time, the samples were air-cooled which occurred with cooling rates sufficiently high for preserving the high temperature microstructure [14].

Figures 3a-c show the microstructure of alloy A after annealing for 1 h at 1170 °C, 1270 °C and 1350 °C, respectively. The microstructure of the sample annealed at 1170 °C is an assembly of lamellar γ/α_2-colonies with an average grain size below 40 µm and a mixture of γ and β_0-grains essentially situated at colony boundaries (Fig. 3a). According to Fig. 1a the annealing treatment at 1170 °C was conducted in the ($\alpha + \beta_0 + \gamma$) phase region.

Fig. 3b shows the microstructure after annealing at 1270 °C for 1 h and subsequent air-cooling. The temperature was selected to be slightly above T_α of the alloy which is close to the β-phase minimum (Fig. 1a). As expected, the γ-phase disappeared and the microstructure at room temperature consists of α_2 and β_0-grains.

Increasing the annealing temperature to 1350 °C leads to higher β/β_0-phase fractions (Fig. 3c) which is consistent with the predictions of the thermodynamical calculations (Fig. 1a). The micrograph obtained at room-temperature evidences the presence of fine-scaled α_2 needles within the β_0 grains. It is presumed that those precipitated during air-cooling. Quantitative analyses of the phase fractions have revealed that the sample annealed at 1270 °C shows the lowest β/β_0-phase content. The β/β_0 volume fraction of the sample heat treated at 1170 °C is slightly higher, whereas the material annealed at 1350 °C exhibits the highest fraction (see below for the specific results for all alloys).

DSC measurements were conducted on the three alloys to determine both T_{eu} and T_α. As described in section 2, two heating rates have been used and the results were linearly extrapolated to 0 K/min in order to achieve equilibrium values for T_{eu} and T_α [5]. The results of the DSC experiments are summarized in Tab. 2.

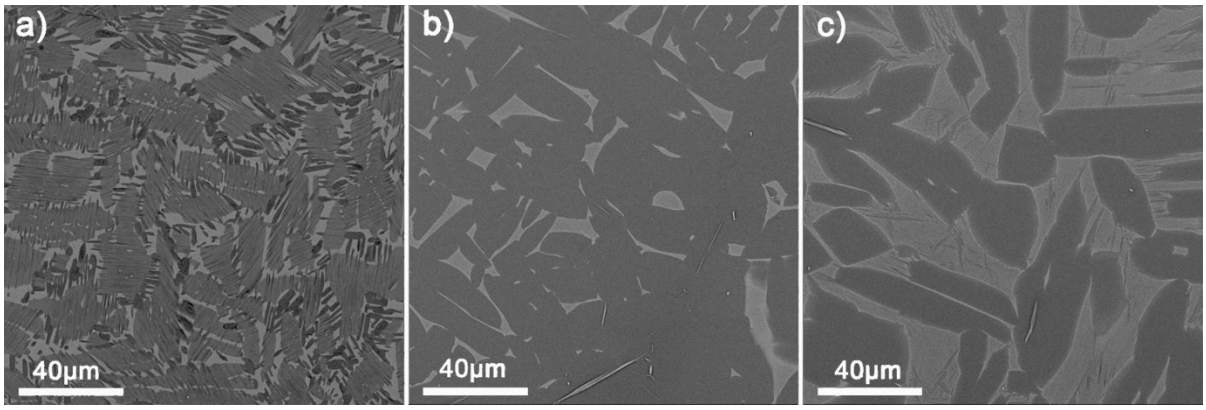

Fig. 3 Microstructure of alloy A (Ti-43.5Al-4Nb-1Mo-0.1B) after annealing at different temperatures for 1 h and subsequent air cooling: a) 1170 °C, annealing conducted in the ($\alpha + \beta + \gamma$) phase field region; b) 1270 °C, annealing conducted in the ($\alpha + \beta$) phase field region, close to the minimum of the β-phase (see Fig. 1a); c) 1350 °C, annealing conducted in the ($\alpha + \beta$) phase field region.

The results obtained from HEXRD experiments, conducted on alloy A, B, and C, are summarized in Fig. 4. Here, the phase fractions of α/α_2, β/β_0 and γ are displayed as a function of temperature. During the continuous heating experiments, the temperature was controlled by means of a high temperature pyrometer. However, the comparison of the eutectoid temperatures derived from HEXRD experiments with those obtained from DSC (Tab. 2) revealed that the temperature indicated by the pyrometer was erroneous.

This is attributed to the formation of an oxide layer on the sample surface during the diffraction experiments. Previous DSC and neutron diffraction studies [23] have shown that T_{eu} hardly depends on the heating rate [5, 12, 23]. Therefore, T_{eu} was chosen as a reference point for correcting the temperature obtained during the HEXRD experiments. This was achieved by calculating the difference between T_{eu} determined by DSC and T_{eu} gained from diffraction data first. In the next step, all temperature values recorded during the HEXRD experiment were corrected by this offset. For determining T_{eu} from diffraction data, the intensity of an α_2 superstructure peak was plotted as a function of temperature. Vanishing of the intensity indicates the loss of order and, therefore, marks T_{eu}.

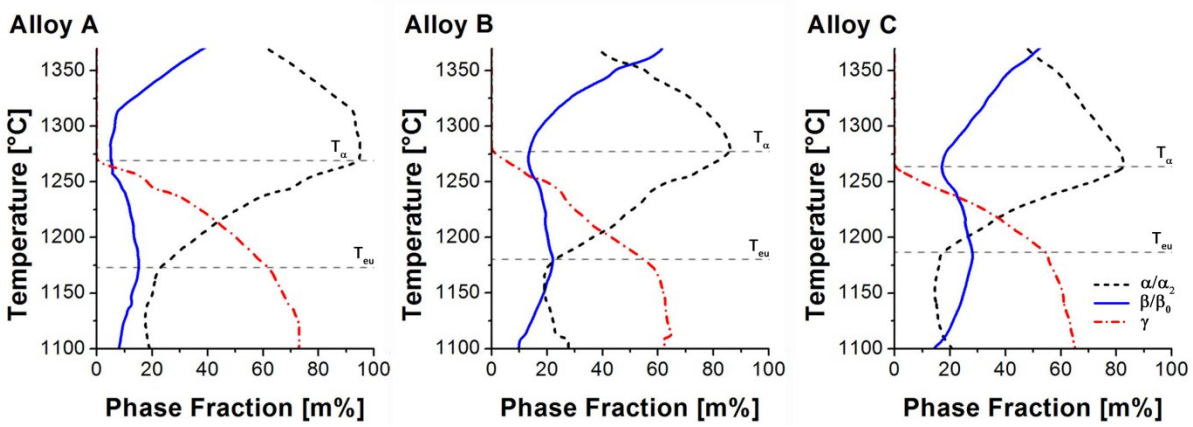

Fig. 4: Phase fractions of α/α_2, β/β_0 and γ as a function of temperature. The phase fractions were evaluated by Rietveld analysis of the corresponding HEXRD patterns. Temperature values were corrected by comparison with DSC measurements, the HEXRD experiments were conducted with a heating rate of 2 K/min.

In Fig. 4 the eutectoid temperature is indicated by a local maximum in the β/β_0 phase fraction and by a sudden change in the slope of the α/α_2 and γ phase fraction curves. A minimum in β/β_0 phase fraction occurs at the α-transus temperature. Accordingly, at this temperature the γ-phase vanishes. For all investigated alloys, the α-transus temperatures evaluated by HEXRD are given in Tab. 2.

Fig. 5 shows the course of the β/β_0-phase fraction as a function of temperature for the three investigated alloys in greater detail. Error bars of the in-situ HEXRD experiments

represent the standard deviation of different Rietveld-fits. For all three alloys a minimum in β/β_0 phase fraction in the range from 1250 °C to 1300 °C can be observed which is in accordance with the results from the thermodynamic calculations shown in Fig. 1. At all temperatures alloy A exhibits the lowest β/β_0-phase content followed by alloy B, and as expected, alloy C shows the highest β/β_0-phase fractions. The solid symbols indicate the results obtained from quantitative metallography conducted on heat treated and air cooled samples as shown in Fig. 3.

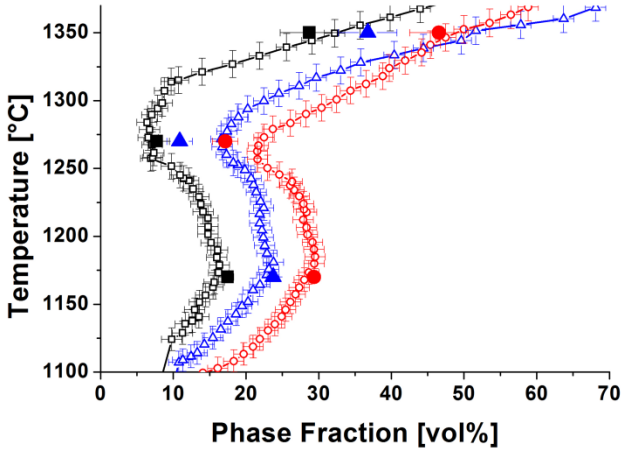

Fig. 5: β/β_0-phase fractions determined by in- and ex-situ methods. The in-situ HEXRD results of alloys A, B and C are indicated by open squares, triangles and circles, respectively. Filled symbols represent the results of quantitative metallography conducted on specimens heat-treated for 1 h at 1170 °C, 1270 °C and 1350 °C, followed by air cooling.

	Alloy A Ti-43.5Al-4Nb-1Mo-0.1B		Alloy B Ti-43.5Al-5Nb-1Mo-0.1B		Alloy C Ti-43.5Al-4Nb-1.5Mo-0.1B	
	DSC	HEXRD	DSC	HEXRD	DSC	HEXRD
T_{eu} [°C]	1173 ± 5	-	1180 ± 5	-	1187 ± 5	-
T_{α} [°C]	1247 ± 5	1267 ± 9.5	1254 ± 5	1262 ± 9.5	1246 ± 5	1277 ± 9.6

Tab. 2: Transformation temperatures T_{eu} and T_{α} as determined from DSC and HEXRD experiments. Since T_{eu} was used as reference point for the temperature correction in the HEXRD experiments, the corresponding values were omitted. HEXRD experiments were conducted with a heating rate of 2 K/min. Error bars were evaluated from the accuracy of the measured temperature and the repeatability of different analysis attempts, whereas the error of the HEXRD measurement was estimated from the accuracy of the pyrometer.

The time evolution of the neutron diffraction patterns obtained during a continuous in-situ temperature ramp on WOMBAT are shown in Fig. 6. Temperature values are indicated by the superimposed graph on the right hand side. It can be seen that reflections of the ordered phases α_2, $\beta_{0,}$ and γ disappear upon heating. At T_{eu} α_2 disorders to α, T_0 marks the loss of order in the β_0-phase and at T_α the γ-phase disappears. Although it is evident from Figs. 4 and 5 that crystalline α and β–phase is still present above T_α, no Bragg reflections are observed due to the peculiar average of the neutron scattering lengths for this material (see section 3). Instead, some diffuse scattering persists peaking at the positions of the superstructure reflections.

For alloy A the experimentally determined intensity values of superstructure peaks are plotted versus temperature in Fig. 7. The plotted intensities were gained from integration of a Gaussian fitted to the corresponding reflection-peak at a certain temperature. All intensities given are background corrected. At a heating rate of 10 K/min, the reflections vanish at 1174 °C (T_{eu}), 1225 °C (T_0) and 1286 °C (T_α) for α_2, β_0, γ, respectively (Tab. 3). After the phase transformation, the peak intensity is close to zero and the algorithm is no longer able to perform the fit. Therefore no intensity values are given after the phase transformation has occurred. A comparison of T_α obtained by different experimental techniques shows that the results differ significantly. The reason for this behavior is that disordering reactions as well as phase transitions require some time to occur while the temperature is constantly increased during continuous heating. Hence, the magnitude of the shift between a transition temperature determined under equilibrium conditions and one that was obtained on heating is a function of the heating rate as well as the kinetics of the phase transition as explained in the next section.

	Alloy A Ti-43.5Al-4Nb-1Mo-0.1B
T_{eu} [°C]	1174
$\beta_0 \rightarrow \beta$ [°C]	1225
T_α [°C]	1286

Tab. 3: Order to disorder transition temperatures of alloy A (Ti-43.5Al-4Nb-1Mo-0.1B) determined by neutron-diffraction. A heating rate of 10 K/min was adjusted in the experiment.

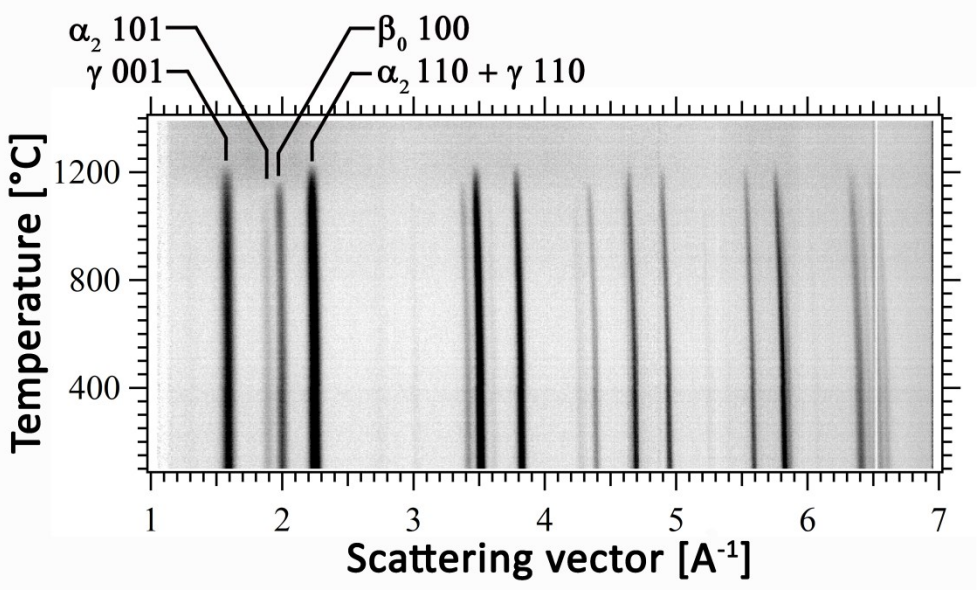

Fig. 6: In-situ neutron diffraction patterns obtained on Ti-43.5Al-4Nb-1Mo-0.1B (alloy A) (in at%) while undergoing a continuous heating ramp of 10 K/min. The intensity is coded in grey scale (black corresponds to high intensities) and stretched in time on the ordinate. The temperature is indicated by the continuous line on the right hand side with readings on the top axis. The reflections at q=1.6-2.3 were used to establish Fig. 7.

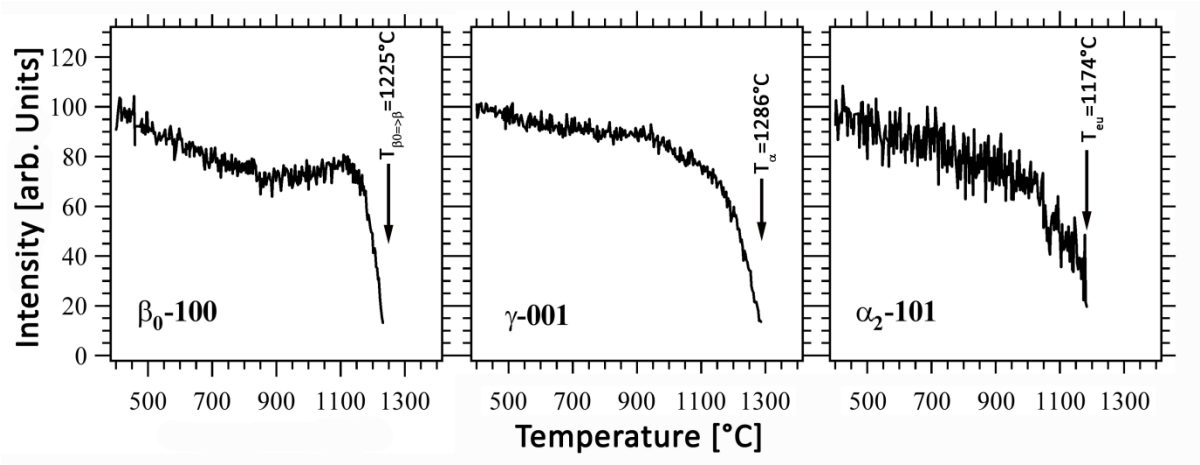

Fig. 7: Intensity evolution of the first three reflections of Fig. 6, normalized to their starting intensity at room temperature. Loss of order in one phase is indicated by a sharp drop in intensity of the corresponding reflection. The intensities do not attain zero values because some background and diffuse scattering persists.

5 Discussion

The main task of this investigation is to evaluate the accuracy of the thermodynamic predictions shown in Fig. 1 [38]. From the DSC results (Tab. 2) it is evident that T_{eu} of the three investigated alloys is significantly higher than the ThermoCalc predictions (Fig. 1). This result is in accordance with the observations reported in [21]. A similar result was found for Ti-45Al-(5-10)Nb alloys published in [5]. The conclusion drawn from these results is that Nb and Mo act not only as β/β_0-stabilizing alloying additions, but also stabilize the ordered α_2-phase. Increasing values for T_{eu} (Tab. 2) as well as increasing β/β_0-phase fractions (Fig. 5) from alloy A to alloy C support this assumption. In principle, the eutectoid temperature can be determined by DSC, HEXRD and neutron diffraction experiments. Since the temperature measurement with a pyrometer was impaired during the HEXRD experiment, the eutectoid temperature determined by DSC was used as a reference point for the correction of the pyrometer reading. HEXRD experiments were conducted at heating rates of 2 K/min, during neutron diffraction a heating rate of 10 K/min was employed.

By thermodynamic calculations T_α was predicted to be 1260 °C for alloy A and 1275 °C for alloys B and C. In the DSC experiments (Tab. 2) slightly lower values for T_α were determined, whereas the results from HEXRD were close to the predicted values (Fig. 4). T_α as determined by neutron diffraction experiments on alloy A was 1286°C (Fig. 7). The observed differences can be explained by the sensitivity of T_α to the applied heating rate. In contrast to that, T_{eu} shows only a weak dependence on heating rate, which is attributed to the different natures of the occurring phase transformations. While at T_{eu} the $\alpha_2 \rightarrow \alpha$ disordering reaction takes place which requires only short-range diffusional jumps, the phase transition at T_α ($\gamma \rightarrow \alpha$) requires a change in crystal structure. This necessitates a collective rearrangement of whole lattice planes by changing their stacking sequence, accompanied by long-range diffusion processes to homogenize the concentration between the disappearing and prevailing phases. Therefore, this phase transition is much slower in terms of transformation kinetics, which in turn explains the higher sensitivity to the heating rate. The observed large difference in rate dependencies of T_{eu} and T_α has also been shown in [39]. As reported in [23] the same effect occurs upon cooling with the only difference being that the temperature shift of T_α is larger.

Whereas the predicted and experimentally observed transition temperatures deviate significantly for T_{eu} and moderately for T_α the experimentally determined course of phase fractions (Fig. 4) is similar to the result of the thermodynamic calculation (Fig. 1). Furthermore, the calculated as well as the experimentally acquired phase fraction diagrams show that an increased content of Nb and Mo shifts the minimum in β/β_0-phase fraction to larger values. The evolution of β/β_0-phase with temperature is important for wrought processing and the design of heat treatments: a high β-phase content is necessary for hot-working [4], but detrimental to the creep strength at service temperature. From Figs. 1 and

4 it is evident that alloy A shows the lowest minimum, thus rendering this specific alloy composition particularly interesting for thermo-mechanical processing and subsequent heat treatments. These heat treatments are conducted to minimize the β/β_0-phase fraction and to adjust a microstructure that possesses balanced mechanical properties. Usually, the heat treatment is performed in a two step fashion, in which the first step is performed close to T_α to reduce the amount of β/β_0-phase while the second step is a stabilization treatment conducted below 1000 °C [4, 7, 14].

In Fig. 5 the β/β_0-phase fraction obtained by HEXRD experiments is compared with data gained from ex-situ investigations. At 1170 °C the β_0-phase fractions obtained by HEXRD are slightly smaller than those from quantitative metallography. This can be explained by the slow transformation behaviour of the β/β_0-phase [21] and the shorter periods of time the material has to reach equilibrium conditions during the HEXRD experiment. At 1270 °C the HEXRD and ex-situ results coincide for alloy A, but not for alloys B and C. One reason for the deviation is that the error in phase fraction determined by quantitative metallography increases with temperature. Especially for the microstructure obtained after annealing at 1350 °C the determination of the β_0-phase content is impaired by the formation of α-needles in β_0-grains which is suspected to occur during air cooling. In addition to that the quality of the HEXRD patterns diminishes with increasing temperature due to grain coarsening which decreases counting statistics. Thus, it is concluded that the observed difference between the in- and ex-situ methods used in this study can be attributed to their limited accuracy as well as to the slow transformation kinetics of the β/β_0-phase.

The deviation observed between the calculated and the experimentally determined phase fraction diagram can be attributed to the insufficient thermodynamic database for alloys with high contents of β/β_0-stabilizing elements [5, 17, 20-21]. Additional complications arise from the sluggish dissolution behaviour of the Nb- and Mo-rich β/β_0-phase. This is emphasized by the fact that no single α-phase region was found in the present investigations although its existence has been reported for alloys with Al contents higher than 42 at%. Clemens et al. [21] have shown that the phase fractions occurring at a certain temperature depend strongly on the annealing time which was attributed to the slow dissolution kinetics of the β-phase. Under equilibrium conditions the following solidification and transformation pathway was proposed: $L \rightarrow L + \beta \rightarrow \beta \rightarrow \beta + \alpha \rightarrow \alpha \rightarrow \alpha + \gamma \rightarrow \alpha + \gamma + \beta_0 \rightarrow \alpha_2 + \gamma + \beta_0$. Continuous heating experiments performed with technically relevant heating rates, like in our in-situ HEXRD experiments, show a different behaviour as reflected in Figs. 4 and 5. Evidently, no α single phase field can be observed. Therefore, it is concluded that a heating rate of 2 K/min is not sufficiently low to enter the α single phase field. Consequently, for continuous cooling with moderate to high cooling rates as well as

for isothermal short-term heat treatments the following transformation sequence is proposed: $L \rightarrow L + \beta \rightarrow \beta \rightarrow \beta + \alpha \rightarrow \alpha\ (+ \beta_m) \rightarrow \alpha + \gamma\ (+ \beta_m) \rightarrow \alpha + \gamma + \beta_0 \rightarrow \alpha_2 + \gamma + \beta_0$, where β_m denotes the metastable β-phase. It is interesting to note that in case of the investigated alloys the thermodynamic calculation seems to describe a metastable phase behaviour rather than a behaviour expected in thermodynamic equilibrium.

In-situ neutron diffraction experiments were conducted during continuous heating on alloy A (Ti-43 Al-4 Nb-1 Mo-0.1 B) in order to study the two occurring order-disorder reactions: α_2 ($D0_{19}$) $\leftrightarrow\alpha$ (hcp) and β_0 (B2) $\leftrightarrow \beta$ (bcc). From Figs. 6 and 7 it is evident that the disordering of the α_2-phase takes place at 1174°C which is in good agreement with the eutectoid temperature determined by DSC experiments (Table 1).

Thermodynamic calculations predict that the order-disorder reaction $\beta_0 \leftrightarrow \beta$ takes place at a temperature of about 1420 °C [4], contradicting the good workability found at considerably lower hot-working temperatures [6-7]. Again, from Figs. 6 and 7 it is obvious that the database used does not predict the ordering temperature correctly. The neutron diffraction experiments show clearly that ordering occurs at about 1224 °C, which is far below the predicted value.

6 Conclusions

Three different γ-TiAl alloy variants were investigated to determine the influence of β/β_0-stabilizing elements on the prevailing phase fractions and transition temperatures. Both experiment and thermodynamic calculation with a commercial database show that an increase in Mo or Nb content increases the β/β_0-phase fraction as well as the eutectoid temperature. It has been shown that the predicted (ThermoCalc) and experimentally determined (in-situ HEXRD) evolution of phase fractions with temperature are in good agreement.

To prove the consistency of the HEXRD results, ex-situ experiments in which the samples were examined metallographically were carried out. From comparison with earlier work it is concluded that the heating rate at which the in-situ HEXRD experiments were carried out (2 K/min) is too high to obtain phase fractions that correspond to equilibrium conditions. This is highlighted by the fact, that no single α-phase field region was detected during the HEXRD experiments.

The measured phase transition temperatures deviate significantly from the ones predicted by ThermoCalc. It is shown, that T_α exhibits a rather strong dependence on heating rate which is in vivid contrast to the behaviour of T_{eu}. Temperatures of the ordering reactions were determined by in-situ neutron diffraction experiments which are particularly sensitive to atomic order in the Ti-Al system. It was thereby shown that the disordering temperature of β_0 is far below the value predicted by ThermoCalc. Upon heating with

2 K/min, the correct sequence of disordering is $\alpha_2 \rightarrow \alpha$ at T_{eu}, followed by $\beta_0 \rightarrow \beta$ before γ disappears at T_{α}.

7 Acknowledgements

Part of this research project has been supported by the European Commission under the 7th Framework Programme through the 'Research Infrastructures' action of the 'Capacities' Programme, Contract No: CP-CSA_INFRA-2008-1.1.1 Number 226507-NMI3 and by the Styrian Materials Cluster, Austria. Kun Yan contributed to the successful conduction of neutron scattering experiments which is gratefully acknowledged. In addition, the authors thank Volker Güther, GfE Metalle und Materialien GmbH, Nuremberg, Germany for fruitful discussions and preparation of the alloys.

References

[1] H. Kestler, H. Clemens, Production, processing and applications of gamma-TiAl based alloys, in: C. Leyens, M. Peters (Eds.) Titanium and Titanium Alloys, WILEY-VCH, Weinheim, Germany, 2003, pp. 351-392.

[2] X. Wu, Review of alloy and process development of TiAl alloys, Intermetallics, 14 (2006) 1114-1122.

[3] M. Yamaguchi, H. Inui, K. Ito, High-temperature structural intermetallics, Acta Materialia, 48 (2000) 307-322.

[4] H. Clemens, W. Wallgram, S. Kremmer, V. Güther, A. Otto, A. Bartels, Design of novel β-solidifying TiAl alloys with adjustable β/B2-phase fraction and excellent hot-workability, Adv. Eng. Mater., 10 (2008).

[5] H.F. Chladil, H. Clemens, G.A. Zickler, M. Takeyama, E. Kozeschnik, A. Bartels, T. Buslaps, R. Gerling, S. Kremmer, L. Yeoh, K.D. Liss, Experimental studies and thermodynamic simulation of phase transformations in high Nb containing γ-TiAl based alloys, Int J Mater Res, 98 (2007) 1131-1137.

[6] S. Kremmer, H. Chladil, H. Clemens, A. Otto, V. Güther, Near conventional forging of titanium aluminides, in: M. Niinomi, S. Akiyama, M. Ikeda, M. Hagiwari, K. Maruyama (Eds.) Ti-2007 Science and Technology, The Japan Institute of Metals (JIM), Sendai, Japan, 2008, pp. 989-992.

[7] W. Wallgram, T. Schmoelzer, L. Cha, G. Das, V. Güther, H. Clemens, Technology and mechanical properties of advanced γ-TiAl based alloys, Int J Mater Res, 100 (2009) 1021-1030.

[8] M. Grujicic, Y. Zhang, Combined atomistic-crystal plasticity analysis of the effect of beta phase precipitates on deformation and fracture of lamellar $\gamma+\alpha_2$ titanium aluminide, Journal of Materials Science, 34 (1999) 1419-1437.

[9] K.D. Liss, T. Schmoelzer, K. Yan, M. Reid, M. Peel, R. Dippenaar, H. Clemens, In situ study of dynamic recrystallization and hot deformation behavior of a multiphase titanium aluminide alloy, Journal of Applied Physics, 106 (2009).

[10] T. Tetsui, K. Shindo, S. Kaji, S. Kobayashi, M. Takeyama, Fabrication of TiAl components by means of hot forging and machining, Intermetallics, 13 (2005) 971-978.

[11] F. Appel, J.D.H. Paul, M. Oehring, U. Fröbel, U. Lorenz, Creep behavior of TiAl alloys with enhanced high-temperature capability, Metallurgical and Materials Transactions A: Physical Metallurgy and Materials Science, 34 A (2003) 2149-2164.

[12] H. Clemens, H.F. Chladil, W. Wallgram, B. Böck, S. Kremmer, A. Otto, V. Güther, A. Bartels, A β-stabilized γ-TiAl based alloy for improved processing performance, in, New Orleans, LA, 2008, pp. 217-228.

[13] F.S. Sun, C.X. Cao, S.E. Kim, Y.T. Lee, M.G. Yan, Alloying mechanism of beta stabilizers in a TiAl alloy, Metallurgical and Materials Transactions A: Physical Metallurgy and Materials Science, 32 (2001) 1573-1589.

[14] L.M. Droessler, T. Schmoelzer, W. Wallgram, L. Cha, G. Das, H. Clemens, Microstructure and tensile ductility of a Ti-43Al-4Nb-1Mo-0.1B alloy, in: Materials Res. Soc. Symp. Proc., MRS, Warrendale, 2009, pp. 121-126.

[15] H. Chladil, H. Clemens, A. Otto, V. Güther, S. Kremmer, A. Bartels, R. Gerling, Charakterisierung einer β-erstarrenden γ-TiAl-Basislegierung, BHM, 151 (2006) 356-361.

[16] H. Clemens, H.F. Chladil, W. Wallgram, G.A. Zickler, R. Gerling, K.D. Liss, S. Kremmer, V. Güther, W. Smarsly, In and ex situ investigations of the β-phase in a Nb and Mo containing γ-TiAl based alloy, Intermetallics, 16 (2008) 827-833.

[17] N. Saunders, Phase equilibria in multi-component γ-TiAl based alloys, in: Y.W. Kim, D.M. Dimiduk, M.H. Loretto (Eds.) Gamma Titanium Aluminides 1999, TMS, 1999, pp. 183.

[18] R.M. Imayev, V.M. Imayev, M. Oehring, F. Appel, Alloy design concepts for refined gamma titanium aluminide based alloys, Intermetallics, 15 (2007) 451-460.

[19] M. Takeyama, S. Kobayashi, Physical metallurgy for wrought gamma titanium aluminides: Microstructure control through phase transformations, Intermetallics, 13 (2005) 993-999.

[20] H.F. Chladil, H. Clemens, H. Leitner, A. Bartels, R. Gerling, F.P. Schimansky, S. Kremmer, Phase transformations in high niobium and carbon containing γ-TiAl based alloys, Intermetallics, 14 (2006) 1194-1198.

[21] H. Clemens, B. Boeck, W. Wallgram, T. Schmoelzer, L.M. Droessler, G.A. Zickler, H. Leitner, A. Otto, Experimental studies and thermodynamic simulations of phase transformations in Ti-(41-45)Al-4Nb-lMo-0.1B alloys, in: Materials Res. Soc. Symp. Proc., MRS, Warrendale, 2009, pp. 115-120.

[22] J.D. Shi, Z. Pu, Z. Zhong, D. Zou, Improving the ductility of γ(TiAl) based alloy by introducing disordered β phase, Scripta Metallurgica et Materiala, 27 (1992) 1331-1336.

[23] I.J. Watson, K.D. Liss, H. Clemens, W. Wallgram, T. Schmoelzer, T.C. Hansen, M. Reid, In situ characterization of a Nb and Mo containing γ-TiAl based alloy using neutron diffraction and high-temperature microscopy, Adv. Eng. Mater., 11 (2009) 932-937.

[24] K.D. Liss, A. Bartels, H. Clemens, S. Bystrzanowski, A. Stark, T. Buslaps, F.P. Schimansky, R. Gerling, C. Scheu, A. Schreyer, Recrystallization and phase transitions in a γ-TiAl-based alloy as observed by ex situ and in situ high-energy X-ray diffraction, Acta Materialia, 54 (2006) 3721-3735.

[25] K.-D. Liss, A. Bartels, A. Schreyer, H. Clemens, High-energy X-rays: a tool for advanced bulk investigations in materials science and physics, Textures and Microstructures, 35 (2003) 219-252.

[26] T. Novoselova, S. Malinov, W. Sha, A. Zhecheva, High-temperature synchrotron X-ray diffraction study of phases in a gamma TiAl alloy, Materials Science and Engineering A, 371 (2004) 103-112.

[27] W. Reimers, A.R. Pyzalla, A. Schreyer, H. Clemens, Neutrons and Synchrotron Radiation in Engineering Materials Science, WILEY-VCH, Weinheim, Germany, 2008.

[28] V. Güther, A. Otto, J. Klose, C. Rothe, H. Clemens, W. Kachler, S. Winter, S. Kremmer, Microstructure and corresponding tensile properties of as-cast, β-solidifying, γ-TiAl based TNM alloys, in: TMS Annual Meeting, New Orleans, CA, 2008, pp. 249-256.

[29] R. Schnitzer, H.F. Chladil, C. Scheu, H. Clemens, S. Bystrzanowski, A. Bartels, S. Kremmer, The production of lamellar microstructures in intermetallic TiAl alloys and their characterisation, Herstellung lamellarer gefügetypen in intermetallischen TiAl-legierungen und deren charakterisierung, 44 (2007) 430-442.

[30] S.G. Eeckhout, B. Gorges, L. Barthe, O. Pelosi, O. Safonova, G. Giuli, A high-temperature furnace for in situ synchrotron X-ray spectroscopy under controlled atmospheric conditions, Journal of Synchrotron Radiation, 15 (2008) 489-494.

[31] T. Tschentscher, P. Suortti, Experiments with very high energy synchrotron radiation, Journal of Synchrotron Radiation, 5 (1998) 286-292.

[32] J.E. Daniels, M. Drakopoulos, High-energy x-ray diffraction using the Pixium 4700 flat-panel detector, Journal of Synchrotron Radiation, 16 (2009) 463-468.

[33] A.P. Hammersley, S.O. Svensson, M. Hanfland, A.N. Fitch, D. Häusermann, Two-dimensional detector software: From real detector to idealised image or two-theta scan, High Pressure Research, 14 (1996) 235-248.

[34] A.J. Studer, M.E. Hagen, T.J. Noakes, Wombat: The high-intensity powder diffractometer at the OPAL reactor, Physica B: Condensed Matter, 385-386 (2006) 1013-1015.

[35] H. Rauch, W. Waschowski, in: A.-J. Dianoux, G. Lander (Eds.) Neutron Data Booklet, Old City Publishing, Philadelphia, 2003, pp. 1-17.

[36] V.F. Sears, International Tables for Crystallography 2006.

[37] L.B. McCusker, R.B. Von Dreele, D.E. Cox, D. Louër, P. Scardi, Rietveld refinement guidelines, Journal of Applied Crystallography, 32 (1999) 36-50.

[38] H. Chladil, Entwicklung und Charakterisierung von hoch Niob-haltigen γ-Titanaluminid Legierungen in: Department Physical Metallurgy and Materials Testing, University of Leoben, Leoben, Austria, 2007.

[39] L.A. Yeoh, K.D. Liss, A. Bartels, H. Chladil, M. Avdeev, H. Clemens, R. Gerling, T. Buslaps, In situ high-energy X-ray diffraction study and quantitative phase analysis in the α + γ phase field of titanium aluminides, Scripta Materialia, 57 (2007) 1145-1148.

ADVANCED ENGINEERING MATERIALS

Appendix D:
An In-Situ High-Energy X-Ray Diffraction Study on the Hot-Deformation Behavior of a β-Phase Containing TiAl Alloy

T. Schmoelzer, K.-D. Liss, C. Kirchlechner, S. Mayer, A. Stark, M. Peel and H. Clemens,

Submitted to Intermetallics

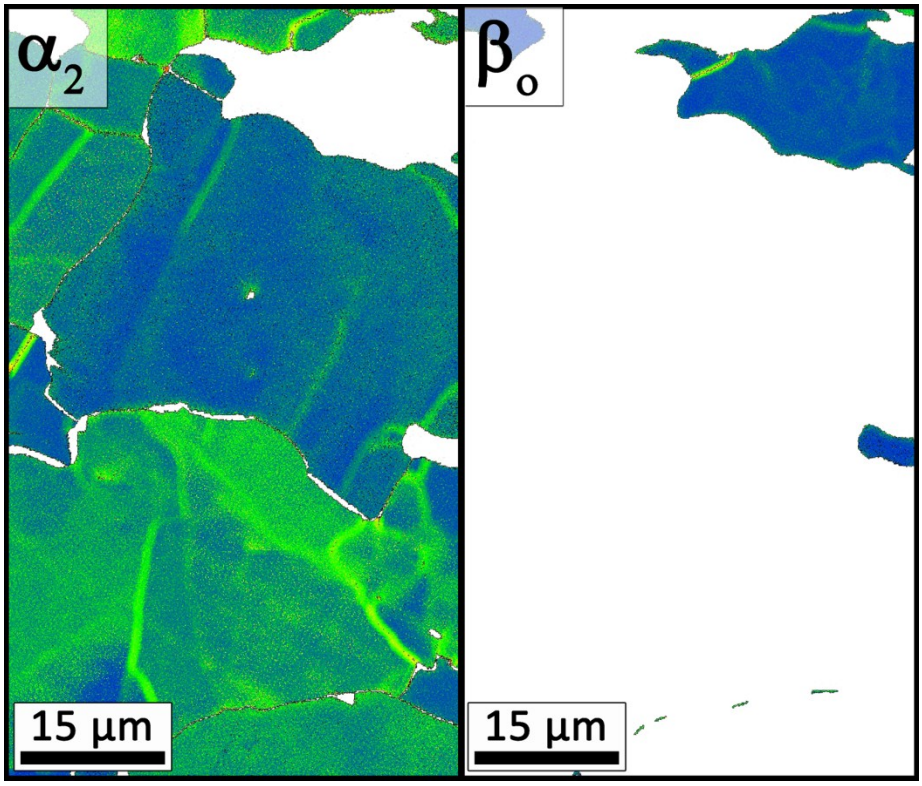

An in-situ high-energy X-ray diffraction study on the hot-deformation behavior of a β-phase containing TiAl alloy

T. Schmoelzer *[a], K.-D. Liss [b], C. Kirchlechner [c], S. Mayer [a], A. Stark [d], M. Peel [e], H. Clemens [a]

[a] Department of Physical Metallurgy and Materials Testing, Montanuniversität Leoben, 8700 Leoben, Austria.

[b] Australian Nuclear Science and Technology Organisation, Lucas Heights, New South Wales 2232, Australia.

[c] Department Material Physics, Montanuniversität Leoben, 8700 Leoben, Austria.

[d] Institute of Materials Research, Helmholtz-Zentrum Geesthacht, 21502 Geesthacht, Germany.

[e] Department of Mechanical Engineering, University of Bristol, Bristol, UK.

Abstract

In engineering materials, microstructural evolution during hot-working critically determines the properties of the finished part. Intermetallic TiAl alloys are no exception and numerous attempts have been made to improve their performance by subjecting them to harmonized hot-working steps. In the current work a novel in-situ diffraction technique along with conventional microscopic methods were employed to characterize the behavior of the individual phases at two different deformation temperatures. A so-called TNM™ alloy with a nominal composition of Ti-43.5 Al-4 Nb-1 Mo-0.1 B (in at%), which exhibits an adjustable fraction of disordered β-phase at elevated temperatures, was deformed isothermally at 1220 °C and 1300 °C. At 1220 °C three phases (α,β,γ) are present in thermodynamic equilibrium which reduces to two (α,β) at 1300 °C. It was possible to observe in-situ the individual behavior of the involved phases during deformation and the phenomena which accommodate the defects generated by hot-working. Results of post mortem microscopic investigations were used to confirm the findings. The results of the in-situ experiments give unique insights into the hot-deformation behavior of multi-phase TiAl alloys, which can be used for specific process optimization and for further alloy development.

Keywords: A. titanium aluminides, based on TiAl; C. thermomechanical treatment; F. diffraction; G. aero-engine components;

1 Introduction

Intermetallic γ-TiAl alloys exhibit high strength at elevated temperatures while having low density [1–5]. These properties make them an attractive material for the application in turbine blades of aero-engines as well as in turbocharger turbine wheels for reciprocating engines [6–9]. Due to the continuous strive of manufacturers to improve engine efficiencies, the demands on the performance of components are ever increasing. A transition in the production route, from casting towards implementation of a hot-working step, combined with subsequent heat-treatments is expected to enable a more thorough control of the microstructure and thus improve the mechanical properties of the finished part [10–12].

Alloys of the so-called TNM™ family can be forged using an isothermal or a near-conventional process [7,13,14]. This type of alloy is particularly well suited for forging and rolling due to the presence of the ductile, disordered body-centered cubic (bcc) β-phase at hot-deformation temperatures [10,13,15]. While it is well established that the β-phase promotes the hot-deformation behavior [16–18], it is not clear which microstructural mechanisms act during forging. A number of papers have been published concerning the hot-deformation of γ-TiAl alloys, mostly reporting compression experiments performed at different temperatures and strain rates where the specimens were subjected to subsequent microstructural investigations [19–25]. Such post-mortem investigations are complicated by the fact that multiple phase transformations and ordering reactions may occur upon cooling to room-temperature. Information on phase equilibria and transformation temperatures in the Ti-Al system can be found elsewhere [26]. Recent studies on the pseudo-binary phase diagram of TNM™ alloys are also available [27–29]. A second method infers microstructural information from the shape of the flow-curve which is determined by the deformation response of each individual phase and their interactions [20,22–24]. In practice, information obtained from the flow-curve predominantly describes the behavior of the majority phase. Additionally, it is notable that most experiments on TiAl alloys have been conducted within the (α_2+γ) (α+γ) or (α+β_o+γ) phase field regions. Consequently, little information concerning deformation at very high temperatures, i.e. in the (α+β) phase field region is available.

In this study, an attempt was made to observe the behavior of an engineering β-containing TiAl alloy in-situ during hot-deformation. To this end, a high-energy X-ray diffraction (HEXRD) method developed by Liss et al was utilized [30–32]. The findings obtained by the in-situ method were confirmed by the results of post-mortem microstructural investigations. Performing in-situ experiments at two different temperatures - in the (α+β) and the (α+β+γ) phase field regions - allows comparison of the deformation behavior dependent on the phases present. The obtained results ultimately contributed to determining suitable process parameters for industrial forming operations [12,13].

2 Materials and Methods

The alloy investigated had a nominal chemical composition of Ti-43.5 Al-4 Nb-1 Mo-0.1 B (in at%) and was supplied by GfE Metalle und Materialien GmbH, Nuremberg, Germany. Ingots with a diameter of 55 mm were produced by means of centrifugal casting. To close residual porosity, the ingot was subsequently hot-isostatically pressed (HIP) at a temperature of 1200 °C and a pressure of 200 MPa for 4 h. The three main phases are the α_2-Ti_3Al (DO_{19} structure), the β_o-Ti phase (B2 structure) as well as their disordered polymorphs (α: A3 structure, β: A2) and the γ-TiAl phase ($L1_0$). The β/β_o-phase fraction has a minimum at 1285 °C which is also the transition temperature between the (α+β) and (α+β+γ) phase field region. A pseudo-binary section of the phase diagram calculated with a commercial TiAl data base [33] is presented in Figure 1a. Alloy composition and deformation temperatures used in the current study are indicated. The course of phase fractions over temperature shown in Figure 1b was acquired during a previous study [28].

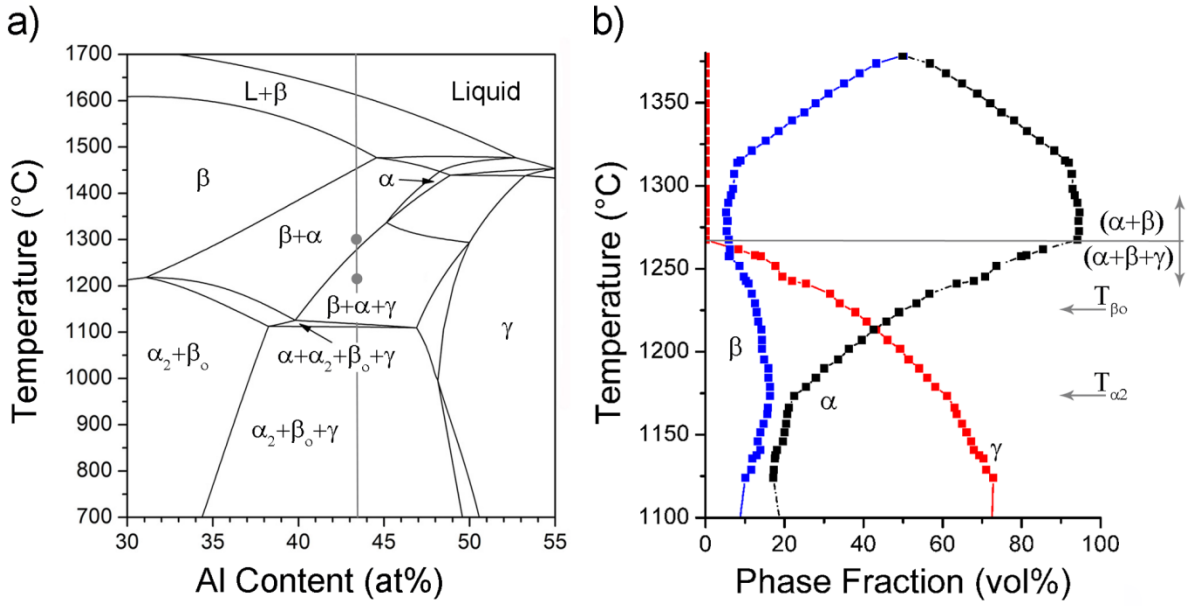

Figure 1: (a) calculated binary section of the quaternary phase diagram [27] and (b) experimentally determined course of phase fractions over temperature of the investigated alloy [28]. In (a), the alloy composition is indicated by a vertical line, the two deformation temperatures are marked by filled circles. Order/disorder transition temperatures of α_2/α and β_o/β are indicated by $T_{\alpha 2}$ and $T_{\beta o}$, respectively in (b) [34].

For further details, especially on the difference between calculated and experimentally established phase diagrams, the reader is referred to [27–29]. At 1300 °C, i.e. in the (α+β) phase field region, the volume fractions of α and β are approximately 93 vol% and 7 vol% whereas at 1220 °C, volume fractions of α, β, and γ were determined to 46 vol%, 13 vol%, and 41 vol% respectively. In Figure 1b, the $\beta_o \leftrightarrow \beta$ and $\alpha_2 \leftrightarrow \alpha$

order/disorder temperatures obtained from neutron diffraction experiments are indicated [34]. As the phenomena occurring during deformation are discussed, it should be born in mind that the experiments were conducted at very high homologous temperatures. A deformation temperature of 1300 °C corresponds to approximately $0.87 \times T_m$ whereas 1220 °C are equivalent to $0.82 \times T_m$.

The experimental setup for investigating dynamic microstructural processes with high-energy X-rays [35] is based on a conventional powder diffraction experiment at a synchrotron source. In the illuminated specimen volume, a limited number of grains should be contained to be able to distinguish single diffraction spots from individual crystallites lying on the Debye-Scherrer rings. Yet a sufficiently high number of grains have to be observed to allow drawing conclusions about the prevailing microstructure. A suitable condition was achieved by using a monochromatic beam with a mean energy of 86.94 keV and a cross-section of 0.1 × 0.1 mm2 as well as cylindrical specimens with a diameter of 4 mm and a length of 8 mm. Diffraction patterns were recorded at a frame rate of about 2 Hz by a Pixium 4700 flat panel detector [36] (Thales Group, Neuilly-sur-Seine, France) which was placed at a distance of 1233.8 mm from the specimen position. The sample-detector distance was determined by means of triangulation and the mean energy of the beam calibrated by employing a CeO_2 standard.

An electro-thermomechanical tester (ETMT) (Instron, Norwood, MA, USA) was utilized for heating and deforming the samples. With this device, heating was achieved resistively with a maximum current of 450 A at 8 V while mechanical loads of up to 3 kN can be imposed on the specimen. The temperature was measured with a type S thermocouple formed to a melt bead which was spot-welded directly onto the specimen surface. Inserting Ta and graphite foil between the specimen and the anvils provided a diffusion barrier and decreased friction forces at the interface. Since the ETMT has a moving and a stationary anvil, the motorized table that carried the ETMT was controlled in such a way that the beam illuminated the same specimen volume throughout the entire experiment.

The specimens were heated to the intended temperatures (1220 °C and 1300 °C) at a rate of 10 °C/s and held at this temperature for 30 s. Then, compression started with a constant anvil speed of 0.021 mm/s which translates to a mean strain rate of $3.7 \cdot 10^{-3}\ s^{-1}$. During the experiment performed at 1300 °C, deformation was discontinued for 20 s to investigate the corresponding materials response. Although the experiment was set up for isothermal deformation the temperature started to decrease at high strains. This was caused by the increase in specimen diameter during compression which lead to a decrease in electrical resistance and, correspondingly, the heating power. After a total strain of $\phi \sim 0.9$, the experiments were terminated. To validate the stress-strain data obtained with the ETMT, hot-compression experiments were conducted on a Gleeble thermo-mechanical

simulator at a constant strain rate of $5\times10^{-3}\,s^{-1}$ and temperatures of 1200 °C and 1300 °C [37].

As dynamic processes are occurring in the microstructure of the specimen, both during heating and deformation, the morphology of the reflection spots on the Debye-Scherrer rings changes. Broadening of a spot is caused by the introduction of defects into the lattice. Sub-grain formation may be identified by the dissociation of one diffraction spot into a distribution cone characterized by its mosaic spread, or, if resolved, into a set of individual peaks within a narrow angular range [38]. A crystallite of small size is represented by a sphere of finite radius rather than a point in reciprocal space and, hence, produces also a broader diffraction spot [39]. Additionally, if the diffraction patterns are recorded continuously, grain rotation can be detected during plastic deformation [40,41]. It has, however, to be born in mind that a grain which satisfies the Bragg-condition only continues to do so if its rotation axis is parallel to the incident beam. Texture evolution during hot-working becomes evident in the intensity distribution over the azimuthal angle and the different Debye-Scherrer rings [41]. In a kinematic approximation, the intensity of the individual diffraction spots is proportional to the volume of the corresponding crystallites [39]. More details on the employed diffraction method can be found in [30–32,42,43]. To illustrate the development of reflections with time, the intensity on one Debye-Scherrer ring is plotted in greyscale as a function of azimuthal angle and time. In these azimuthal angle time plots (called AT-plots henceforth) a stationary reflection spot produces a continuous line. If the line is tilted, the spot (and hence, the grain) rotates about the beam axis. Such lines are called timelines in the following. More details on the generation and interpretation of an AT-plot can be found in [31,32].

After completion of the experiments, microstructural investigations were performed on the deformed specimens. Micrographs were obtained on a Zeiss EVO 50 scanning electron microscope (SEM) at an acceleration voltage of 20 kV in back scattered electron (BSE) imaging mode. Electron backscatter diffraction (EBSD) images were obtained on a LEO field emission gun SEM (Zeiss 1225) equipped with an EDAX EBSD system. An acceleration voltage of 30 kV and a 120 µm aperture were used for image acquisition.

3 Results

After casting and HIP, the material exhibits a microstructure as shown in Figure 2. In this condition, colonies consisting of coarse α_2 and γ lamellae as well as globular γ-grains are present. The lamellar colonies have a broad size distribution with the largest ones reaching lengths of up to 200 µm, whereas the maximum diameter of the globular γ-grains is about 20 µm. A substantial amount of β_o-phase is observed which encompasses the lamellar colonies. Additionally, small β_o precipitates can be found within the α_2-laths of the lamellar colonies. It should be noted that the relatively fine-grained cast microstructure shown in

Figure 2 is achieved by the addition of boron. A good chemical homogeneity is attained by solidification via the β-phase [10].

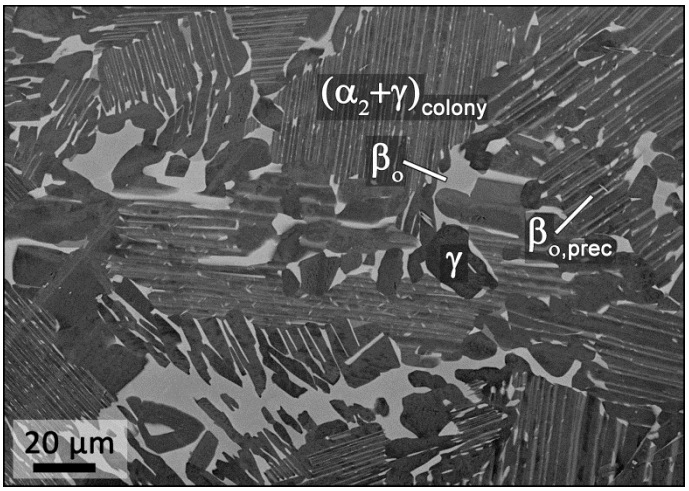

Figure 2: Microstructure of the cast and HIP starting material. Three phases are present of which β_o images brightest, α_2 appears in an intermediate shade of grey and γ is the darkest phase. The image was obtained by means of SEM in BSE contrast.

Microstructural images obtained from the specimens deformed during the in-situ HEXRD experiments at 1300 °C and 1220 °C are depicted in Figure 3. Due to the high cooling rate, the two-phase (α+β) microstructure present at a deformation temperature of 1300 °C was preserved in 3 a. Upon cooling, only the $\alpha \rightarrow \alpha_2$ and $\beta \rightarrow \beta_o$ ordering reactions took place. The β_o-grains have attained a form that is more elongated perpendicular to the compression direction than the α-grains. Additionally, the complex shapes of the β_o-grains should be noted. Figure 3b shows a microstructural image of the specimen deformed at 1220 °C in the (α+β+γ) phase field. Consequently all three phases are observed in the micrograph. The γ-phase is present in the form of globular grains and coarse lamellae within colonies, some of which have buckled during deformation. It is worth mentioning that no γ-lamellae oriented parallel to the compression direction were observed. Lamellae that buckled during deformation appear to have been the ones that were initially parallel to the loading axis (Figure 3b inset). Compared to the starting microstructure (Figure 2), grain refinement is more pronounced in the specimen deformed at 1220 °C (Figure 3b) than in the one deformed at 1300 °C (Figure 3a).

AT-plots of the deformation experiments performed at 1300 °C and 1220 °C as well as the parameters temperature, true stress, and true strain are presented in Figure 4a-f. For two representative reflections, α 022 (Figure 4a) and β 002 (Figure 4b), the development of diffraction patterns over time is given only for azimuthal angles between 0° and 180° to avoid the use of overly large images.

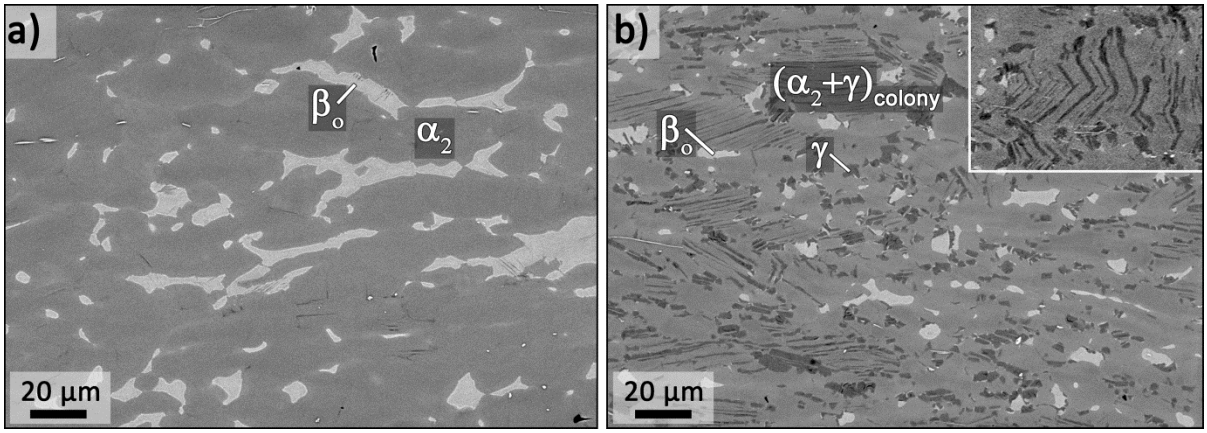

Figure 3: Microstructures after deformation at 1300 °C (a) and 1220 °C (b). In (a) only α_2 and β_o-phase are present while in (b) also γ-phase is evident. Labels in the micrographs indicate the phases present during hot-deformation. The inset in (b) shows lamellae that buckled during compression. In both images the compression direction is vertical and the scale of the inset is identical to the main image (b).

Figures 4c and f show the development of temperature, true stress and true strain as a function of time. Both experiments were performed isothermally except for the aforementioned cross-section related decrease towards the end of the test, which correlated with an increase in flow stress as would be expected [20,24]. Deformation was intentionally discontinued for 20 s during the experiment performed at 1300 °C to be able to observe static annealing phenomena.

During continuous heating to 1300 °C, at about 1280 °C, a sudden change in the intensity of α reflections occurs (Figure 4a) signifying the dissolution of the γ-phase. Some of the β spots intensify and new ones are appearing (Figure 4b). While holding at 1300 °C, the α-phase reflections are static, whereas the β spots show some degree of fluctuation. As deformation starts, α-phase timelines tilt, some bifurcate and all of them broaden. In the AT plots of the β-phase, dot-clouds are formed almost instantaneously. After 217 s, deformation was discontinued and the static behavior of the material can be observed.

For both phases the number of timelines observed while deformation was stopped is greater than that before the onset of deformation. This indicates that grain refinement has occurred. Once more, the α-phase grains produce timelines in which only a few intensity fluctuations are present. The β-phase, on the other hand, exhibits strongly fluctuating intensity. As deformation continues at 1300 °C, the α-phase timelines tilt again, whereas those of the β-phase disintegrate into dots. Upon further deformation only dots are observed in the AT-plot of the β-phase (Figure 4b).

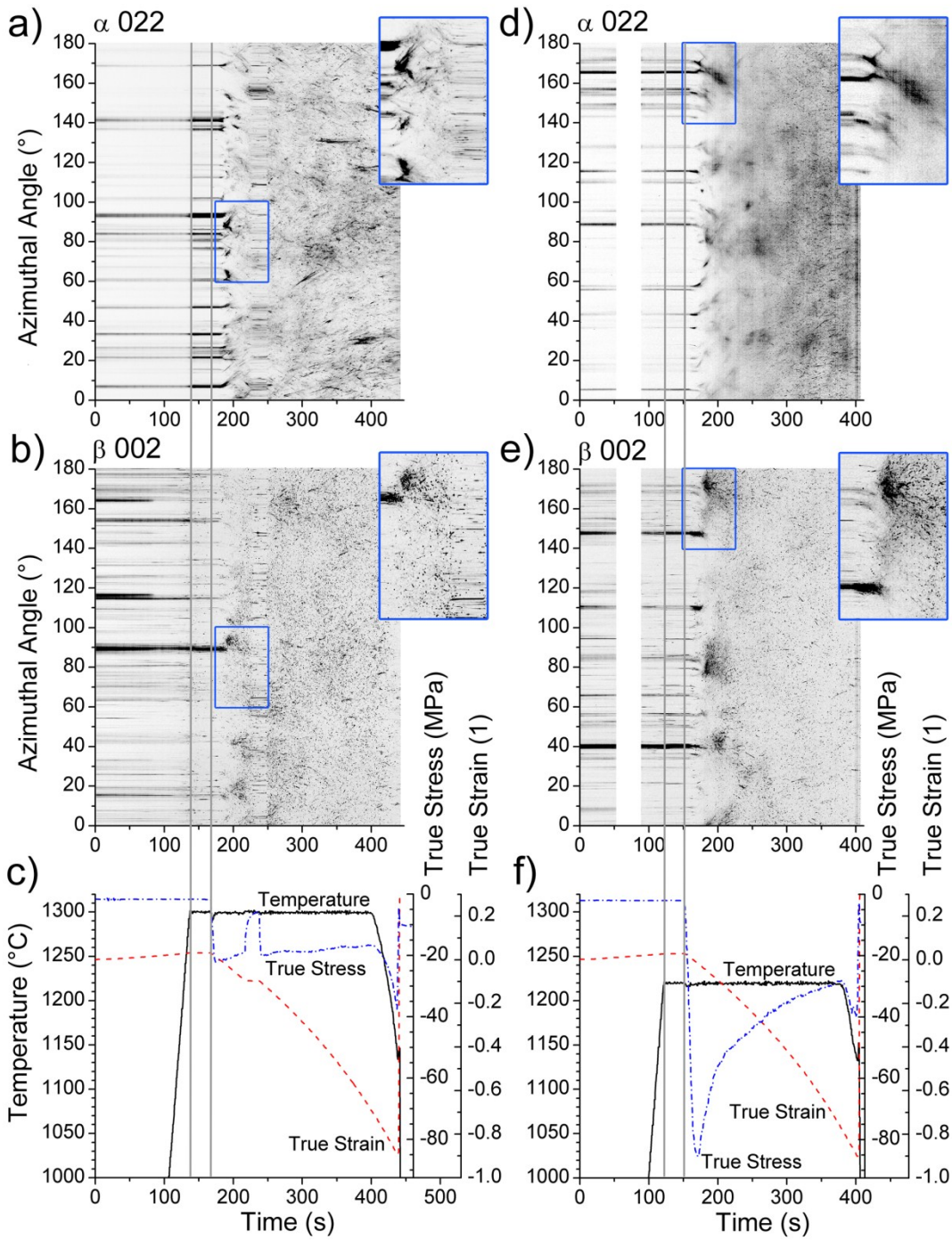

Figure 4: AT plots of specimens deformed at 1300 °C (left column) and at 1220 °C (right column). Both, α 022 (a,d) and β 002 (b,e) reflections are imaged as well as temperature, true stress and true strain (c,f) throughout the hot compression experiment. During heating, the temperature increases linearly from RT to deformation temperature. Temperature values below 1000 °C are omitted to improve readability. The vertical lines mark reaching of the deformation temperature and the onset of loading while the insets provide a magnified view of pattern development at the beginning of deformation.

The plot of the α-phase, on the other hand, reveals a few timelines of high intensity that are inclined with respect to the time axis (Figure°4a). Generally, timelines of the α-phase are longer than those of the β-phase.

The AT-plots of α and β-phase of the experiment performed at 1220 °C are shown in Figures 4d and 4e. No images were acquired between 54 s and 89 s due to the fact that the detector routine was interrupted and had to be restarted. Since no fluctuations occur in the α or β-phase after the period during which no images were recorded, it can be assumed that no important microstructural developments were missed during heating. Again, during the holding time only the β reflections fluctuate in intensity (Figure 4d, e). As deformation commences, the α-phase timelines instantly broaden and are increasingly blurred as deformation increases. Starting at 270 s, comparably sharp reflection dots are appearing in the AT-plot of the α-phase. The AT-plot of the β-phase reveals the splitting of timelines into dot-clouds when deformation starts and only a few short, comparably sharp timelines are observed until the final deformation is attained (Figure 4e).

In the investigated alloy, also γ-phase is present at 1220 and the AT-plot of its 020 reflection is presented in Figure 5a. During heating, only gradual changes in intensity are observed. Similar to all other phases the majority of γ timelines broaden as deformation starts. Some, however, remain sharp for a long period of time (see inset in Figure 5a). With increasing strain sharp dots appear which are of low intensity. Single timelines are increasingly difficult to see as deformation progresses.

During the experiment, the load imposed on the specimen and the anvil position were recorded. Together with the starting geometry of the specimens, these data allow calculating the true stress and true strain under the assumptions that the specimens retain a cylindrical shape and their volumes remain constant. Stress-strain curves that were attained in this fashion are featured in Figure 6. After loading, the curve obtained at 1300 °C exhibits a fairly constant flow-stress of around -20 MPa. The discontinuity in the curve stems from the short period of time during which the deformation was paused. In contrast, the flow-stress at 1220 °C rises rapidly to -80 MPa just after just after deformation commences before more gradually declining throughout the test.

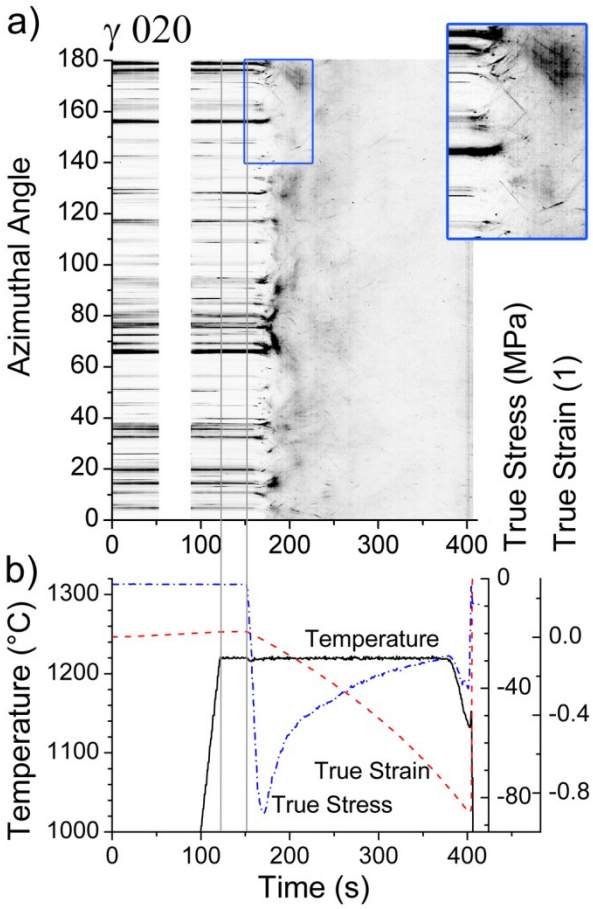

Figure 5: (a) AT-plot of the γ 020 reflection of the specimen deformed at 1220 °C and (b) the corresponding deformation parameters. In the inset, a section of the AT-plot is magnified. Temperature values below 1000 °C are omitted to improve readability. Vertical lines mark reaching of the deformation temperature and the onset of loading.

After deformation, the specimens used in the in-situ experiments were investigated with regard to their microstructure by means of EBSD. Kernel average misorientation maps of the specimen deformed at 1300 °C are presented in Figure 7. In this mode, the misorientations between a center point and its next-nearest neighbors are evaluated. The average misorientation is then calculated and assigned to the center point. Details on this procedure can be found in [44,45]. A number of sub-grain boundaries are visible in the α_2-phase grains. Additionally, high degrees of misorientation are observed within some grains. In contrast to this, the β_o grains exhibit rather low defect densities.

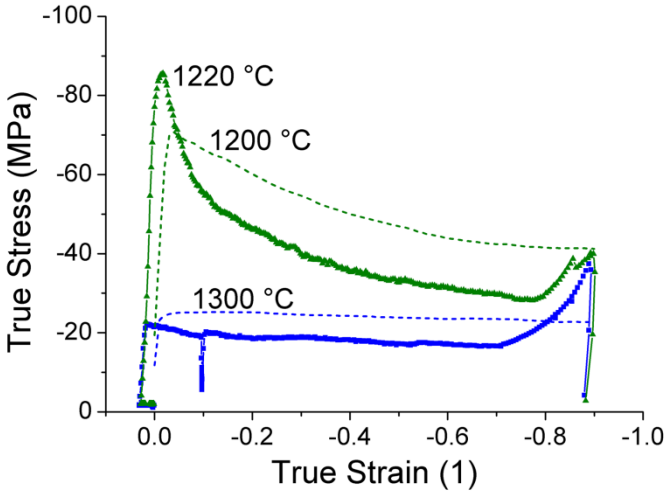

Figure 6: Stress-strain curves of specimens deformed at 1300 °C (α+β phase field region) and 1220 °C (α+β+γ phase field region). The data were acquired during the in-situ experiment where the specimen was deformed at a mean strain rate of 3.7×10^{-3} 1/s. The dashed lines show the results of experiments conducted with a Gleeble thermo-mechanic simulator at temperatures of 1200 °C and 1300 °C at a strain rate of 5×10^{-3} s-1 [37].

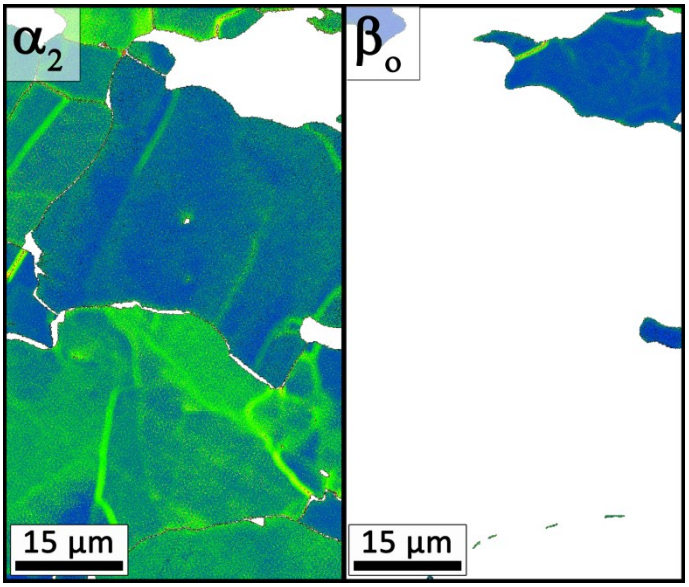

Figure 7: Kernel average misorientation maps of α_2 and β_o-phase obtained by EBSD (light colors correspond to high misorientations). The images show the microstructure of the specimen after deformation at 1300 °C. Note that both phases were disordered at 1300 °C.

In Figure 8, kernel average misorientation maps of the specimen deformed at 1220 °C are shown. At this temperature three phases (α, β and γ) were present during deformation. Due to the precipitation of fine γ-lamellae during cooling (after deformation), the α_2-phase was not properly resolved in the EBSD image. The γ-phase is only imaged if

present in the form of globular grains or coarse lamellae. In these areas, some low-angle grain boundaries (LAGB) and orientation gradients within grains are observed. It is obvious from Figure 8 that, apart from a few LAGB, only a low number of defects were stored in the β_o-phase. The misorientation plot of the γ-phase reveals the presence of sub-grain boundaries and of certain areas of high misorientation especially in coarse lamellae.

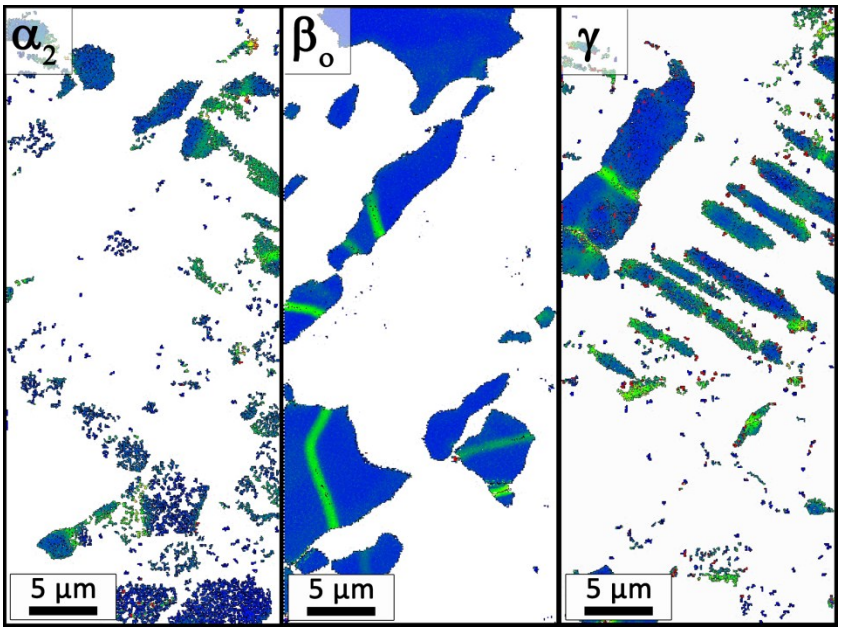

Figure 8: Kernel average misorientation maps obtained after deformation of the specimen at 1220 °C. Due to high defect densities within the γ and the α_2-phase and the lamellar arrangement of the two phases, only the β_o-grains are imaged properly. Light colors correspond to high degrees of misorientation. Note that at 1220 °C, α and β-phase are present in their disordered states.

4 Discussion

The reason for implementing complex hot-deformation steps in the production route of TiAl parts is to improve the microstructure and therefore the mechanical properties of the product [1,2,4,7,46,47]. A comparison between the microstructures present before (Figure 2) and after (Figure 3) hot-deformation shows that the grains elongated perpendicular to the compression direction during plastic deformation. After hot-compression at 1220 °C, many lamellar grains are oriented with the lamellae perpendicular to the load axis (Figure 3b). This observation is explained by the fact that lamellar colonies exhibit a deformation behavior that is similar to a stack of cards. If the lamellae are perpendicular to the loading direction, the colony is in hard mode because the α-phase (respectively α_2-phase below the ordering temperature) has to deform in its hardest slip mode. In the soft mode, the lamellae enclose an intermediate angle (ideally 45°) with

respect to the loading direction and deform easily via shear parallel to the interfacial planes. Colonies in which the lamellae are parallel to the load exhibit an intermediate yield stress [48].

The elongated shape of the β_o-grains after deformation suggests that disordered β accommodated a disproportionally large fraction of the strain (Figure 3). This finding is in accord with literature results [49]. Additionally, it is commonly known that hot-deformation at lower temperatures leads to finer grained microstructures [50] which is confirmed by Figures 3a and 3b and previous studies conducted on various TiAl alloys, e.g. [49,51,52].

4.1 α-phase

The results from in-situ HEXRD experiments allow bridging the gap between the microstructural images before and after the compression experiment. In the AT-plots of both investigated deformation temperatures, the α timelines tilt and broaden as soon as deformation starts (Figures 4a and d). This indicates the occurrence of grain rotation about the beam axis and defect formation (i.e. dislocation multiplication). Timelines frequently bifurcate at 1300 °C, which is less frequently observed at 1220 °C. Bifurcation can be caused by the arrangement of dislocations to sub-grain boundaries which infers that at 1220 °C processes that lead to such an arrangement occur less readily. Another notable difference is that timelines remain sharper during deformation at 1300 °C, than at 1220 °C (Figures 4a and d).

Sharp timelines or dots appear in significant numbers at a strain of ~0.25 (at t=250 s) while the material is being deformed at 1220 °C. This implies that new grains with low defect density appear after some minimum plastic strain and time. Dynamic discontinuous recrystallization (DDRX) is known to require a minimum amount of plastic deformation and a so-called incubation time [53]. Consequently, the observation of the sudden appearance of grains with low defect density can be ascribed to DDRX.

At 1300 °C, the dominant features in the AT-plot of the α 022 reflection are long timelines that show moderate broadening (Figure 4a). Instantaneous bifurcation of timelines upon the onset of compression points towards the accommodation of defects by a continuous process that does neither require a minimum strain, nor an incubation time. An important factor in determining which process is likely to contribute most to accommodating the defects is the stacking fault energy (SFE). No accurate values of the SFE in the α/α_2-phase are to be found in literature, but there seems to be some consensus on the fact that it is high [49] which favors dynamic recovery (DRV). Considering these facts it is concluded that the α-phase undergoes a significant degree of recovery at 1300 °C. Additionally, HAGB formation may occur by continuous recrystallization. In general, the defect densities in the α-phase are high after deformation which is in accord with the findings of Liu et al. [49].

The EBSD map of the α_2-phase after deformation at 1300 °C (Figure 7) reveals that grains with different defect densities are present. Additionally, sub-grain boundaries are observed in the microstructure which is further evidence for the occurrence of DRV.

4.2 β-phase

Contrary to the AT-plots of the α-phase, those of the β-phase show strong similarities at the two investigated temperatures (Figure 4b and e). In both experiments, changes in the timelines of the β-phase are obvious even before deformation starts at t~125 s. Since no strain is imposed on the specimen at this stage, only grain coarsening and phase transformation processes can change the intensity of a diffraction spot. Strains due to different coefficients of thermal expansion or phase strains can rotate crystallites by a small degree which might also lead to a significant change in intensity. Although there are single timelines vanishing and appearing during this stage, continuous timelines are far more dominant. This suggests that only a few grains are affected by the aforementioned processes. As soon as the specimen is subjected to deformation, the timelines disintegrate into clouds of small, comparatively sharp reflection spots located around the position of the original timeline. Many sharp spots with low intensities within a small angular range correspond to a large number of rather small crystallites with low defect densities and small misorientations [38]. This behavior is characteristic for DRV which is consequently identified as the dominant process. This conclusion is supported by the fact that the bcc β-phase is presumed to have a high SFE due to its similarity to β-Ti [49,54]. Additionally, it has been found for a different TiAl alloy [49] that the β-phase accommodates a large fraction of plastic strain during hot-deformation, which is confirmed by the morphology of the β-phase shown in Figure 3.

The main difference between the AT-plots obtained at the two different temperatures is that the reflection spots are sharper and of higher intensity at 1300 °C compared to 1220 °C (Figures 4b and e). This behavior is attributed to the fact that thermally activated recovery processes are occurring faster at higher temperatures.

Since both experiments were performed at the same strain rate, more rapidly occurring DRV processes lead to lower defect densities in steady-state conditions. Furthermore, the flow-stress has a pronounced influence on the sub-cell size [55,56]. The lower the flow-stress, the larger the sub-cells, which explains the higher intensity of reflection spots at 1300°C. From EBSD results (Figure 8), it is obvious that the β_o-phase grains have low defect densities. Some sub-grain boundaries are observed, especially after deformation at 1220 °C, which could point towards DRV and DDRX. An unambiguous conclusion concerning the processes occurring in β was only possible based on the results of the in-situ diffraction experiment.

4.3 γ-phase

Deformation at 1220°C is performed in the (α+β+γ) phase field region. During heating, the volume fraction of γ-phase is decreasing (Figure 1b) which is reflected by the overall loss in intensity visible in the AT-plot (Figure 5a). One important fact to notice is that the γ-phase is present in the form of globular grains and as lamellae within the α/γ lamellar colonies at deformation temperature. Since γ and α laths of the same colony satisfy the Blackburn orientation relationship [57], reflections stemming from one colony exhibit determined correlations on the Debye-Scherrer rings [58] and image similar to globular γ-grains in the AT-plot. The fluctuations in intensity before deformation starts (Figure 5a) are attributed to coarsening and phase transformation processes. As a plastic strain is imposed on the specimen, most timelines broaden and tilt. However, there are some timelines that tilt but do not broaden significantly. These timelines are believed to origin from lamellar colonies that occupy a hard orientation with respect to the compression axis. Consequently, these grains accommodate a smaller fraction of the total strain and therefore show a lower defect density than the ones occupying a soft orientation. Rotation of these grains is facilitated by the plastic deformation of grains that surround them and are deformed more readily. Coarse lamellar colonies in hard orientations are likely to persist in the deformed microstructure, since the strains imposed are too small to induce recrystallization in the γ-phase. Most lamellar colonies in soft orientation, however, recrystallize more readily because of their higher defect density. It should be noted, at this point, that the strain imposed on a lamellar colony is not only dependent on its orientation, but also critically on its surrounding microstructural components.

From the appearance of the AT-plot (Figure 5) and the fact that most lamellar colonies were consumed during deformation (Figure 3b) it is concluded, that a significant fraction of the γ-phase undergoes DDRX during hot working at 1220 °C. Dynamic recovery occurs less readily due to the small SFE of γ (60-90 mJ/m2 [49]). Chraponski et al. [59] investigated a γ-TiAl based alloy which was hot-worked at 1000 °C by means of transmission electron microscopy and concluded that recrystallization as well as recovery occur in the γ-phase which is in excellent agreement with the present study. Additionally, this publication [59] points out that there is a significant degree of deformation inhomogeneity which is also confirmed by the current results.

4.4 Flow-curve

Generally, the shape of the flow-curve can be used to determine the restoration mechanisms that are operative during hot-deformation. Flow-curves recorded during the experiment are similar to those obtained with a Gleeble thermo-mechanical simulator (Figure 6). A common interpretation of flow-curves is based on their shape. Single-peak flow curves are indicative of dynamic recrystallization, whereas a constant flow stress is

associated with the occurrence of dynamic recovery (e.g. [50]). The flow curve obtained from the experiment performed at 1300 °C exhibits an approximately constant stress level until the temperature drops (Figure 6). This indicates that dynamic recovery processes are dominant, whereas the flow curve obtained at 1220 °C corresponds to the single-peak type indicating softening due to dynamic recrystallization. At 1300 °C, the HEXRD data show clear evidence that dynamic recovery occurs in both the α and β-phase which is in excellent accord with the observed shape of the flow-curve (Figure 6). Deformation at 1220 °C leads to a flow curve that exhibits significant flow-softening. By HEXRD, it was found that a large fraction of the lamellar colonies decompose and that the γ-phase recrystallizes dynamically. Furthermore, α-grains were shown to recrystallize at this temperature. Since only small fractions of β are present at this temperature (see Figure 1b), the shape of the flow curve is consistent with the findings of the HEXRD experiment.

Conclusion

In this paper, the hot-deformation behavior of a Ti-43.5 Al-4 Nb-1 Mo-0.1 B alloy was investigated in-situ by means of high-energy X-ray diffraction. Two compression experiments were conducted at 1300 °C in the (α+β) phase field region and at 1220 °C in the (α+β+γ) phase field region at a mean strain rate of 0.0037 s^{-1}. It was found that the α-phase predominantly dynamically recovers at 1300 °C, whereas dynamic recrystallization is observed for strains exceeding 0.25 at 1220 °C. For the β-phase, dynamic recovery was determined as the dominant process at both temperatures. The γ-phase dynamically recovers and recrystallizes at 1220 °C. By means of in-situ high-energy X-ray diffraction, it was also possible to directly observe the behavior of lamellar colonies which initially occupied a hard orientation with respect to the compression axis. Even though some of these colonies rotated during compression, they accommodated hardly any strain. Consequently, the defect density was too low to induce dynamic recrystallization and remnant colonies were found during post-mortem microstructural examinations. Results obtained by complementary investigation methods are in good agreement with the behavior observed in the diffraction experiments. In this study, in-situ methods were used to gain insight into the microstructural evolution during hot-working of a β-containing γ-TiAl based alloy. The obtained results yield important information for future alloy design strategies and for the optimization of industrial-scale hot-deformation processes of β containing γ-TiAl alloys.

Acknowledgements

The Australian participants acknowledge travel funding provided by the International Synchrotron Access Program (ISAP) managed by the Australian Synchrotron. The ISAP is funded by a National Collaborative Research Infrastructure Strategy grant provided by the Federal Government of Australia. We also appreciate the access and support of the ESTF management. The European experimentalist wishes to express gratitude for the ESRF travel support. Specimen material was provided by GfE Metalle und Materialien GmbH Nuremberg, Germany. We are grateful to Janny Lindemann for providing flow-curves obtained in hot-compression experiments at Brandenburgische Technische Universität Cottbus.

References

[1] Kim Y-W, Clemens H, Rosenberger A, Editors. Gamma Titanium Aluminides 2003. Warrendale, PA, USA: TMS, 2003.

[2] Yamaguchi M, Inui H, Ito K. Acta Mater. 2000;48:307-322.

[3] Appel F, Wagner R. Mater. Sci. Eng., R. 1998;22:187-268.

[4] Kestler H, Clemens H. Production, Processing and Application of γ(TiAl)-based Alloys. In: Leyens C, Peters M, Editors. Titanium and Titanium Alloys. Weinheim, Germany: WILEY-VCH, 2003. p. 351.

[5] Wu X. Intermetallics 2006;14:1114-1122.

[6] Cui WF, Liu CM, Bauer V, Christ H-J. Intermetallics 2007;15:675-678.

[7] Clemens H, Smarsly W. Adv. Mater. Res. 2011;278:551-556.

[8] Lasalmonie A. Intermetallics 2006;14:1123-1129.

[9] Loria EA. Intermetallics 2000;8:1339-1345.

[10] Clemens H, Wallgram W, Kremmer S, Güther V, Otto A, Bartels A. Adv. Eng. Mater. 2008;10:707-713.

[11] Clemens H, Chladil HF, Wallgram W, Zickler GA, Gerling R, Liss K-D, Kremmer S, Güther V, Smarsly W. Intermetallics 2008;16:827-833.

[12] Kremmer S, Chladil HF, Clemens H, Otto A, Güther V. Near Conventional Forging of Titanium Aluminides. In: Niinomi M, Akiyama S, Ikeda M, Hagiwari M, Maruyama K, Editors. Ti-2007 Science and Technology. Sendai, Japan: The Japan Institute of Metals (JIM), 2008. pp. 989-992.

[13] Wallgram W, Schmoelzer T, Cha L, Das G, Güther V, Clemens H. Int. J. Mater. Res. 2009;100:1021-1030.

[14] Rizzi N. Presentation at the Symposium “Structural Aluminides for Elevated Temperature Applications” New Orleans, LA, USA: TMS, 2008.

[15] Shi J-D, Pu Z, Zhong Z, Zou D. Scr. Mater. 1992;27:1331-1336.

[16] Tetsui T, Shindo K, Kaji S, Kobayashi S, Takeyama M. Intermetallics 2005;13:971-978.

[17] Tetsui T, Shindo K, Kobayashi S, Takeyama M. Intermetallics 2003;11:299-306.
[18] Tetsui T, Shindo K, Kobayashi S, Takeyama M. Scr. Mater. 2002;47:399-403.
[19] Appel F, Oehring M, Paul JDH, Klinkenberg C, Carneiro T. Intermetallics 2004;12:791-802.
[20] Liu B, Liu Y, Zhang W, Huang JS. Intermetallics 2011;19:154-159.
[21] Niu HZ, Chen YY, Xiao SL, Kong FT, Zhang CJ. Intermetallics 2011;19:1767-1774.
[22] Rao KP, Prasad YVRK, Suresh K. Materials & Design 2011;32:4874-4881.
[23] Rao KP, Prasad YVRK. Mater. Sci. Eng., A. 2010;527:6589-6595.
[24] Wang G, Xu L, Tian Y, Zheng Z, Cui Y, Yang R. Mater. Sci. Eng., A. 2011;528:6754-6763.
[25] Stark A, Schimansky FP, Clemens H. Solid State Phen. 2010;160:301-306.
[26] Witusiewicz VT, Bondar A, Hecht U, Rex S, Velikanova TYa. J. Alloys Compd. 2008;465:64-77.
[27] Clemens H, Boeck B, Wallgram W, Schmoelzer T, Droessler LM, Zickler GA, Leitner H, Otto A. Experimental Studies and Thermodynamic Simulations of Phase Transformations in Ti-(41-45)Al-4Nb-1Mo-0.1B Alloys. In: MRS Proceedings, Vol. 1128. Warrendale: MRS, 2008. pp. 115-120.
[28] Schmoelzer T, Liss K-D, Zickler GA, Watson IJ, Droessler LM, Wallgram W, Buslaps T, Studer AJ, Clemens H. Intermetallics 2010;18:1544-1552.
[29] Schloffer M, Iqbal F, Gabrisch H, Schwaighofer E, Schimansky F-P, Mayer S, Stark A, Lippmann T, Göken M, Pyczak F, Clemens H. Intermetallics 2012;22:231-240.
[30] Liss K-D, Garbe U, Li H, Schambron T, Almer JD, Yan K. Adv. Eng. Mater. 2009;11:637–640.
[31] Liss K-D, Yan K. Mater. Sci. Eng., A. 2010;528:11-27.
[32] Liss K-D, Schmoelzer T, Yan K, Reid M, Dippenaar R, Clemens H. J. Appl. Phys. 2009;106:113526.
[33] Saunders N. Phase Equilibria in Multi-Component γ-TiAl based Alloys. In: Kim YW, Dimiduk DM, Loretto MH, Editors. Gamma Titanium Aluminides 1999, TMS, Warrendale, PA 1999:183–194.
[34] Watson IJ, Liss K-D, Clemens H, Wallgram W, Schmoelzer T, Hansen TC, Reid M. Adv. Eng. Mater. 2009;11:932-937.
[35] Liss K-D, Bartels A, Schreyer A, Clemens H. Text. Microstr. 2003;35:219-252.
[36] Daniels JE, Drakopoulos M. J. Sync. Rad. 2009;16:463–468.
[37] Lindemann J. Hot-compression Tests of Intermetallic TiAl Alloys with the Gleeble Thermomechanic Simulator. Unpublished Results, Cottbus: 2010.
[38] Jakobsen B, Poulsen HF, Lienert U, Almer JD, Shastri SD, Sørensen HO, Gundlach C, Pantleon W. Science 2006;312:889-92.
[39] Warren BE. X-ray Diffraction. New York: Dover Publications, 1990.

[40] Margulies L, Winther G, Poulsen H. Science 2001;291:2392.
[41] Yan K, Liss K-D, Garbe U, Daniels JE, Kirstein O, Li H, Dippenaar R. Adv. Eng. Mater. 2009;11:771-773.
[42] Schmoelzer T, Liss K-D, Staron P, Mayer S, Clemens H. Adv. Eng. Mater. 2011;13:685-699.
[43] Reimers W, Pyzalla AR, Schreyer A. Neutrons and Synchrotron Radiation in Engineering Materials Science. Weinheim, Germany: WILEY-VCH, 2008.
[44] Rehrl C, Kleber S, Renk O, Pippan R. Mater. Sci. Eng., A. 2011;528:6163-6172.
[45] Vorhauer A, Hebesberger T, Pippan R. Acta Mater. 2003;51:677-686.
[46] Kim Y-W, Morris D, Yang R, Leyens C, editors. Structural Aluminides for Elevated Temperature Applications. Warrendale, PA, USA: TMS, 2008.
[47] Kim Y-W. Acta Mater. 1992;40:1121–1134.
[48] Inui H, Kishida K, Misaki M, Kobayashi M, Shirai Y, Yamaguchi M. Phil. Mag A 1995;72:1609-1631.
[49] Liu B, Liu Y, Li YP, Zhang W, Chiba A. Intermetallics 2011;19:1184-1190.
[50] Dieter GE. Mechanical Metallurgy. Boston: Mcgraw Hill Higher Education, 1989.
[51] Appel F, Kestler H, Clemens H. Forming. In: Westbrook JH, Fleischer RL, Editors. Intermetallic Compounds - Principles and Practice: Progress. Chichester, UK: John Wiley & Sons Ltd., 2002. pp. 617-642.
[52] Seetharaman V, Semiatin SL. Met. Mat. Trans. A 1996;27:1987-2004.
[53] Humphreys FJ, Hatherly M. Recrystallization and Related Annealing Phenomena. Pergamon Press Ltd., 2004.
[54] Leyens C, Peters M, Editors. Titanium and Titanium Alloys. Weinheim, Germany: Wiley-VCH, 2003.
[55] Raj S, Pharr GM. Mater. Sci. Eng. 1986;81:217-237.
[56] Orlová A. Mater. Sci. Eng., A. 1996;220:281-285.
[57] Blackburn MJ. In: Jaffee RI, Promisel NE, Editors. The Science, Technology and Application of Titanium. Oxford: Pergamon Press Ltd., 1970. p. 663.
[58] Liss K-D, Bartels A, Clemens H, Bystrzanowski S, Stark A, Buslaps T, Schimansky F-P, Gerling R, Scheu C, Schreyer A. Acta Mater. 2006;54:3721-3735.
[59] Chrapoński J, Rodak K. J. Microscopy 2006;223:298-301.

AIP | Journal of Applied Physics

Appendix E:
In-Situ Study of Dynamic Recrystallization and Hot-Deformation Behavior of a Multiphase Titanium Aluminide Alloy

K.-D. Liss, T. Schmoelzer, K. Yan, M. Reid, M. Peel, R. Dippenaar and H. Clemens

Journal of Applied Physics **106** (11), 2009, Art. No. 113526

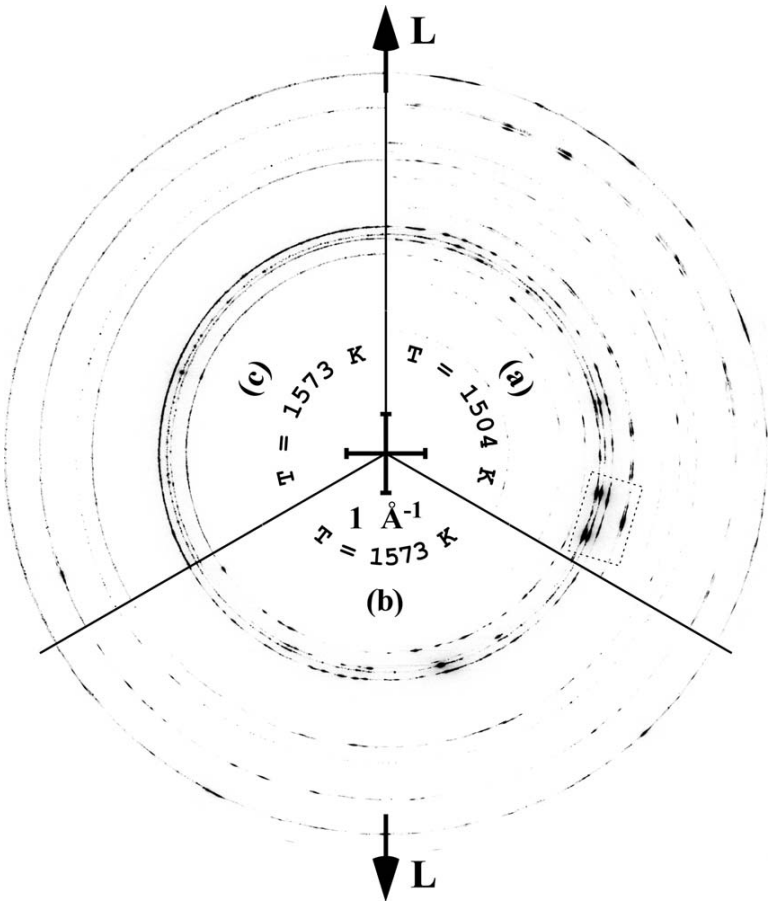

In situ study of dynamic recrystallization and hot deformation behavior of a multiphase titanium aluminide alloy

Klaus-Dieter Liss,[1,a] Thomas Schmoelzer,[2] Kun Yan,[1,3] Mark Reid,[3] Matthew Peel,[4] Rian Dippenaar,[3] and Helmut Clemens[2]

[1] *Australian Nuclear Science and Technology Organisation, PMB 1, Menai, New South Wales 2234, Australia*
[2] *Department of Physical Metallurgy and Materials Testing, Montanuniversität, A-8700 Leoben, Austria*
[3] *Faculty of Engineering, University of Wollongong, Wollongong, New South Wales 2522, Australia*
[4] *European Synchrotron Radiation Facility, BP 220, F-38043 Grenoble, France*

Received 14 September 2009; accepted 28 October 2009; published online 10 December 2009

Hot-compression tests were conducted in a high-energy synchrotron x-ray beam to study in situ and in real time microstructural changes in the bulk of a β-solidifying titanium aluminide alloy. The occupancy and spottiness of the diffraction rings have been evaluated in order to access grain growth and refinement, orientation relationships, subgrain formation, dynamic recovery, and dynamic recrystallization, as well as phase transformations. This method has been applied to an alloy consisting of two coexisting phases at high temperature and it was found that the bcc β-phase recrystallizes dynamically, much faster than the hcp α-phase, which deforms predominantly through crystallographic slip underpinned by a dynamic recovery process with only a small component of dynamic recrystallization. The two phases deform to a very large extent independently from each other. The rapid recrystallization dynamics of the β-phase combined with the easy and isotropic slip characteristics of the bcc structure explain the excellent deformation behavior of the material, while the presence of two phases effectively suppresses grain growth. © 2009 American Institute of Physics. [doi:10.1063/1.3266177]

I. INTRODUCTION

A sound understanding of plastic deformation and recrystallization in metals and intermetallics is a necessary prerequisite for the design and processing of materials with novel or improved physical properties like mechanical strength, heat resistivity, ductility,

formability, and so on. For example, it is desirable to develop intrinsically lighter and stronger materials for the transportation and aerospace industry, thereby reducing propulsion and energy costs. Intermetallic titanium aluminides are in the focus of research as they show enhanced mechanical strength at elevated temperatures and as such are good candidates to replace the heavy nickel based superalloys in specific components of aero- and automotive engines.[1–3] Although titanium aluminides exhibit attractive mechanical properties, they are not widely used due to difficult and expensive manufacturing routes.[3–5] This is, in large part, a consequence of the complex phase diagram of these alloys, possessing different regions of atomic order/disorder leading to different properties of the constituent phases. On the other hand, it is the form of the phase diagram that determines the strength of this type of material. At the intended application temperatures of 870–1020 K, simple TiAl based alloys exhibit a dual phase field of ordered hcp α_2-Ti_3Al ($D0_{19}$) and near-*fcc* γ-TiAl ($L1_0$) structures. The α_2-phase disorders at the eutectoid temperature ≈1453 K into hcp α, whereas the γ-phase disappears at the α-transus temperature of typical T≈1573 K. Accurate temperature values depend on the exact composition. It has been found that successful plastic deformation can be performed only in a narrow temperature range in the α+γ phase field.[4] In this narrow "deformation window," phase fractions vary strongly with temperature,[6] and it is difficult to control the hot-working process.[4,5] Deformation can also be performed above the α-transus, but this leads to crystalline anisotropy of the hexagonal system and the associated texture formation. In addition, rapid grain growth occurs at these temperatures, thereby excluding this temperature range for production purposes. To circumvent these drawbacks, an approach is taken whereby the bcc β-Ti phase is stabilized at high temperatures, which is known to both deform easily and show less anisotropy than the hcp α-Ti phase.[7] A single β-phase field region at high temperature is not desired because of grain coarsening.[8] In order to overcome these problems, the so-called TNM™ alloy of nominal composition Ti-43.5Al-4Nb-1Mo-0.1B (composition in atomic percent) was developed.[9] The alloy solidifies through the β-phase and exhibits a wide α+β-phase field in which hot-working can be conducted on an industrial scale. For example, an excellent forgeability in the α+β-phase field has been reported.[10] The phase diagram for TNM alloy was established[11] and refined recently by *in situ* neutron diffraction.[12] *In situ* high-temperature laser scanning confocal microscopy proved the slow kinetics of grain growth in the high temperature α+β phase field region,[12] where the material is soft and ductile. A more comprehensive account of TNM alloys is given by Clemens and co-workers.[9,10,13]

The aim of the present study is to obtain *in situ* and in real time information from the bulk of the Ti-43.5Al-4Nb-1Mo-0.1B alloy during hot compression. The starting poly-crystalline microstructure consists of lamellar γ/α_2 colonies with globular γ-grains and ordered β_0-grains containing γ-precipitates with a grain size of about 100 μm. The recently developed high-energy synchrotron x-ray diffraction method[14] combined with the

evaluation of the morphology of the diffraction Debye–Scherrer rings[15,16] is applied to a multiphase alloy undergoing hot plastic deformation. This allows the evaluation of grain size statistics[17] such as growth and refinement, subgrain formation,[18] lattice strain,[19] grain orientations, orientation relationships between grains and phases,[20] grain rotations,[21] texture evolution,[16] mechanisms of phase transformations,[22] dynamic recovery, and dynamic recrystallization.[15]

II. EXPERIMENTAL

The experiment was performed at the beamline ID15b of the European Synchrotron Radiation Facility (ESRF)[14,23] using high-energy x-rays of 86.94 keV corresponding to an incident wave number k=44.03 Å^{-1} and wavelength λ=0.1427 Å. The Ø≈100 µm beam transmits the Ø 4 mm sample and is diffracted from its crystallites into Debye-Scherrer rings on a detector in 1233.8 mm distance from the sample center. The relatively small number of crystallites in the illuminated volume leads to spottiness on the Debye-Scherrer rings, which should be avoided in conventional powder diffraction but plays an essential role in the present investigation. The fast Pixium 4700 flat-panel detector[24] was employed for real time data acquisition at ≈2 Hz. The wirecut, 4 mm diameter, 8 mm high cylindrical sample was deformed in an Instron electrothermomechanical tester for simulating thermomechanical processing. In the present configuration, loads up to 3000 N can be applied while the specimen is heated resistively with a maximum power angle of 8 V and 450 A. Dedicated high-temperature compression anvils were produced from a special molybdenum alloy (TZM). In addition, graphite and tantalum foils were inserted between the anvil faces and the sample. This arrangement assured good electric contact, provided lubrication between the sample and anvil (graphite), and prevented diffusion of carbon into the specimen (tantalum). The load axis was horizontally perpendicular to the incident beam and translation scans have been taken to align accurately the center of the sample with the center of the beam. A regulation loop was implemented to keep the centers in coincidence during compression before any diffraction image was taken. The mean detector distance was calibrated by recording two diffraction patterns in different distances and using triangulation, while the x-ray energy was calibrated with a CeO_2 standard. The process parameters were a heat ramp of 9.5 K/s up to the maximum temperature of 1573 K after 145 s. This temperature was chosen to ensure the compatibility of the results to the findings published in Ref. [10]. After 35 s hold, a constant compression rate of 0.021 mm/s was applied (strain rate of ≈$2.6\cdot10^{-3}$ s^{-1}). After compressing for 45 s (≈1 mm, 12.5% strain), the deformation was interrupted for 22 s in order to study relaxation. Compression was then continued and after a further 153 s (≈4.15 mm, 52% strain) when the applied load was 410 N, the temperature regulation system became unstable (maximum power reached due to the increasing cross section of the sample) and the temperature began to drop resulting

in the applied load increasing rapidly to 1103 N some 40 s later. At this time, the machine safety tripped and the jaws rapidly returned to their starting positions loosing the sample from the beam. The temperature was measured by a R-type thermocouple spot welded on the central circumference of the cylinder outside the beam cross section.

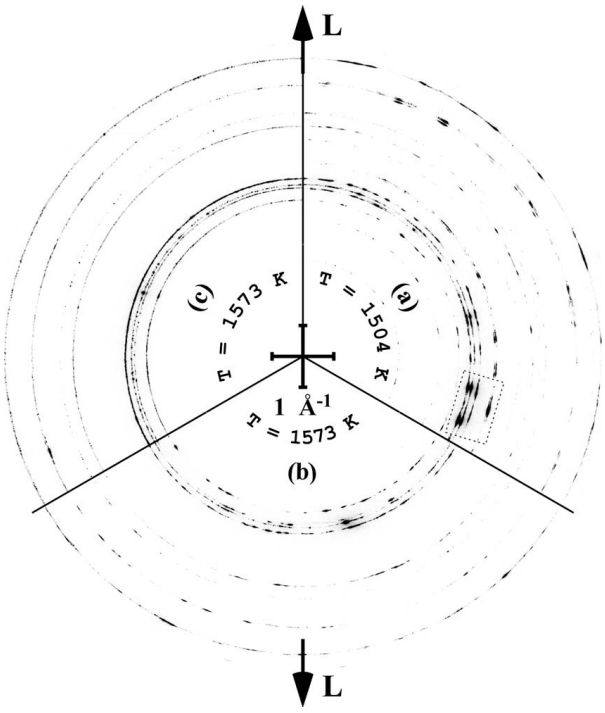

FIG. 1. Representative parts of the acquired diffraction rings compiled in three sectors: (a) below the alpha transus temperature T_α, showing α-, β-, and γ-phases in coexistence; (b) above T_α, where γ disappeared before plastic deformation and (c) above T_α during plastic deformation. Reflections in the indicated box in (a) reveal orientation correlations of all three phases. The common ring center is marked with a crossed scale bar of 1 $Å^{-1}$ and the longitudinal load direction L is indicated. Reflections are indexed in Fig. 2.

III. RESULTS AND DISCUSSION

Figure 1 shows experimentally obtained diffraction patterns as an assembly of three sectors (a) at T=1504 K, below the α-transus temperature (T_α=1555 K), (b) above T_α, before and (c) during deformation [T=1573 K for both (b) and (c)]. The reflections are indexed in Fig. 2, which represents, in color scale, the azimuthally integrated diffraction rings against the scattering vector (radial direction of the rings) and time. The experimental parameters are depicted on the same time axis to the right of the graph. The pattern at 1504 K in Fig. 1(a) shows rings stemming from all three coexistent phases, α, β, and γ. The γ-TiAl phase disappears at T_α and only reflections from the α-and β-phase remain in the 1573 K sectors (b) and (c). There are also correlations between the α-, β-, and γ-reflections expressed by

intensity agglomerations at equal or nearby azimuthal angles, confirming the Blackburn orientation correlation between α- and γ-phase in Fig. 1(a) (Refs. 20 and 25), as well as the Burgers orientation correlation between α- and β-phase in Figs. 1(a) and 1(b).[15,26] Additionally, the box in Fig. 1(a) shows the orientation correlations between all three phases where the γ-002/200 spot aligns in a triangle with α-101, β-110, and α-002.[22] The time evolution of the azimuthally integrated patterns in Fig. 2 shows the effect of thermal expansion, moving the reflections to smaller scattering vectors upon heating. There are some weak superstructure reflections disappearing halfway through the heating ramp, which correspond to the ordered α_2 and β_0 phases.[12] The disappearance of the γ-TiAl phase determines the α-transus temperature which was determined as T_α=1555 K in agreement with earlier reported values.[12,13] This good agreement provides convincing experimental evidence of the accuracy of the present experiment.

The data is represented in Fig. 3, where the intensity distribution along a certain diffraction ring is plotted in grayscale as a function of azimuthal angle and time. To produce this representation of the diffraction data, the full circle of a Debye–Scherrer ring from Fig. 1 is cut at the six o'clock position and straightened into one horizontal line from 0 to 360° of Fig. 3 at any given time. A 20° cyclic extension is plotted at either side of the range in order to evaluate features in this orientation range. Directions longitudinal (*L*) and transverse (*T*) to the load axis are indicated at the top of the figure. The vertical time axis is the same as in Fig. 2 and the experimental parameters are reproduced for reference.

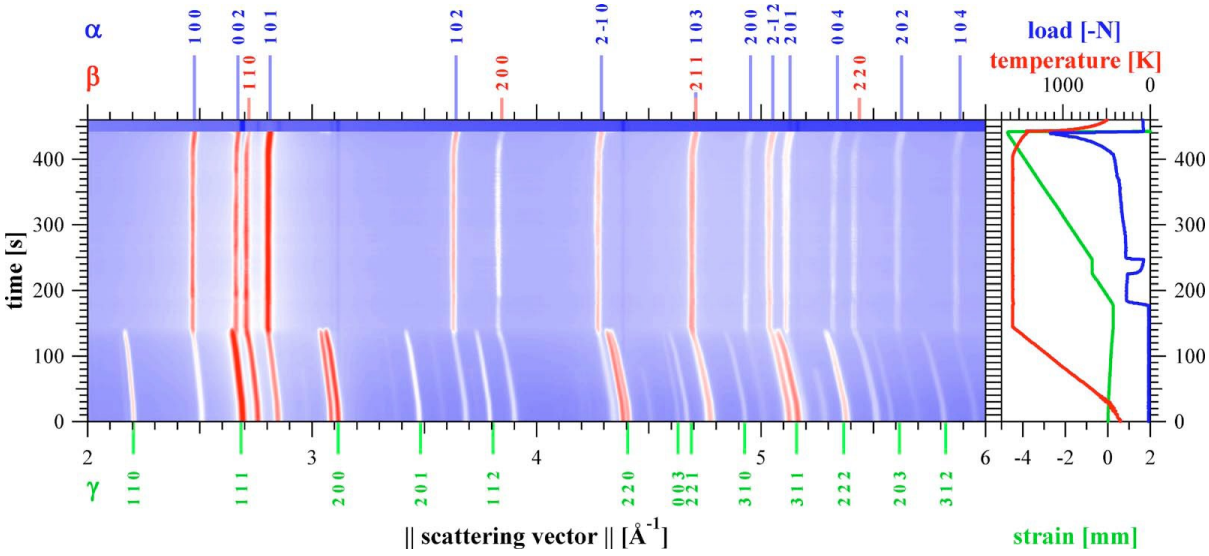

FIG. 2. Color coded powder diffraction patterns obtained by azimuthal integration of the time frames in Fig. 1 vs scattering vector $q=4\pi/\lambda \sin(2\vartheta/2)$ on the abscissa evolving in time on the ordinate to the left. Because of the tetragonality of γ-TiAl (L10 structure), some reflections appear as double lines. For simplification, however, indices are given for a fcc lattice. The deformation parameters (compressive mode) are given to the right.

The azimuthal-angle-time plots (AT-plots) allow the time evolution of reflections in orientation space to be tracked. In principle, each line is a one-dimensional manifold section from a conventional pole figure.[16] When not overlapping, the number of spots on a selected ring at any one time represents the number of crystallites matching the Ewald sphere for the Laue condition. Therefore, in the case of a fixed illuminated volume, the number of spots is somehow inversely proportional to the crystallite size raised to a certain power for multiple dimensions. Further, a sharp reflection stemming from a perfect crystallite has a lower probability of hitting the Ewald sphere than a broad reflection with large mosaic spread evolving from lattice distortions such as dislocations and subgrain cells. In short, the number of diffraction spots increases with smaller grain size and larger mosaic spread. In addition to these microstructural parameters, symmetry plays a role for the number of observable spots, and, hence, it is also proportional to the multiplicity of the reflections. The evolution of an individual reflection spot in the AT-plot is called a timeline. Particular features of timelines are shown in Fig. 4 as zoomed regions of interest extracted from Fig. 3.

Considering first the heating part of the experimental cycle, apart from minor intensity changes, AT-plots of the α-phase in Fig. 3 stay very stable until the α-transus is reached. This implies that there is no major evolution in grain size nor in mosaic spread and the overall microstructure remains intact. While the γ-111 timelines disappear at T_α, the α-reflections augment intensity due to the increase of the total phase fraction of α-Ti and there is no further evolution of the morphology. The number of timelines observed in the individual reflections corresponds well to the ratio of their multiplicities which are 6, 2, 12 for α-100, α-002, and α-101, and 12, 6 for β-110 and β-200, respectively. This can be best viewed after the γ-phase disappeared in Fig. 3, for example, by regarding a cut at time 160 s and statistically counting the number of intensity maxima.

The β-phase behaves differently upon approaching T_α and holding at a temperature just above T_α. The timelines sharpen and become spotty and interrupted and their overall distribution diminishes, meaning the density of Bragg spots fluctuates and shrinks. This can be interpreted as a grain recovery process and sharpening of mosaic spread. The driving force for this process is probably due to transformation induced stresses. As the temperature was raised quickly with respect to the transformation kinetics of the system, on-going rearrangements of the α- and β-phases take place, particularly influencing the minority β-phase.[9,10]

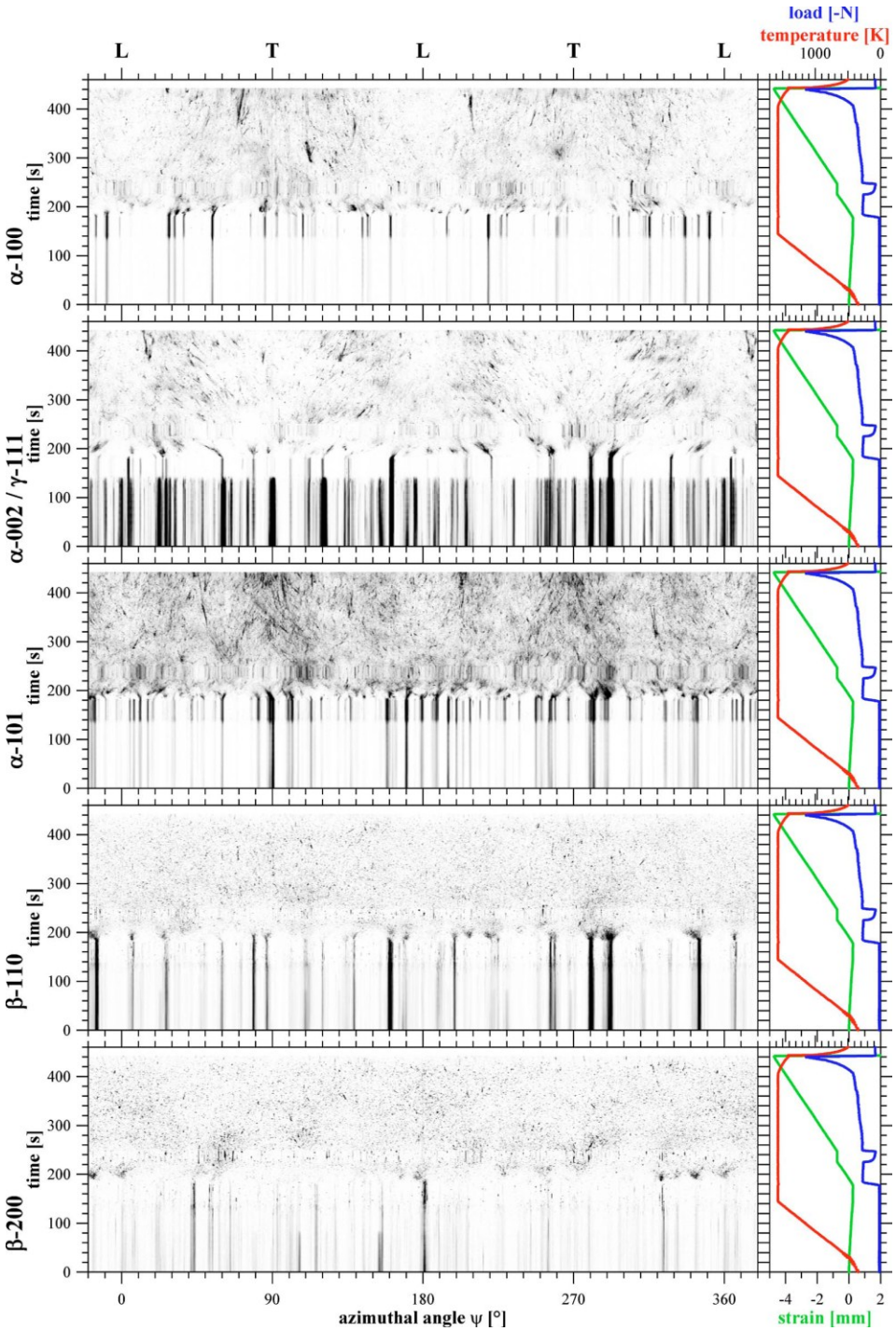

FIG. 3. AT-plots of the first three α- and two β-reflections. The α-002 and γ-111 reflections overlap and cannot be separated until the γ-phase disappears at the α-transus temperature. The orientations of the grains evolve rapidly upon the application of strain but are otherwise stable, as indicted by the deformation parameters to the right of each plot. Longitudinal and transverse load directions, L and T, respectively, are given at the top of the azimuthal-angle axis. Zoomed regions of interest are shown in Fig. 4.

Considering the deformation part of the experimental cycle on the β-phase, upon the onset of plastic deformation at t=180 s, timelines of the β-phase spread out rapidly into a larger angular range, which can be recognized, for example, on the intense timelines around azimuth ψ=280°and ψ=290° on the AT-plots of β-110. Other outbursts in orientation space seem to occur at angular positions where previously no or little intensity was observed, such as at ψ=340° on β-200, as emphasized in Fig. 4(c). During the cold deformation of a metal, these broadenings stem from the breakdown of grains into subgrains with a continuous mosaic spread ending up in grain refinement and deformation texture of the material.[16] The appearance of the outbursts from apparently nothing are the evolution of mosaic spread from grain orientations nearby, but not matching the Ewald sphere, which moves into the reflection condition as their angular distribution broadens.[16] Upon hot deformation, however, dynamic recovery concurs with the grain breakdown forming a spotty mosaic distribution: Agglomeration of distorted subgrains recover to more perfect subgrains which are then separated by a subgrain boundary representing a small-angle boundary.[15] Soon after subgrain formation, the intensity is spread all over the rings, and, hence, grains and subgrains cannot be distinguished any longer. Dynamic recrystallization, a process in which new grains, separated by large-angle boundaries, are formed from a highly distorted microstructure, is experimentally observed by the popping up and disappearance of reflections.[15] Some of the short timelines show fluctuations of dynamic recovery aligned in strings which are inclined in the AT-plot due to a grain rotation process.[16] Sometimes, regions of slightly preferred orientation occur on a 10° scale in azimuthal angle, which indicates that there is an underpinning orientational preference upon dynamic recrystallization.[15] The global texture of the β-phase, however, is very weak.

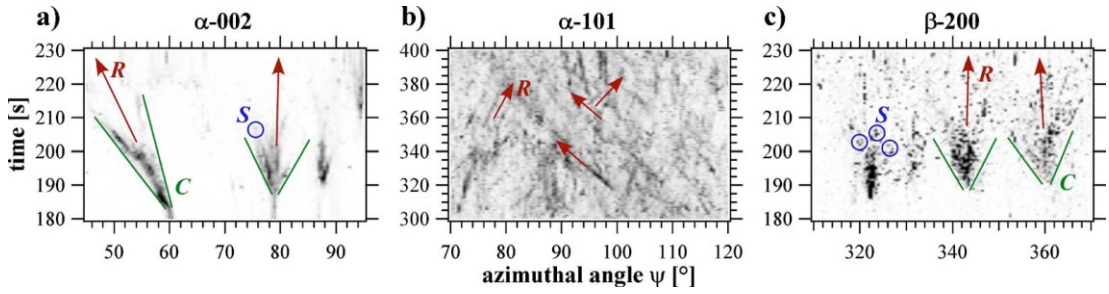

*FIG. 4. Extracts from the AT-plots of Fig. 3, showing typical features of timelines. A conical shape **C** represents an increase of mosaic spread caused by angular broadening through subgrain formation. The mean inclination **R** of the timeline characterizes grain rotation. Timelines may appear spotty, **S**, due to recovery of subgrains and their fluctuations. Predominant slip deformation, crossing of rotation vectors and strong initial dynamic recovery effects are demonstrated in (a), (b), and (c), respectively.*

Recovery and recrystallization during deformation are considerably slower in the α-phase than in the β-phase. Upon the onset of plastic deformation, the creation of mosaic spread behaves much smoother, almost as observed in cold deformed copper,[16] as seen in Fig. 4(a). Although it occurs, dynamic recovery is strongly reduced, and large grain rotations expressed by tilted timelines occur throughout a slip deformation process. There is a high degree of preferred orientation at the end of the experiment: The prismatic α-100 orientation distribution peaks in the *T* directions and has a minimum along *L*, while the basal α-002 orientation has minima at *T* and *L* peaking at *L*35°, indicating a tilted basal fiber texture.[27] Grains initially in arbitrary orientations rotate into these preferred orientations. As an example, the timeline starting at ψ=60° of α-002 rotates strongly to the left [Fig. 4(a)] and the one at ψ=120° to the right, in a symmetric way away from *T*. A timeline starting close to the texture maximum or minimum orientations does not show rotation but large angular spreading as can be seen at ψ=25° and ψ=79° [Fig. 4(a)] in α-002 or in the *T* and *L* directions in α-100. The α-101 orientation exposes high multiplicity and has components of both basal and prismatic orientations. Therefore, the inclination of the timeline depends on which of the equivalent slide systems are activated and thus can rotate this particular reflection plane, which is an inclined projection of the simple rotation vector into the left or right direction. This leads to over-crossing timelines, as seen, for example, in Fig. 4(b). Similar timeline crossings are seen occasionally in α-100 and α-110, but less in α-002, indicating that α-002 has a rotation axis along the beam axis and the basal slip system is well activated. The tilted basal fiber texture is another indication for slip deformation as deformation dominated by twinning would drive the texture maximum into the *L* direction. Other than in the cold deformation process,[16] dynamic recovery takes place when the mosaic spread becomes too large or when grain rotation takes place at a particularly high rate. The widely spread subgrains then become new, perfect grains by themselves which subsequently deform and rotate independently in the polycrystalline matrix. Highly uncorrelated dynamic recrystallization plays a minor role in the deformation of the α-phase. Indeed, dynamic recovery in commercial pure titanium has been suggested as a dominant deformation process under certain conditions.[28]

The different behavior of the α- and β-phases is demonstrated as well in the holding cycle starting at time 225 s, where the displacement was stopped for 22 s. The timelines of the α-phase remain mostly static while the β-phase still shows many fluctuations. The observed behavior is attributed to a relaxation effect, as seen in the load curve in Fig. 3, occurring mostly in the β-phase.

IV. CONCLUSION

In conclusion, we have followed *in situ* and in real time the plastic deformation in the bulk of an advanced intermetallic Ti-43.5Al-4Nb-1Mo-0.1B alloy at 1573 K. The recently developed combination of rapid two-dimensional high energy x-ray diffraction with advanced analysis of the spottiness of the diffraction rings has been presented and applied to the investigation of a multiphase alloy. Orientation relationships between the phases were identified upon static heating indicating at least three different components, namely, the Blackburn orientation correlation between the α- and the γ-phase typical for γ-based titanium aluminides,[25] the Burgers orientation correlation occurring in hcp↔bcc transformations[26] and a recently reported orientation correlation between the α-002, α-101, and γ-002/200 reflections.[22] The hcp α-phase deforms preferentially by slip rather than by twinning, superimposed by a relatively slow dynamic recovery and a less important dynamic recrystallization process. This leads to a tilted basal fiber deformation texture. In contrast, the bcc β-phase is driven by rapid fluctuations in orientation space, which start below the α-transus temperature during heating and continue during holding at the deformation temperature before the compression test is started. The high activity of the β-phase gives raise to rapid dynamic recovery and dynamic recrystallization which basically overwrites almost any deformation texture of this phase. It is interesting to note that there is no major coupling between the orientations and the deformation processes of the α- and the β-phase, and it appears that each grain behaves individually, self-consistently in a polycrystalline matrix. The coexistence of α- and β-phases hinders rapid grain growth as opposed to that observed in alloys with a single-phase field. The high rate of dynamic recovery and recrystallization occurring within β-grains render TNM alloys favorable for thermomechanical processing.

ACKNOWLEDGMENTS

The Australian participants acknowledge travel funding provided by the International Synchrotron Access Program (ISAP) managed by the Australian Synchrotron. The ISAP is funded by a National Collaborative Research Infrastructure Strategy grant provided by the Federal Government of Australia. We also appreciate the access and support of the ESRF management, User Office, and beamline staff. The European experimentalist wishes to express thanks for the ESRF travel support. Sample materials were provided by GfE Metalle und Materialien GmbH, Nuremberg, Germany and Bohler Schmiedetechnik GmbH & CoKG, Kapfenberg, Austria. The authors thank Wilfried Wallgram for helpful discussions.

REFERENCES

[1] E. A. Loria, Intermetallics **8**, 1339 (2000).

[2] W. Smarsly, H. Baur, G. Glitz, H. Clemens, T. Khan, and M. Thomas, "Titanium Aluminides for Automotive and Gas Turbine Applications," in *Structural Intermetallics*, edited by K. J. Hemker, D. M. Dimiduk, H. Clemens, R. Darolia, H. Inui, J. M. Larsen, V. K. Sikka, M. Thomas, and J. D. Whittenberger (The Minerals, Metals and Materials Society, Warrendale, 2001), pp. 25–34.

[3] X. H. Wu, Intermetallics **14**, 1114 (2006).

[4] S. Kremmer, H. F. Chladil, H. Clemens, A. Otto, and V. Güther, in *Ti-2007 Science and Technology*, edited by M. Niinomi, S. Akiyama, M. Hagiwari, M. Ikeda, and K. Maruyama (The Japan Institute of Metals, Sendai, 2007), pp. 989–992.

[5] F. Appel and M. Oehring, in *Titanium and Titanium Alloys*, edited by C. Leyens and M. Peters (Wiley-VCH, Weinheim, 2003), pp. 89–152.

[6] L. A. Yeoh, K.-D. Liss, A. Bartels, H. F. Chladil, M. Avdeev, H. Clemens, R. Gerling, and T. Buslaps, Scr. Mater. **57**, 1145 (2007).

[7] A. Stark, A. Bartels, R. Gerling, F. P. Schimansky, and H. Clemens, Adv. Eng. Mater. **8**, 1101 (2006).

[8] D. Phelan, M. Reid, N. Stanford, and R. Dippenaar, JOM **58**, 67 (2006).

[9] H. Clemens, W. Wallgram, S. Kremmer, V. Guther, A. Otto, and A. Bartels, Adv. Eng. Mater. **10**, 707 (2008).

[10] W. Wallgram, T. Schmölzer, L. Cha, G. Das, V. Güther, and H. Clemens, Int. J. Mater. Res. **8**, 1021 (2009).

[11] H. Clemens, B. B. Böck, W. Wallgram, T. Schmölzer, L. M. Drössler, G. A. Zickler, H. Leitner, and A. Otto, Mater. Res. Soc. Symp. Proc. **1128**, 451 (2009).

[12] I. J. Watson, K. D. Liss, H. Clemens, W. Wallgram, T. Schmoelzer, T. Hansen, and M. Reid, Adv. Eng. Mater. **11**, 932 (2009).

[13] H. Clemens, H. F. Chladil, W. Wallgram, G. A. Zickler, R. Gerling, K. D. Liss, S. Kremmer, V. Güther, and W. Smarslyg, Intermetallics **16**, 827 (2008).

[14] K.-D. Liss, A. Bartels, A. Schreyer, and H. Clemens, Textures Microstruct. **35**, 219 (2003).

[15] K.-D. Liss, U. Garbe, H. Li, T. Schambron, J. D. Almer, and K. Yan, Adv. Eng. Mater. **11**, 637 (2009).

[16] K. Yan, K.-D. Liss, U. Garbe, J. Daniels, O. Kirstein, H. Li, and R. Dippenaar, Adv. Eng. Mater. **11**, 771 (2009).

[17] S. E. Offerman, N. H. Van Dijk, J. Sietsma, S. Grigull, E. M. Lauridsen, L. Margulies, H. F. Poulsen, M. T. Rekveldt, and S. Van Der Zwaag, Science **298**, 1003 (2002).

[18] B. Jakobsen, H. F. Poulsen, U. Lienert, J. Almer, S. D. Shastri, H. O. Sorensen, C. Gundlach, and W. Pantleon, Science **312**, 889 (2006).

[19] J. Böhm, A. Wanner, R. Kampmann, H. Franz, K.-D. Liss, A. Schreyer, and H. Clemens, Nucl. Instrum. Methods Phys. Res. B **200**, 315 (2003).

[20] K.-D. Liss, A. Bartels, H. Clemens, S. Bystrzanowski, A. Stark, T. Buslaps, F.-P. Schimansky, R. Gerling, C. Scheu, and A. Schreyer, Acta Mater. **54**, 3721 (2006).

[21] L. Margulies, G. Winther, and H. F. Poulsen, Science **291**, 2392 (2001).

[22] K. D. Liss, A. Stark, A. Bartels, H. Clemens, T. Buslaps, D. Phelan, and L. A. Yeoh, Adv. Eng. Mater. **10**, 389 (2008).

[23] T. Tschentscher and P. Suortti, J. Synchrotron Radiat. **5**, 286 (1998).

[24] J. E. Daniels and M. Drakopoulos, J. Synchrotron Radiat. **16**, 463 (2009).

[25] M. J. Blackburn, in *The Science, Technology and Application of Titanium*, edited by R. I. Jaffee and N. E. Promisel (Pergamon Press Ltd., Oxford, 1970), p. 633–643.

[26] W. G. Burgers, Physica (Amsterdam) **1**, 561 (1934).

[27] A. Stark, A. Bartels, F.-P. Schimansky, and H. Clemens, in *Advanced Intermetallic-Based Alloys*, edited by Jörg Wiezorek, Chong Long Fu, Masao Takeyama, David Morris, and Helmut Clemens (Mater. Res. Soc. Symp. Proc. 980, Warrendale, PA, 2007), 0980-II07-01.

[28] Z. P. Zeng, Y. S. Zhang, and S. Jonsson, Mater. Sci. Eng., A **513–14**, 83 (2009).

ADVANCED ENGINEERING MATERIALS

Appendix F:
In-Situ Synchrotron Study of B19 Phase Formation in a TiAl Alloy

T. Schmoelzer, A. Stark, E. Schwaighofer, T. Lippmann, S. Mayer and H. Clemens.

Provisionally accepted at Advanced Engineering Materials

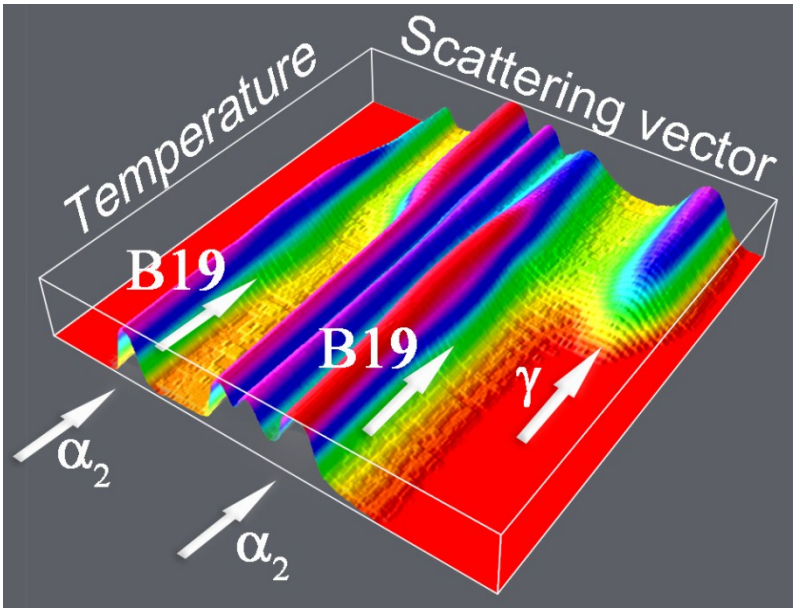

In-situ synchrotron study of B19 phase formation in an intermetallic γ-TiAl alloy**

By *T. Schmoelzer**, *A. Stark*, *E. Schwaighofer*, *T. Lippmann*, *S. Mayer*, and *H. Clemens*

[*] *T. Schmoelzer, E. Schwaighofer, Dr. S. Mayer, Prof. Dr. H. Clemens*
Department Physical Metallurgy and Materials Testing,
Montanuniversität Leoben, 8700 Leoben, (Austria)
E-mail: thomas.schmoelzer@unileoben.ac.at
Dr. A. Stark, Dr. T. Lippmann
Institute of Materials Research,
Helmholtz-Zentrum Geesthacht, 21502 Geesthacht, (Germany)

[**] *The support of DESY management, User Office and HZG beamline staff is highly acknowledged. Research activities leading to the presented HEXRD results received funding from the European Community's Seventh Framework Programme (FP7/2007-2013) under grant agreement n°226716. A part of this project was conducted within the framework of the BMBF project O3X3530A, Germany and the Styrian Materials Cluster, Austria.*

A multitude of phases exists in the binary Ti-Al phase diagram and even greater numbers are formed in structural TiAl alloys, which contain additional alloying elements to improve their properties. In the current study, a Ti-45 Al-3 Mo-0.1 B (in at%) alloy was investigated with respect to the phases occurring in chemical non-equilibrium. In-situ high energy X-ray diffraction experiments enabled to identify a transient phase to be of the B19 type and to determine its temperatures of formation and dissolution.

Introduction

As there is increasing pressure on manufacturers to produce more efficient and lightweight aircraft engines, new material classes are considered for structural components. Among the prime candidates to replace dense Ni-based super-alloys in the low pressure turbine are materials in the Ti-Al alloy system.[1] A range of alloying elements is used to adjust their properties and among them is Mo, a strong stabilizer of the β/β_o-phase.[2, 3] This phase is of great technological importance due to its beneficial effects on the solidification and hot-deformation behavior of γ-TiAl alloys. For further information on the role of β/β_o-phase in γ-TiAl based alloys, the reader is referred to.[4, 5]

To improve the understanding of the effects of Mo addition to γ-TiAl based alloys, an alloy with a nominal composition of Ti-45 Al-3 Mo-0.1 B (in at%) was produced. The phases occurring in this alloy were studied by means of in-situ high-energy X-ray diffraction (HEXRD) over a wide temperature range.[6] Based on these results and available literature

data[7], a phase diagram was constructed. In technological processes, however, high heating and cooling rates are frequently used. Therefore, the materials behavior under non-equilibrium conditions is investigated in the present study.

In equilibrium conditions, the phases α_2 ($D0_{19}$, P63/mmc), β_o (B2, Pm-3m) and γ ($L1_0$, P4/mmm) co-exist at room temperature. At high temperatures, α_2 and β_o disorder to α (A3, P63/mmc) and β (A2, Im-3m), respectively. The transformation temperatures are 1205 °C for $\alpha_2 \rightarrow \alpha$ and ~1230 °C for $\beta_o \rightarrow \beta$.[8] Details on the phase diagram can be found in.[6, 7] In addition to these main constituents, several phases with lower symmetry are mentioned in literature. Among these are hexagonal ω-related phases [9] and orthorhombic phases.[10, 11] Abe et al. [10] reported on an orthorhombic phase with B19 structure (Pmma) that forms very fine precipitates upon rapid cooling in a Ti-48 Al alloy. Tanimura et al. [12] observed the formation of B19-phase as a metastable transitional phase in the $A3 \rightarrow D0_{19}+L1_0$ precipitation sequence. Here also small regions of B19 were formed in the α/α_2 matrix upon quenching of a Ti-40 Al alloy from 1250 °C which acted as nucleation sites for γ-phase formation during a subsequent annealing step at 1000 °C. Appel et al. [11] observed B19 phase in Ti-(40-44) Al-8.5 Nb alloys after extrusion at 1250 °C and a subsequent heat-treatment at 1030 °C. Although the existence of the B19 phase in the TiAl system has been well established, no detailed information on the chemical or temperature regime in which the B19 phase forms in these alloys is available as yet.

It should be noted that the B19-phase is structurally closely related to the α/α_2, γ and β/β_o phases.[13] **Figure 1 a** shows a hexagonal closest packed with atoms of only one kind which corresponds to the {0001} plane of the disordered α-Ti(Al) phase. **Figures 1 b** and **c** show closest packed planes containing two atomic species with compositional ratios of 3:1 or 1:1, similar to the {0001} plane in α_2-Ti_3Al and the {100} plane in B19-TiAl, respectively. All three phases exhibit the stacking sequence ...ABAB... corresponding to a hexagonal closest packed structure. Nonetheless, the B19 structure possesses an orthorhombic symmetry due to the fact that the two atomic species are arranged in alternating lines (**Figure 1 c**). It should be mentioned, however, that the B19 lattice is only slightly distorted as compared with an ideal hexagonal lattice.

It is interesting also to note that the atoms in the closest packed plane of γ-TiAl (i.e. the {111} plane) are arranged in the same way as in the {100} plane of the B19 structure (Figure 1 c), but contrary to B19, the $L1_0$ structure exhibits the stacking sequence ...ABCABC... Also in β_o-TiAl, the atomic arrangement in the closest packed plane (which is the {110} plane) corresponds to that of the {100} plane of B19 (Figure 1 c). The structural relationship between B19 and β_o is similar to that between α and β-Ti.

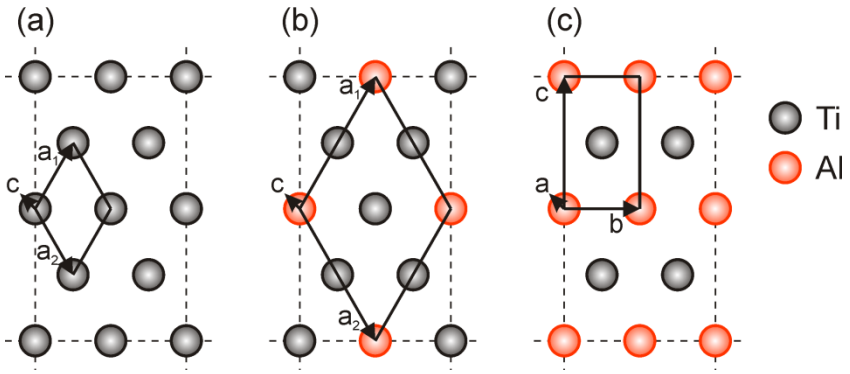

Figure 1: *Structural relations between the individual phases in TiAl alloys illustrated by sections of their closest packed planes. (a) {0001} α-Ti(Al), (b) {0001} α_2-Ti_3Al, and (c) {100} B19-TiAl. The dimensions of the unit cells of α-Ti(Al), α_2-Ti_3Al, and B19-TiAl are marked by solid lines. It should be noted that (a) also corresponds to {110} β-Ti(Al) and (c) also corresponds to {111} γ-TiAl as well as {110} β_o-TiAl.*

Experimental

The phases occurring under non-equilibrium conditions in a Ti-44.58 Al-3.23 Mo-0.12 B alloy were investigated by means of in-situ HEXRD experiments at the HARWI II beamline of the DESY synchrotron in Hamburg, Germany.[14] Details on ingot production, phase diagram and original microstructure can be found in.[6, 7] A beam of monochromatic synchrotron radiation with a mean energy of 100 keV and a cross-section of 1x1 mm^2 was used for diffraction experiments. Heating of the cylindrical specimens with a diameter of 5 mm and a length of 15 mm was performed by a modified Bähr DIL 805A/D dilatometer.[15] Temperature was controlled by an S-type thermocouple. Note that the temperatures given in this paper are rounded to 5 °C steps. A mar555 detector (marresearch, Norderstedt, Germany) recorded the diffraction patterns at a distance of 1837 mm from the specimen position. Integration of the diffraction patterns was performed within the fit2D software package.[16] The software PowderCell was employed for Rietveld fitting.

Prior to the in-situ experiment, the specimens were heat treated at 1450 °C for 30 min and subsequently water quenched. This resulted in a $\alpha_2+\beta_o$ microstructure where the α_2-phase formed rapidly during cooling and it is in a chemical non-equilibrium. Due to the suppression of γ-phase formation, the α_2-phase is highly supersaturated in Al. Heating during the HEXRD experiments was performed continuously at rates of 25 °C/min and 2 °C/min.

Results and Discussion

Employing HEXRD allowed for in-situ monitoring the phases evolution. A series of selected diffractograms recorded during heating at 2 °C/min is presented in **Figure 2**. The first pattern acquired at 565 °C features single peaks of the α_2 and β_o-phase as indexed in Figure 2. At this temperature, the phase fractions as determined by means of Rietveld analysis are approximately 80 vol% α_2 and 20 vol% β_o. As temperature rises, the 20-2l and 22-4l α_2 peaks begin to split. This is most obvious for the 20-20 and 22-40 peaks at 640 °C where the separation between the original and the newly emerged reflection reaches its maximum. As the temperature is increased further, the peak splitting gradually diminishes until a single peak is visible again at 715 °C. Within this temperature interval, also the intensity of the γ-peaks changes significantly. Starting with low intensities below 640 °C, a gradual gain in intensity with increasing temperature is observed. Simultaneously, the intensity of the α_2 reflections is abating. A phase composition of about 35 vol% α_2, 20 vol% β_o, and 45 vol% γ is attained at the highest temperature of 715 °C.

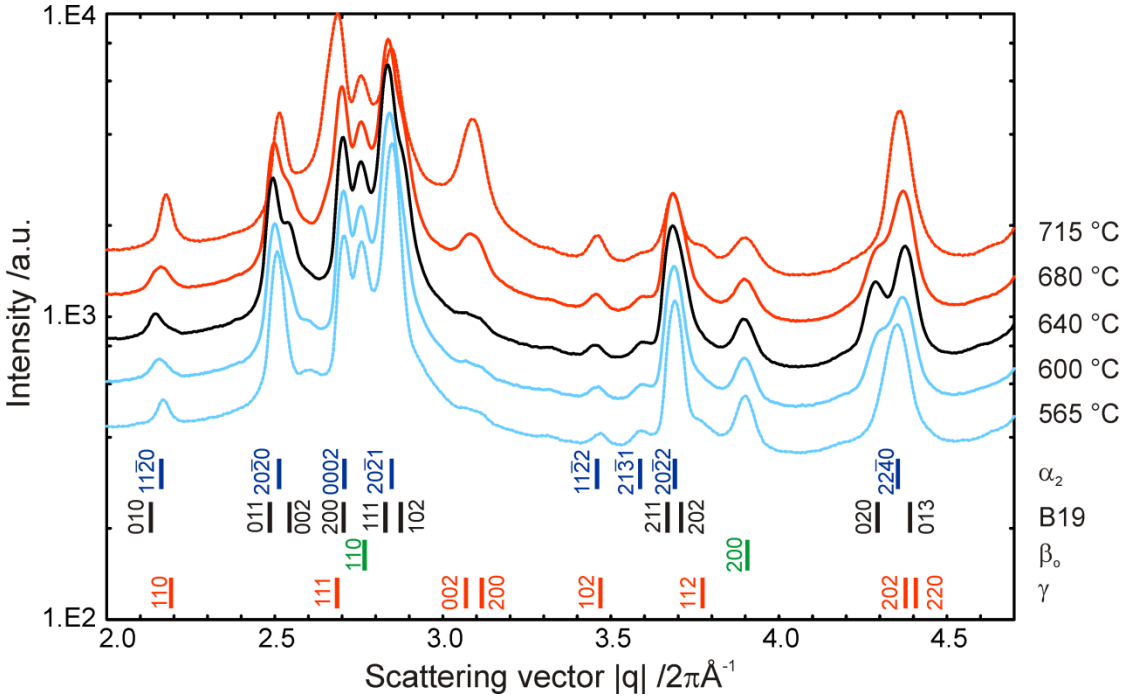

Figure 2: *Diffractograms obtained by HEXRD during continuous heating. Temperatures at which the patterns were obtained are indicated on the right. It is obvious that peaks of α_2 reflections split due to the formation of the orthorhombic B19 phase. All reflections are indexed at the bottom.*

When a higher heating rate (25 °C/min) is used, the diffraction patterns show similar changes, only shifted to higher temperatures. The splitting of α_2-phase reflections starts at

about 650 °C and the maximum peak separation is reached at approximately 710 °C. The appearance of the γ reflections and the reduction in α_2-peak intensity occurs at 740 °C.

In order to investigate if any microstructural changes occurred during heating to 640 °C, one specimen was heated to this temperature (at a rate of 2 °C/min) and subsequently quenched. A second specimen was only subjected to the primary heat-treatment at 1450 °C and quenched. Using standard metallographic methods [17], both samples were prepared for scanning electron microscopic (SEM) investigations using a Zeiss Evo 50 microscope in the back-scattered electron (BSE) mode. Comparison of the obtained micrographs revealed no apparent changes (see **Figure 3** with the specimen heated to 640 °C). Only two phases (α_2 and β_o) can be distinguished which exhibit morphologies that strongly resemble martensitic microstructures observed in commercial Ti alloys (e.g. [18, 19]). Although a small γ peak is observed in the diffraction pattern obtained at 640 °C, no indication for γ formation was found in the micrograph. This might be due to the fact that γ forms ultrafine lamellae during its early stages of precipitation [20] which cannot be resolved in the SEM.

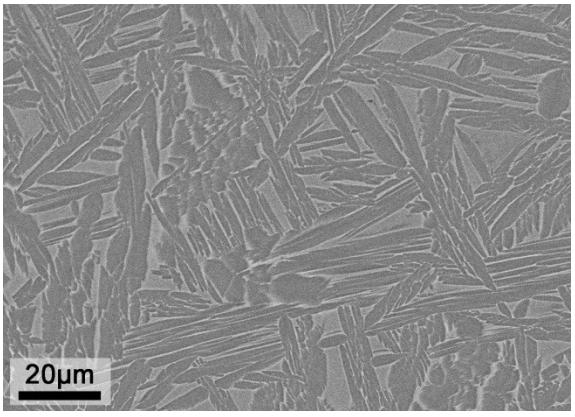

Figure 3: *SEM micrograph of the specimen after heating to 640 °C at a rate of 2 °C/min. The image was obtained in BSE mode. β_o appears in light grey and B19 in dark grey.*

From the sequence of events, it is tempting to speculate that a precursor phase forms in supersaturated α_2 and facilitates the precipitation of γ-phase. The splitting of the hexagonal α_2 reflections 20-2l and 22-4l is an indication of an orthorhombic distortion of the lattice. All former α_2 reflections and the newly split double peaks can clearly be attributed to a transient orthorhombic phase with B19 structure (Pmma) as shown in **Figure 2**. At the temperature where the peak separation is most clearly visible (T=640 °C), the lattice parameters of B19 were evaluated to a=4.65 Å, b=2.93 Å and c=4.95 Å. At this stage, all of the α_2 phase had transformed to B19, and the phase fractions are approximately 80 vol% B19 and 20 vol% β_o. The finding that all of α_2 transforms to B19 before γ precipitation starts is in contrast to the observations of Abe et al. [10] and Tanimura et al. [12]. However, this

apparent disagreement may be a consequence of the different alloy compositions used in these studies.

Concerning the formation of B19 it should be noted that the splitting of α_2 reflections increases continuously as the temperature rises. One example for the development of double peaks is the former 22-40-α_2 reflection which gradually splits into two clearly separated peaks, 020-B19 and 013-B19. This indicates that the B19 formation is associated with a diffusional process and a continuous change in the chemical composition occurs. This conclusion is supported by the observation that the temperature of formation of B19 strongly depends on the heating rate.

In this study the transformation processes were observed in-situ whereas former studies depended on post mortem analyzed samples. It was, however, not possible to identify any changes between the as-quenched and the annealed to 640 °C samples by means of SEM in back scattered electron (BSE) contrast. Since the chemical compositions and the crystal structures of α_2 and B19 are quite similar, it is not unlikely that the microstructural changes induced by the phase transformation are too subtle to be detected in the SEM. For this reason, TEM investigations are planned for the forthcoming studies.

Unfortunately, no information on the stability of the B19 phase within the observed temperature range was obtained and further experiments are needed to clarify this matter. This study, however, is the first report on the formation of B19 phase in TiAl alloys observed in-situ. It was found that B19 forms as a transient phase facilitating the precipitation of γ from α_2. Furthermore, it was possible to determine the temperature range in which the B19 phase occurs in the investigated alloy

Conclusion

During heating of a heat-treated and quenched Ti-45 Al-3 Mo-0.1 B alloy (nominal composition), an unexpected transitional phase was identified employing a high-energy X-ray diffraction method. It was shown that the supersaturated α_2 phase transformed via the orthorhombic B19 phase to γ and α_2. It was also determined that the B19 phase formed in the temperature range from 600-700 °C when a heating rate of 2 °C/min is employed. The close structural relationship between α_2, γ and B19 facilitates the formation of this phase and is elaborated here. Since industrial processes are frequently conducted at high heating and cooling rates, the observation of B19 phase formation during processes far from thermal equilibrium has a strong technological relevance.

References

[1] H. Clemens, W. Smarsly, *Advanced Materials Research* **2011**, *278*, 551-556.

[2] R. Kainuma, Y. Fujita, H. Mitsui, I. Ohnuma, K. Ishida, *Intermetallics* **2000**, *8*, 855-867.

[3] H. Clemens, W. Wallgram, S. Kremmer, V. Güther, A. Otto, A. Bartels, *Advanced Engineering Materials* **2008**, *10*, 707-713.

[4] F.-S. Sun, C.-X. Cao, S.-E. Kim, Y.-T. Lee, M.-G. Yan, *Metallurgical and Materials Transactions A* **2001**, *32*, 1573-1589.

[5] H. Clemens, H.F. Chladil, W. Wallgram, G.A. Zickler, R. Gerling, K.-D. Liss, S. Kremmer, V. Guther, W. Smarsly, *Intermetallics* **2008**, *16*, 827-833.

[6] T. Schmoelzer, S. Mayer, C. Sailer, F. Haupt, V. Güther, P. Staron, K.-D. Liss, H. Clemens, *Advanced Engineering Materials* **2011**, *13*, 306-311.

[7] S. Mayer, C. Sailer, H. Nakashima, T. Schmoelzer, T. Lippmann, P. Staron, K.-D. Liss, H. Clemens, M. Takeyama, *Mater. Res. Soc. Symp. Proc.* **2011**, *1295*, 113-118.

[8] S. Kabra, K. Yan, S. Mayer, T. Schmoelzer, M. Reid, R. Dippenaar, H. Clemens, K.-D. Liss, *International Journal of Materials Research (formerly Zeitschrift Fuer Metallkunde)* **2011**, *102*, 697-702.

[9] A. Stark, M. Oehring, F. Pyczak, A. Schreyer, *Advanced Engineering Materials* **2011**, *13*, 700-704.

[10] E. Abe, T. Kumagai, M. Nakamura, *Intermetallics* **1996**, *4*, 327-333.

[11] F. Appel, M. Oehring, J.D.H. Paul, *Advanced Engineering Materials* **2006**, *8*, 371-376.

[12] M. Tanimura, Y. Inoue, Y. Koyama, *Scripta Materialia* **2001**, *44*, 365-373.

[13] A. Stark, *Textur- Und Gefügeentwicklung Bei Der Thermomechanischen Umformung Nb-reicher γ-TiAl-Basislegierungen*, Shaker Verlag, Aachen **2010**.

[14] T. Lippmann, L. Lottermoser, F. Beckmann, R.V. Martins, T. Dose, R. Kirchhof, A. Schreyer, in *Hasylab Annual Report*, Hamburg, Germany **2007**, 113.

[15] P. Staron, T. Fischer, T. Lippmann, A. Stark, S. Daneshpour, D. Schnubel, E. Uhlmann, R. Gerstenberger, B. Camin, W. Reimers, E. Eidenberger, H. Clemens, N. Huber, A. Schreyer, *Advanced Engineering Materials* **2011**, *13*, 658-663.

[16] A.P. Hammersley, S.O. Svensson, M. Hanfland, A.N. Fitch, D. Hausermann, *High Pressure Research* **1996**, *14*, 235-248.

[17] R. Schnitzer, H.F. Chladil, C. Scheu, H. Clemens, S. Bystrzanowski, A. Bartels, S. Kremmer, *Praktische Metallographie* **2007**, *44*, 430–442.

[18] H. Matsumoto, H. Yoneda, K. Sato, S. Kurosu, E. Maire, D. Fabregue, T.J. Konno, A. Chiba, *Materials Science and Engineering A* **2011**, *528*, 1512-1520.

[19] M. Takeyama, S. Kobayashi, *Intermetallics* **2005**, *13*, 993-999.

[20] L. Cha, H. Clemens, G. Dehm, *International Journal of Materials Research (formerly Zeitschrift Fuer Metallkunde)* **2011**, *102*, 703-708.